

Experimental Investigation of Unstrained Diffusion Flames and their Instabilities

THÈSE N° 4249 (2008)

PRÉSENTÉE LE 12 DÉCEMBRE 2008

À LA FACULTE SCIENCES ET TECHNIQUES DE L'INGÉNIEUR
LABORATOIRE DE MÉCANIQUE DES FLUIDES
PROGRAMME DOCTORAL EN MÉCANIQUE

ÉCOLE POLYTECHNIQUE FÉDÉRALE DE LAUSANNE

POUR L'OBTENTION DU GRADE DE DOCTEUR ÈS SCIENCES

PAR

Etienne ROBERT

acceptée sur proposition du jury:

Prof. M. Deville, président du jury
Prof. P. Monkewitz, directeur de thèse
Prof. M. Matalon, rapporteur
Dr Ph. Metzener, rapporteur
Prof. Ph. R. von Rohr, rapporteur



ÉCOLE POLYTECHNIQUE
FÉDÉRALE DE LAUSANNE

Suisse
2009

À Emma et Nils,

Merci!

Acknowledgments et remerciements

This thesis would not have been possible without a great number of people, their support, their skills and their ideas. This page will certainly be too short to express all of my gratitude, but I still wish to thank them properly.

First and foremost, the idea behind the burner used and developed in this thesis is the brainchild of my thesis supervisor, professor Peter Monkewitz. I would like to express my deep gratitude for giving me the opportunity to work on such an interesting problem. His experimental instincts and considerable theoretical wisdom are the main reasons I learned so much during this thesis, thank you Peter.

Peter also introduced me to professor Moshe Matalon, who was of great help with the theoretical side of the problem. His collaboration was extremely valuable in ensuring that our experimental realization was consistent with the theoretical approach to the problem, and for that I am grateful.

None of the work presented here would have been possible without the financial support of the Swiss National Science Foundation under Grant 20020-108074.

Un grand merci aussi aux mécaniciens de l'atelier central qui ont avec tellement de talent transformé mes idées folles en réalité. Merci particulier à Bernard pour le volume considérable de travail qu'il a accompli sur ce projet, avec toujours une qualité irréprochable. Merci à Marc pour avoir compris l'urgence de la situation quand c'était nécessaire. Merci à tous les autres pour les petits et les plus gros coups de pouce!

Merci aussi aux collègues qui font qu'autour d'une bière à sat ou d'une glace sur la terrasse, il est possible de déconnecter de cette thèse l'espace d'un instant. Merci à ceux que j'ai côtoyés longtemps : Emeric, Richard et Radboud qui ont d'excellente compagnie durant cette thèse, que ce soit pour le côté technique ou social. Je n'oublie pas les doctorants qui ont quitté le labo peu après mon arrivée : Chris Pipe et en particulier David Lo Jacono qui réalisa la première version de l'expérience utilisée dans cette thèse. Merci aussi aux doctorants du labo d'à côté, en particulier Roland, Orestis et Marc-Antoine, sans qui les pause cafés se passeraient bien trop souvent en petit comité vu la modeste taille de notre labo.

Les visites régulières et toujours agréables des membres de ma famille ont aussi été fort utiles pour garder le moral au fil de toutes ses années passées loin de mon petit coin de pays. Une pensée toute particulière pour mon papa Michel et mes deux petits frères Marc-Antoine et Pierre-Yves qui n'ont pas hésité à venir se graisser les mains dans mon labo quand ils passent me voir en Suisse.

Finalement, je ne saurais passer sous silence le support indéfectible que j'ai reçu de mon amour de toujours. Emma, merci infiniment pour tout, tu es la meilleure! Plus récemment, les merveilleux sourires de mon fils Nils qui me tire les pantoufles quand j'écris cette thèse ont été une source de motivation incroyable.

Abstract

In this thesis, thermal-diffusive instabilities are studied experimentally in diffusion flames. The novel species injector of a recently developed research burner, consisting of an array of hypodermic needles, which allows to produce quasi one-dimensional unstrained diffusion flames has been improved. It is used in a new symmetric design with fuel *and* oxidizer injected through needle arrays which allows to independently choose both the magnitude and direction of the bulk flow through the flame. A simplified theoretical model for the flame position, the temperature and the species concentration profiles with variable bulk flow is presented which accounts for the transport properties of both reactants. The model results are compared to experiments with a CO_2 -diluted H_2-O_2 flame using variable bulk flow and inert mixture composition.

The mixture composition throughout the burning chamber is monitored by mass spectrometry. An elaborate calibration procedure has been implemented to account for the variation of the mass spectrometer sensitivity as a function of the mixture composition. The calibrated results allow the *effective* mixture strength of the diffusion flames to be measured with a relative uncertainty of about 5 %.

In order to properly characterize the flame produced, the velocity and temperature distribution inside the burning chamber are measured. The resulting species concentration and temperature profiles are compared to the simplified theory and demonstrate that the new burner configuration produces a good approximation of the 1-D chambered diffusion flame, which has been used extensively for the stability analysis of diffusion flames. The velocity profiles are also used to quantify the residual stretch experienced by the flame which is extremely low, below 0.15 s^{-1} . Hence, this new research burner opens up new possibilities for the experimental validation of theoretical models developed in the idealized unstrained 1-D chambered flame configuration.

The thermal-diffusive instabilities observed close to extinction are investigated experimentally and mapped as a function of the Lewis numbers of the reactants. The use of a mixture of two inerts (helium and CO_2) allows for the effect of a wide range of Lewis numbers to be studied. A cellular flame structure is observed in hydrogen flames when the Lewis numbers is relatively low with a typical cell size between 7 and 15 mm. The cell size is found to scale linearly with the diffusion length, in good agreement with theoretical predictions. When the Lewis number is increased by using a higher helium content in the dilution mixture, the instabilities observed are planar intensity pulsation. The use of methane allowed pulsating flames to be generated for a wide range of bulk velocities and transport properties. The pulsating frequencies measured are in the 0.7 to 11 Hz range and were found to scale linearly with a diffusion frequency defined as U^2/D_{th} multiplied by the square root of the Damköhler number. The experimental results presented here are the first observations of thermal-diffusive instabilities in such a low-strain flame. They constitute a unique dataset that can be used to quantitatively validate theoretical models on diffusion flame stability developed in the simplified one-dimensional configuration.

Keywords: Thermal-diffusive instability, unstrained, diffusion flame, experimental.

Résumé

L'utilisation d'un nouveau type de brûleur permet de produire des flammes de diffusion uni-dimensionnelles et sans étirement. La nouveauté réside dans la manière avec laquelle les espèces réactives sont introduites dans le brûleur, au travers de certaines d'aiguilles hypodermiques. Une évolution du design est introduite dans laquelle l'arrangement symétrique du système d'injection permet un contrôle indépendant sur l'intensité et la direction de l'écoulement moyen dans la chambre de combustion. Un modèle théorique simplifié tenant compte de l'écoulement moyen variable est présenté pour la position de flamme de même que les profils de concentration et d'espèce dans le brûleur. Les prédictions de ce modèle sont comparés aux résultats expérimentaux pour des flammes d'hydrogène et d'oxygène dilués dans du CO_2 .

La composition du mélange de gaz présent dans la chambre de combustion est mesuré à l'aide d'un système de spectrométrie de masse. Une technique de calibration sophistiquée a du être mise au point pour compenser le changement de la sensibilité de l'instrument intervenant en fonction de la composition du mélange mesuré. La flamme produite a aussi été caractérisée par la mesure des distributions de vitesse et de température dans le brûleur. Les profils de concentration et de température ainsi obtenus ont été comparés avec succès à la théorie simplifiée. Ceci démontre que la flamme produite est une bonne approximation de la configuration uni-dimensionnelle simplifiée, qui est utilisée abondamment dans le développement de modèles théoriques sur la stabilité des flammes de diffusion. Les profils de vitesse permettent également une évaluation de l'étirement résiduel subi par la flamme, qui est inférieur à 0.15 s^{-1} . Ce nouveau type de brûleur de recherche ouvre de nombreuses possibilités de recherches, en particulier pour la validation expérimentale de modèles théoriques sur la stabilité des flammes de diffusion, développés en supposant une absence d'étirement dans la configuration uni-dimensionnelle simplifiée.

Les instabilités thermo-diffusives formées à l'approche de l'extinction ont été observées et cartographiées en fonction des nombres de Lewis des espèces utilisées. L'utilisation d'un mélange de deux gaz inertes (hélium et CO_2) pour la dilution des espèces réactives a permis le balayage d'une large plage de nombres de Lewis. Une structure de flamme cellulaire est observée pour les nombres de Lewis relativement faibles, avec une taille de cellules comprise entre 7 et 15 mm, évoluant linéairement avec la longueur caractéristique de diffusion, conformément aux prédictions théoriques. Quand le nombre de Lewis est augmenté en utilisant une plus grande proportion d'hélium dans le mélange de dilution, les instabilités observées deviennent des oscillations planes de l'intensité de la réaction. L'utilisation du méthane comme combustible a permis la production de flammes oscillantes sur une large plage de vitesse d'advection et de propriété de transport du mélange. Les fréquences de pulsation observées sont incluses dans l'intervalle de 0.7 à 11 Hz, et évoluent en fonction d'une fréquence de diffusion définie comme U^2/D_{th} multipliée par la racine carrée du nombre de Damköhler. Les résultats expérimentaux d'instabilité thermo-diffusives présentés ici sont les premiers réalisés dans une telle flamme pratiquement dépourvue d'étirement. Ils constituent une base de données unique permettant les premières validations quantitatives des modèles sur la stabilité des flammes de diffusion réalisés dans la configuration uni-dimensionnelle simplifiée.

Mots-clés: Instabilités thermo-diffusives, flamme de diffusion, étirement, étude expérimentale.

Contents

1	Introduction	1
1.1	Chemically reacting flows	1
1.2	Reaction-diffusion instabilities	2
1.2.1	The study of thermal-diffusive (TD) instabilities	5
1.2.2	The study of TD instabilities in diffusion flames	6
1.3	Objectives and scope of the thesis	7
1.4	Contributions	8
1.5	Thesis Outline	9
2	State of the art	11
2.1	Theoretical studies	11
2.2	Experimental studies	14
2.3	Numerical methods	16
3	Theoretical considerations	19
3.1	Simple one-dimensional model for the baseline flame	19
3.1.1	Reaction-sheet approximation	20
3.1.2	Model results	22
3.1.3	Adiabatic flame temperature	23
3.2	Stability considerations	24
3.2.1	The response curve	24
3.2.2	Thermal-diffusive instabilities	27
3.3	Numerical tools	28
4	Experimental facilities and methods	31
4.1	The burners	31
4.1.1	Mark I burner	32
4.1.2	Mark II burner	35
4.2	Image Acquisition	39
4.2.1	Photography	39
4.2.2	Video	41
4.3	Velocity measurements	41
4.3.1	Laser Doppler Anemometry (LDA)	42
4.3.2	Hot thermistor anemometry	42
4.4	Temperature measurements	43
4.4.1	Temperature measurements with thermocouples	44
4.4.2	Probes fabrication	44
4.4.3	Effective temperature	50

4.5	Gas mixtures preparation	51
5	Mixture composition measurements	55
5.1	The choice of experimental technique	55
5.2	Mass spectrometry based PPA	57
5.3	The instrument working principles	57
5.3.1	Sampling	59
5.3.2	The ion source	59
5.3.3	The mass analyzer	61
5.3.4	The detectors	61
5.3.5	Control software	62
5.4	Mass spectrometer calibration	63
5.4.1	Built-in procedure	63
5.4.2	Calibration over a wide concentration range	64
5.4.3	Results and discussion	69
6	Burner characterization	73
6.1	Flame shape	74
6.1.1	Flame parasitic curvature	75
6.1.2	Formation of convection cells	76
6.2	Velocity measurements	78
6.2.1	Injection layer	78
6.2.2	Transverse velocity profiles	79
6.2.3	Residual strain	81
6.3	Temperature measurements	83
6.3.1	Temperature in the burning chamber	86
6.4	Species measurements	86
6.4.1	Species transverse concentration profiles	87
6.4.2	Species longitudinal concentration profiles	89
6.5	Flame position	90
6.5.1	Virtual origin	90
6.5.2	Influence of bulk velocity	93
6.5.3	Influence of Lewis number	93
7	Experimental observation of TD instabilities	97
7.1	Stability and extinction limits	97
7.2	Mapping of the instabilities	100
7.3	Cellular flames	102
7.3.1	Observed instabilities	102
7.3.2	Cell size scaling	105
7.4	Planar intensity pulsations	107
7.4.1	Observed instabilities	109
7.4.2	Pulsation frequency scaling	113
8	Conclusions and outlook	123
A	Mass spectrometer system analysis	127
A.1	Working pressures	127
A.2	Sampling rate and ionization efficiency	131
B	Possible reactant and inert combinations	133

<i>CONTENTS</i>	xiii
C Nomenclature	135
Bibliography	147
Curriculum Vitae	149

List of Tables

4.1	Characteristics of the thermocouples used, before coating.	46
4.2	Characteristics of the thermocouples used.	48
6.1	Parameters used to generate the stable flames used for burner characterization.	73
7.1	Burner parameters for the flames presented in section 7.4.1.	115
7.2	Parameters considered in pulsation frequency scaling.	118
A.1	Conductance values (for CO ₂) for the vacuum system	129
A.2	Pressures and mean free paths throughout the vacuum system.	129

List of Figures

1.1	Origin of the reaction-diffusion instability resulting in pattern formation.	3
1.2	Examples of reaction-diffusion patterns.	4
1.3	Premixed burner configurations.	6
1.4	Non-premixed burner configurations.	8
2.1	Detailed map of the instabilities expected close to extinction.	18
3.1	Conventional and symmetric chambered diffusion flame	20
3.2	Theoretical species concentration profiles.	23
3.3	Typical S-shaped response curve.	26
3.4	Enlargement of the S-curve region close to the extinction limit.	26
3.5	Qualitative sketch of the types of instabilities expected.	28
3.6	Species and temperature profiles obtained using the Cantera software package.	29
4.1	Schematic of the Mark I version of the burner.	32
4.2	Detailed representation of the injection layer.	33
4.3	Typical pictures of flames from the unmodified Mark I burner.	34
4.4	Picture of flat flame in the Mark I burner.	34
4.5	Schematic and photograph of symmetric Mark II burner.	36
4.6	Injection and extractor tube configuration.	37
4.7	Mark II burning chamber and flame shape.	38
4.8	Picture of one of the Mark II extraction plenums.	39
4.9	Viewing angles used to capture the flame location.	40
4.10	Sample of hot thermistor anemometer calibration curve.	43
4.11	Thermocouple schematic for the heat transfer problem.	45
4.12	Picture of thermocouples probes used.	47
4.13	Pictures of the uncoated and coated thermocouple junctions.	48
4.14	Water vaporisation scheme used to produce calibration mixtures.	53
5.1	Outline of the different components of the mass spectrometer.	58
5.2	Picture of the MKS Cirrus RGA used in this thesis.	58
5.3	Mass spectrometer sensitivity in binary mixtures of H ₂ , O ₂ , CO ₂ in Ar.	65
5.4	Mass spectrometer sensitivity variation in the presence of H ₂ O.	66
5.5	Time dependence of mass spectrometer sensitivity.	67
5.6	Mass spectrometer sensitivity in H ₂ -O ₂ -CO ₂ mixtures.	68
5.7	Mass spectrometer sensitivity in H ₂ -He-Ar mixtures.	70
5.8	Mass spectrometer sensitivity in O ₂ -He-Ar mixtures.	70

5.9	Evaluation of the calibrated mass spectrometer measurement error. . .	71
5.10	Evaluation of the mass spectrometer measurement error with rudimentary calibration.	72
6.1	Flame shapes in the Mark I and Mark II burners.	74
6.2	Profile of the flame visible light emission.	75
6.3	Angle of the vector normal to the flame sheet.	76
6.4	Effect of convective cells in the burner on flame shape.	78
6.5	Velocity profiles in the injection layer.	79
6.6	Vector plot of the velocity in the Mark I burner.	80
6.7	Vertical and horizontal components of the velocity in the burner. . . .	81
6.8	Transverse velocity profile in the Mark II burner.	82
6.9	Velocity profile and residual stretch in the flame sheet.	84
6.10	Picture of thermocouple probes inserted in the burner.	84
6.11	Longitudinal temperature profiles from coated and uncoated probes. . .	85
6.12	Magnitude of the radiation correction as a function of measured temperature.	86
6.13	Radiation corrected longitudinal temperature profiles.	87
6.14	Comparison between experimental, numerical and theoretical longitudinal temperature profiles.	87
6.15	Flame temperature distribution across the burning chamber.	88
6.16	Effect of the walls on the oxidant distribution in the chamber.	89
6.17	Longitudinal species concentration profiles.	91
6.18	Sketch illustrating the choice of the virtual origin location.	91
6.19	Effect of bulk velocity and mixture density on the virtual origin. . . .	92
6.20	Effect of bulk flow velocity on flame position.	94
6.21	Effect of U and Le_x on flame position predicted by the simplified theory. .	94
6.22	Experimental results for flame position with variable Lewis numbers. . .	95
7.1	Stability limits inferred from the supplied flow rates.	98
7.2	Stability limits inferred from the mass spectrometric data.	99
7.3	Mixture strength inferred from flow rates and mass spectrometry. . . .	100
7.4	Flame position change as the flame becomes unstable.	101
7.5	Mapping of the instabilities in the Lewis number parameter space. . . .	102
7.6	Photographs of cellular flames.	103
7.7	Cell motion in cellular flames.	104
7.8	Concentration profiles across a cellular flames.	104
7.9	Cell size scaling with bulk velocity.	105
7.10	Cell size scaling with thermal diffusivity.	106
7.11	Scaling of the cell size.	107
7.12	Effect of bulk velocity and mixture density on the mixture strength. . .	108
7.13	Example of sampling window used for the video analysis.	109
7.14	Intensity pulsation in a helium diluted hydrogen flame.	109
7.15	Pulsation in a methane flame with the inner quartz cylinder present. . .	110
7.16	Pulsation in a methane flame without the inner quartz cylinder present. .	111
7.17	Very flat pulsating methane flame.	112
7.18	Variation of the flame intensity for different types of pulsations. . . .	113
7.19	Simultaneous variation of the flame intensity and position.	114
7.20	Concentration profiles across two pulsating flames.	114
7.21	Treatments and Fourier transform of intensity signal.	117

7.22 Pulsation frequency scaling with the diffusion frequency.	118
7.23 Pulsation frequency scaling obtained from dimensional analysis. . . .	119
7.24 Scaling of the pulsation frequency with the Damköhler number. . . .	122
8.1 Soot layer in a methane flame.	126
A.1 Schematic representation of the mass spectrometer vacuum system . .	128
B.1 Lewis number parameter spaces covered by various gas mixtures. . .	134

Chapter 1

Introduction

The thesis presented here covers the subject of thermal-diffusive (TD) instabilities in diffusion flames. The understanding of this phenomena is of great interest in modern combustion systems who tend to be operated with lean mixtures to control emissions, making them prone for the development of these instabilities. The experimental investigations were carried out in a novel research burner that allows the creation of a nearly-unstrained one-dimensional diffusion flame. In the absence of strain and other hydrodynamic effects, the results gathered can be compared quantitatively with simplified theoretical models, providing the experimental validation they lacked so far.

1.1 Chemically reacting flows

Combustion processes have played a central role throughout human history, often providing the energy driving the paradigm shifts that shaped our current societies. The discovery and control of fire over a million years ago [1] contributed to the emergence of our species and is used as a criterion to identify our ancestors. The ability to generate artificial fire arrived much later towards the end of the middle Paleolithic era with the Neanderthal man striking flint against pyrite [2]. The first civilizations of Mesopotamia used combustion extensively for smelting copper, sparking the bronze age and countless technological advances brought by hard metal. In the late 18th century, the use of fossil fuels in the industrial revolution brought us where we are today: in a society dependent upon combustion for most of its energy supply but still a long way from fully understanding the intricacies of the combustion process. The current recently acquired awareness of the consequences of the widespread use of fossil fuels such as the generation of various air pollutants [3] and the rise in atmospheric CO₂ concentration [4, 5] infuses a renewed purpose to the field of combustion research.

Combustion refers to an exothermic reaction between a fuel and an oxidizing agent usually mediated through a series of radical chain reactions. The detailed study of chemically reacting systems invariably brings the question of how are the reactants brought to the reaction site and how are the products evacuated. As a result, combustion problems are tightly coupled with associated fluid dynamics problems. The governing equations of chemically reacting flows are therefore the equations of fluid motion supplemented by the equations governing the chemical process. The interactions of these chemical and transport processes can lead to instability, a state characterized by the unbounded growth of a small perturbation. In combustion systems the growth is limited

by the geometry of the burning chamber resulting in pattern formation in the flame, periodic load variations or extinction, compromising performance and reliability.

In most practical applications the combustion is turbulent and partially premixed, making its analysis particularly complicated. In this situation, the transport of species is done by advection and diffusion. However, the chemistry is usually fast compared to transport processes, resulting in thin reaction zones with steep concentration gradients where diffusion is the locally dominant transport phenomena. In both premixed and non-premixed combustion, the competing mechanisms of diffusion and reaction can be a source of instability. The former distributes heat and species from regions of abundance to regions of relative scarcity, while the latter requires heat to act as a sink for reactants and a source for products. These thermal-diffusive (TD) instabilities can result in the formation of cellular patterns in the flame from the uneven spatial distribution reaction rate magnitude. The phenomenon has been observed in both premixed and non-premixed configuration. Pulsation in flame intensity and other phenomena can also result from this thermal-diffusive instability.

In order to reduce emissions, the trend in many modern combustion applications is to operate the combustors in a lean mixture, making them more susceptible to the development of thermal-diffusive instabilities. These instabilities playing a key role in soot formation [6, 7] and in the dynamic extinction and re-ignition process, fundamental knowledge of their behavior is desirable.

1.2 Reaction-diffusion and thermal-diffusion instabilities

The thermal-diffusive instability is part of the larger family of reaction-diffusion (RD) instabilities. They can occur wherever the differential transport of reactants and products to a reaction site is dominated by diffusion. Alan Turing, in his landmark paper on morphogenesis [8] postulated this mechanism to be at the origin of pattern formation in the natural world, from leaf arrangement on a stem to fingerprints. Although the underlying mechanisms are different in the Turing instability in morphogenesis and in the thermal-diffusive instabilities in combustion, interesting parallels can be drawn between the two.

Three conditions must be met for the RD or TD instabilities to develop, as illustrated in figure 1.1. First, in both cases a product of the reaction must be a catalyst for that same reaction, making it auto-catalytic. In the case of morphogenesis, this product is an biological activator that was only postulated to exist by Turing, but whose existence has been demonstrated since [9, 10]. Specific activator/inhibitor pairs have been linked to the formation of hair [11], feathers [12] and teeth [13]. For combustion, heat as a reacting agent induces a positive feedback through its action on the reaction rate. Secondly, another product of the reaction must have the opposite effect of slowing the rate of the reaction upon its release. In combustion systems, the release of combustion products has this effect by reducing the available concentration of reactants in the reaction area. For biological systems, Turing again postulated the existence of reaction inhibitors that were later identified. Finally, for pattern formation to occur, the diffusion coefficient of the activator must be significantly higher than that of the inhibitor [8, 14, 15]. This favors sites where the reaction is already occurring to remain active while preventing propagation and merging of different active sites. The resulting regions of relatively high reaction rate will become the petals of the flower, the ridge of

your fingerprints or the cells of the cellular flame.

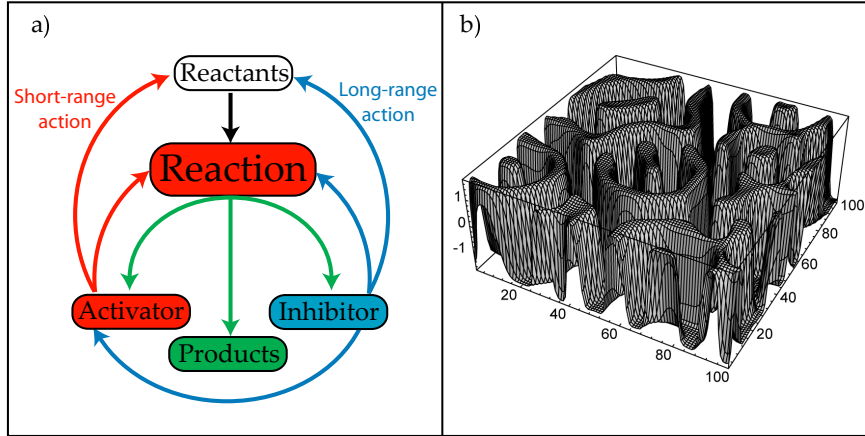


Figure 1.1: (a) The origin of the reaction-diffusion instability leading to pattern formation, a autocatalysed reaction where a product is also an inhibitor that diffuses faster than the catalyst. (b) Differential diffusion of the agents results in pattern formation in the intensity of the reaction and hence in the distribution of the products. Here a simulation of the labyrinthine pattern in the cerebral cortex, taken from [16].

Since the innovative work of Turing, pattern formation in reactive-diffusive systems has been studied extensively. Numerical studies have predicted a certain number of pattern that should occur under specific conditions [17, 18]. Experimentalists observed some of these patterns in specially designed gel-filled reactors with peculiar chemical reactions systems displaying the characteristics necessary for the development of the Turing instability. Experimental observations include rotating spirals [19], stationary strips or cells and self replicating cells [20]. Examples of patterns predicted analytically or numerically and observed experimentally are presented in figure 1.2.

The reaction-diffusive and thermal-diffusive systems differ because the effect of heat on the combustion reaction rate is of much higher non-linear order than the one of any activator on a bio-chemical reaction. In chemical systems, reaction occur when two reactive molecules collide with a sufficient amount of energy E called the activation energy. Arrhenius [23] was the first to recognize fact and introduced relation 1.1 that now bears his name to account for the temperature variation of the chemical reaction rate.

In this equation, ω is the reaction rate, A is the pre-exponential factor (also called the frequency factor), R is the perfect gas constant and T the temperature. The pre-exponential factor exhibits a weak temperature dependence and the Arrhenius equation can be modified to equation 1.2, where T_0 is a reference temperature and n a unitless power. The expression $\exp(E/RT)$ is the Boltzmann factor, representing the fraction of all collisions that have at least an energy of E .

$$\omega = A \exp(-E/RT) \quad (1.1)$$

$$\omega = A' \left(\frac{T}{T_0} \right)^n \exp(-E/RT) \quad (1.2)$$

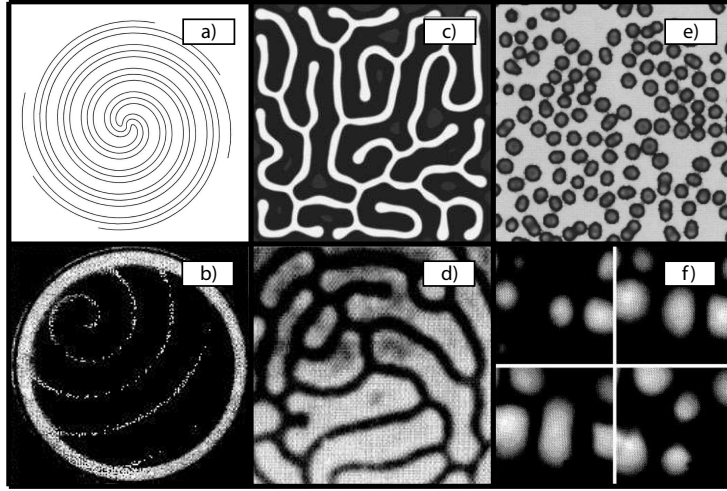


Figure 1.2: Examples of reaction-diffusion patterns. Rotating spiral in the concentration distribution, analytical solution (a) from [21], experimental observation (b) from [19]. Lamellar pattern, numerical simulation (c) from [18] and experimental observation (d) from [20]. Self-replicating spot pattern, numerical simulation (e) from [22] and experimental observation (f) from [20].

On the other hand, in bio-chemical systems pattern formation is caused by the *marginal reaction rate*, that is the change in reaction rate is mainly caused by the change in the reactant concentration [8, 24] through the actions of the activator and inhibitor. This change is therefore affecting the pre-exponential factor A of equation 1.1 which is a measure of the collision frequency between the reactive species. Turing [8] assumed that the reaction rate was a linear function of the reactants concentrations, following the law of mass action, an hypothesis justifiable for systems just beginning to leave a homogeneous condition. The temperature and concentration dependence of the pre-exponential factor of equation 1.1 is detailed in equation 1.3.

$$A = [A]^i [B]^j \sigma_{AB} \left[\frac{8k_B T}{\pi \mu} \right]^{1/2} \quad (1.3)$$

The symbols in brackets $[A],[B]$ represents the concentrations of species A and B while σ_{AB} is their hard-sphere collision cross-section, k_B the Boltzmann constant and μ the reduced mass ($m_A m_B / (m_A + m_B)$) with $m_{A,B}$ the mass of the reactive species. The exponents i and j are the orders of the reaction with respect to A and B respectively.

Additionally, most potential activator-inhibitor combinations have similar diffusivities in aqueous solutions, with nearly all simple molecules and ions having a diffusion coefficient within a factor 2 of $1.5 \times 10^{-5} \text{ cm}^2 \cdot \text{s}^{-1}$. Although this condition is not absolute [25], it helps explains why experimental evidence of Turing instabilities was only gathered relatively recently [14, 15] and first in chemical system rather than biological ones.

1.2.1 The study of thermal-diffusive (TD) instabilities

Thermal diffusive instabilities are known to occur in both premixed and non premixed combustion, for reviews see [26, 27, 28, 29]. The focus of the present research lies in the experimental investigation of thermal-diffusive instabilities of non-premixed or diffusion flames. In this configuration, the reactants are supplied separately to the reaction area and combustion occurs where they meet in stoichiometric proportions. The choice of using diffusion flames to study these instabilities is justified by the limitations inherent to the premixed configuration. However, considerably more attention has been directed towards the thermal-diffusive instabilities of premixed than non-premixed flames. In premixed combustion, the reaction is located in a flame front that travels with a characteristic velocity in the combustible mixture.

Because of the practical importance of this flame speed, the first experimentations on flat flames were aimed at determining the characteristic velocity of the propagation of a flame front in a combustible mixture. The pioneering work of Mallard and Le Chatelier [30] on a simple laminar flame front traveling in a tube revealed the thermal nature of the mechanism responsible for flame propagation. For an interesting historical perspective with illustration of the apparatus used, see the review of Oppenheim [31]. It was not until much later than Darrieus [32] and Landau [33] independently demonstrated that such planar deflagration fronts are inherently unstable. It is the much stronger coupling between the reaction and diffusion processes [26, 28] in this configuration that gives rise to aerodynamic instabilities resulting from thermal expansion. This Darrieus-Landau instability makes flat flame fronts simply established in a chambered flow of combustible mixture (figure 1.3(a)) unpractical for experiments aimed at investigating flame dynamics because of the strong coupling between this important hydrodynamic effect and the combustion process. Experimental results of a planar flame front deformed by the Darrieus-Landau instability is presented in [34]. A procedure allowing the creation of unstrained planar premixed flames is described by Searby [35]. It involves keeping the bulk velocity in the chamber of figure 1.3(a) at a critical velocity different than the laminar flame speed to avoid the Darrieus-Landau instability. More commonly, to study thermal-diffusive instabilities in premixed flames without these complications, the hydrodynamic instability is usually stabilized either through heat loss or hydrodynamic strain.

A premixed flat flame can be generated by supplying a combustible mixture through a porous injection plate because of the stabilizing effect of heat loss at the plate [36], see sketch in figure 1.3(b). However, this approach induces important perturbation of the flame front because of the heat loss and possible upstream diffusion of radicals towards the cold injection plate, where they are neutralized through wall collisions. Another approach consists at opposing free jets of the combustible mixture, resulting in the formation of two planar flames on either sides of the stagnation plane formed by the jets impinging one another, see [37] for pictures and figure 1.3(c) for a conceptual sketch. The radial expulsion of combustion products creates a velocity gradient, stretching and stabilizing the flame. This stretch has been shown to also have a strong effect on thermal-diffusive instabilities [29] and extinction [37], making this configuration of limited use to study these phenomena. Finally, if the combustible mixture is injected through a porous cylinder, the flow rate can be adjusted so that the diverging flow field stabilizes the flame [38], as shown in figure 1.3(d). However, buoyancy forces tend to break symmetry through the Rayleigh-Taylor instability [39] if the experiment is not carried out in microgravity.

One dimensional flame generated using the burner configurations mentioned in this

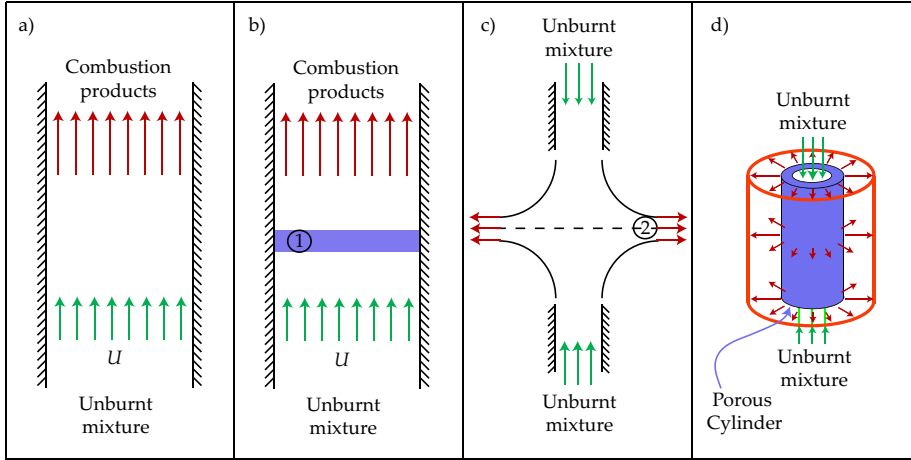


Figure 1.3: Premixed burner configurations. (a) Chambered premixed flame. Combustible mixture supplied from bottom at uniform velocity U corresponding to flame speed, resulting in static flame front. Unconditionally unstable to Darrieus-Landau instability. (b) Flat flame stabilized through heat loss at a water cooled porous plate (1) used to supply the mixture. (c) Opposed jets, with flame forming on either side of the stagnation plane (2), stabilized by hydrodynamic stretch. (d) Flame around a porous cylinder, stabilized by diverging flow field, requires microgravity.

section and some other type of burners such as the Bunsen torch have been used to study thermal-diffusive instabilities in premixed systems. However, the thermal or hydrodynamic perturbations induced by the burner prevents the investigation of the TD instabilities uncoupled from other phenomenon in these premixed flame.

1.2.2 The study of thermal-diffusive instabilities in diffusion flames

The strong coupling between the reaction and diffusion processes at the origin of the hydrodynamic instability in premixed flames is much less of a concern in the non-premixed configuration. The stabilization mechanism used in premixed combustion experiments invariably have an effect on the observed thermal-diffusive instabilities. To gain fundamental knowledge on the phenomenon, theoreticians and experimentalists seek to avoid these hydrodynamic effects to develop and validate their models. From this theoretical perspective, diffusion flames are an attractive analytical tool even if at first they seem far from actual combustion applications.

Although in most practical applications the combustion is turbulent and at least partially premixed, knowledge gained in diffusion flames can help model premixed flames. In the context of the turbulent flamelet model [40], where chemistry is considered fast compared to the transport process, the reaction occurs in asymptotically thin layers. These flamelets are embedded in the turbulent flow field with a one-dimensional inner structure. As long as the thickness of the flamelet is asymptotically thin, it can be shown that the advection is a lower order term than the chemically reacting part, making diffusion processes dominate the flamelet dynamics. To gain fundamental knowledge of the combustion process, one-dimensional flames configurations are therefore very attractive because of their use as a validation tool for theoretical models.

Several configurations are available to generate diffusion flames for research purposes. As with premixed flames, the challenge resides in keeping the transport process simple (ideally it should be strictly one-dimensional) and in avoiding thermal or hydrodynamic perturbations, such as strain. A very simple one-dimensional diffusion flame configuration was introduced as theoretical construct for research purposes by Kirkby and Schmitz [41]. The combustion chamber is a straight duct open at one end to a fast stream of oxidant and supplied at the other with fuel through a semi-permeable membrane. A sketch is provided in figure 1.4(a). All transport processes are one-dimensional with the oxidant counter-diffusing against the flow of products to the planar reaction sheet. In such a simple configuration, analytical solutions can be found for the governing equations and numerous stability models have been developed using this system [42, 43, 44, 45, 46, 47]. These models predict a planar stable flame sheet when far from extinction. Unfortunately, this burner is impossible to realize in practice because of the perturbations induced by the fast stream required to remove the products and supply the oxidant above the chamber. Therefore, these theoretical models remain without quantitative experimental validation.

The opposed jet flame presented in figure 1.4(b) has been used extensively to generate flat diffusion flames. The strain induced in the flame as the products are forced radially makes this configuration useful for the investigations on the effects of strain on the chemistry [48, 49], extinction limits [50] and stability of diffusion flame [51]. The unavoidable nature of this strain, its high magnitude and its stabilizing effect implies that this configuration is of limited use to study thermal-diffusive instabilities.

Low strain diffusion flame have been generated close to the forward stagnation point of porous cylinders and hemispherical caps [52], injected with fuel and placed in a slow stream of oxidant. A sketch is presented in figure 1.4(c), for a review of various counterflow diffusion flame configurations see [53]. With great care, the strain rate can be kept as low as 1.4 s^{-1} [52] by using a large radius porous injector. Using this type of burner, thermal-diffusive instabilities were observed close to the extinction limit showing qualitative agreement with numerical models [54]. The influence of hydrodynamics is still important in this burner and prevents the formation of durable instability patterns, making comparison with theoretical models difficult.

A novel research burner configuration was recently introduced [55, 56] that allows the creation of flat one-dimensional nearly-unstrained diffusion flames. In this thesis, the original experiment is improved and a new symmetrical version is built. A sketch of the original configuration is presented in figure 1.4(d). In designing this burner, great care was taken to reduce to a minimum all causes of flame stretch: aerodynamic straining, flame curvature and flame/flow unsteadiness [57]. The resulting flame is ideally well suited to study thermal-diffusive instabilities uncoupled from parasitic effects. The results gathered during this thesis and presented here will allow the first quantitative experimental validation of the theoretical models developed in the simplified one-dimensional counter-diffusing configuration of figure 1.4(a). Such comparison enables the identification of the critical simplifying assumptions made during the theoretical developments and their influence on the models precision.

1.3 Objectives and scope of the thesis

The main objective of this thesis is to further develop and characterize the novel quasi-unstrained one-dimensional counter-diffusion research burner recently introduced by the Laboratory of Fluid Mechanics at the Swiss Federal Institute of Technology Lau-

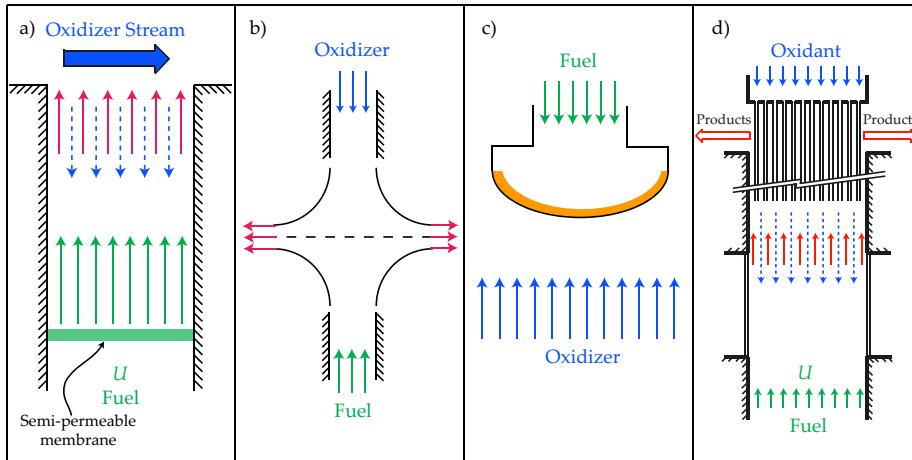


Figure 1.4: Non-premixed burner configurations. (a) Idealized unstrained one-dimensional chambered flame model. (b) Opposed jet counter-diffusion configuration. (c) Low-strain hemispherical cap burner. (d) Novel quasi-unstrained counter diffusion burner, the design used and improved in this thesis.

sanne (EPFL-LMF) [55, 56]. Improvements are implemented on the existing version (Mark I) and a new version is designed and constructed (Mark II). The new version features a symmetric design that allows control over bulk flow magnitude and direction across the flame sheet. These unique experimental facilities are used to quantitatively validate theoretical models of diffusion flame stability developed in the idealized one-dimensional configuration of figure 1.4a).

The comparison between experiment and theoretical models necessitates the implementation of specific measurement techniques. A necessary preliminary objective of the present work is therefore to select and implement measurement techniques suitable to gather data useful for the validation of theoretical models. Mass spectrometry is used in order to quantify the effective mixture composition supplied to the burner and the species concentration profiles across the burning chamber.

The scope of the work presented here is the experimental investigation of thermal-diffusive instabilities of unstrained diffusion flames. The unique experimental facilities developed during this thesis offer vast possibilities for original research in the field of combustion. The present investigation will be limited to thermal-diffusive instabilities resulting in the formation of a cellular flame pattern or in planar intensity pulsations.

1.4 Contributions

Novel research burner configuration, description and characterization

Chapters 4 and 6: the recently introduced unstrained counter-diffusion burner has been improved and measurements have been carried out to verify that it is indeed a good approximation of the idealized one-dimensional flame configuration. The working principles of the burner are described and the flame produced characterized as a function

of the operating parameters.

Work partially published in U.S. Combustion meeting, 2007 and International Symposium on Combustion 2008. Accepted for publication in Proceedings of the Combustion Institute, vol. 32, 2009. Detailed configuration description and characterization to be submitted to Combustion and Flame.

Mass spectrometer calibration procedure over a wide concentration range

Chapter 5: through the use of a semi-automated gas mixture generator and the development of a novel calibration procedure, an inexpensive mass spectrometer has been calibrated to drastically improve its accuracy for the quantitative measurement of complex mixture composition over a wide concentration range.

Work to be submitted to Measurement Science and Technology.

Mapping of Lewis number parameter space and scaling of the instabilities

Chapter 7: the use of a two-inert dilution mixture allows the mapping of extended regions of the Lewis number parameter space for instabilities while keeping mixture strength roughly constant. Using the same oxidant and fuel allowed the generation of the first experimental stability map of a diffusion flame in the absence of any hydrodynamic effects. The experimental measurements carried out in both cellular and pulsating flames describe the scaling of the instability properties as a function of the physical parameters of the flame.

Work to be submitted to Combustion and Flame.

1.5 Thesis Outline

- Chapter 2 reviews the literature on theoretical, experimental and numerical investigations of the instabilities of unstrained diffusion flames. The focus is on providing the state of the art rather than giving technical details on the various approaches used.
- Chapter 3 deals with theoretical considerations relevant to the present investigation. The simplified one-dimensional counter-diffusion flame construct used to develop theoretical models is presented. Since this thesis is principally experimental in nature, the theoretical developments presented will be limited to the minimum necessary to properly compare the models with the experimental results.
- Chapter 4 presents the experimental facilities used. The improvements implemented on the Mark I burner are presented. Design choices made for the Mark II version are explained and the construction process is described. The equipments used for mixture preparation, velocity and temperature measurement are described.
- Chapter 5 covers the extensive developments that were made for the calibration of the mass spectrometer used. A novel calibration procedure is introduced to

account for the intrinsic non-linearities of this type of instrument over the wide mixture concentration ranges encountered in this experiment.

- Chapter 6 covers the measurements that were made to characterize this new burner configuration and verify that it is indeed a good approximation of the idealized one-dimensional configuration.
- Chapter 7 presents the measurements that were made on the thermal-diffusive instabilities. The influence of the Lewis number is studied by diluting the reactants in a two-inerts mixture. A mapping of instabilities and extinction limits in the Lewis number parameter space is shown. Finally, the cell size and pulsation frequency scaling in unstable flames is treated, as a function of both the Lewis numbers and bulk velocity.
- Chapter 8 provides conclusions and future research perspectives opened by the novel experimental facility presented here.

Chapter 2

State of the art

The subject of instability in combustion has generated an extensive and diversified literature. The current presentation will be limited to the subject of thermal-diffusive instabilities, with a clear emphasis on the non-premixed configurations. The interested readers are directed to the broader reviews of the field by Sivashinsky [26], Buckmaster [27], Clavin [28] and Matalon [29]. As the review articles presented above clearly show, research in the field of combustion instabilities has focused until recently on premixed rather than diffusion flames.

This imbalance between the premixed and non-premixed configuration probably resides not in a lack of interest but rather in the difficulty to observe thermal-diffusive instabilities in simple diffusion flames suitable for analytical treatments. Cellular structures in premixed flames have been noticed a long time ago on Bunsen burners [58, 59] and later recognized as part of the greater family of thermal diffusive-instabilities [60, 61]. The ability to generate flat premixed flames in the controlled conditions of the laboratory using a uniform flow kept equal to the laminar flame speed then sparked the intensive research using this configuration mentioned in the review articles listed above.

The first experimental evidence of thermal-diffusive instabilities in a non-premixed flame came much later, with the work of Garside & Jackson [62]. Since then, research on the instabilities of diffusion flames has gained momentum. This is especially true for in the past two decades, when the push to reduce emissions meant that combustion systems tend to be operated with partially premixed lean mixtures, making them more prone to develop this type of instability. This chapter is divided as follows, first the literature is reviewed for theoretical investigations will be presented, followed by the experimental and finally a glimpse at the numerical approaches used will be shown.

2.1 Theoretical studies

Before Garside & Jackson [62] made their first documented observations of cellular instabilities in diffusion flame, the non-premixed received some attention from theoreticians. The term diffusion flame was introduced by Burke and Schumann [63] in their landmark paper of 1928 in which they studied the flames formed between concentric and co-flowing streams of fuel and oxidant. At the time, they did not report previous theoretical investigation on the properties and shape of diffusion flames. They devised a simple theory, assuming constant velocity, equal diffusion coefficients for the two species and one-dimensional transport (radially). They also did not treat the

chemical kinetics part of the problem and collapsed the reaction zone to an infinitely thin surface. Bypassing the internal structure of the reaction zone in the analysis greatly simplified the problem. Using these assumption they achieve good agreement for flame shape between their theory and experimental flames formed using hydrogen, city gas or methane as the fuel and air as the oxidant.

Later, Zeldovich [64] performed a more complete investigation of the combustion of initially unmixed gases in a similar configuration. He added the assumption that both reactants molecular diffusivities are equal to the thermal diffusivity, resulting in both Lewis numbers being equal to 1. Using a burner configuration analogous to the one of Burke and Schumann [63], he obtained theoretical results for the species and temperature distribution at the flame, showing that they were the same as for a prepared mixture in stoichiometric proportions. He also demonstrated that contrary to premixed flames where the reaction rate is determined by the physico-chemical properties of the reactants, in diffusion flames the reaction rate can be limited by the mixing rate between the reactants.

To study the unperturbed diffusion phenomena controlling the dynamics of these non-premixed flames, a one-dimensional theoretical construct was later introduced by Spalding et al. [65, 66]. It is a variation of this configuration that is created experimentally in the novel burner developed for this thesis. The theoretical model Spalding & Jain developed uses again the assumption of unity Lewis numbers, referred to as the *normal diffusion assumption* (NDA), but considers temperature dependent transport properties and finite rate chemical kinetics. The maximum reaction rate was determined and compared to an analogous premixed flame and the extinction limits were found. The authors concluded that the maximum reaction rate can probably be predicted by the Zeldovich-Spalding theory but point out the lack of experimental validation, especially regarding fuel leakage through the flame. This idealized one-dimensional flame configuration has been used extensively since then to develop increasingly complex theoretical models and will be described in detail in chapter 3.

The early models described previously used broad assumptions and were aimed at predicting basic flame parameters such as shape, reaction rate, temperature and extinction. Subsequent models either pursued broader goals or grew in complexity, accounting for more variables and relaxing some assumption. Kirkby & Schmitz [41] were the first to tackle the task of studying theoretically the stability of the planar diffusion flames formed in the idealized one-dimensional configuration. They considered the sensitivity of the model developed by Spalding & Jain [66] to infinitesimal disturbances, using constant transport properties and allowed the Lewis number to be different than unity. They found that the stability of the steady burning state to small perturbations must be analyzed and demonstrated a reduction in the domain of possible burning mixture caused by instabilities. More precisely, they identified temperature oscillations in mixtures with Lewis number above unity as a possible mechanism for extinction. Kirkby & Schmitz [41] used numerical methods on the model to obtain these results. At the time, computing power was scarce and expensive, limiting the amount of parameters that could be investigated simultaneously. More modern numerical approaches to thermal-diffusive instabilities in combustion will be presented in section 2.3.

The introduction of activation energy asymptotic, notably through the work of Liñán [67, 68], yielded results covering the entire range of Damköhler number, from the Burke-Schumann limit of infinitely fast chemistry down to extinction. The Damköhler number D_a is the ratio of the characteristic residence time to the characteristic chemical time and is used extensively to characterize the intensity of the chemical reaction

in a burning flame. Such analyzes yield the precise location of the reaction zone that can be treated as a thin reaction sheet. Plotting the maximum flame temperature as a function of the Damköhler number yields the typical S-shaped response curve of the flame. Traveling along the curve with increasing D_a , the flame condition jumps from a frozen-flow ignition regime to a near-equilibrium diffusion controlled regime where a thin reaction zone sits between two regions of equilibrium flow. In between those two extreme regimes, intermediate states with significant leakage of reactants through the reaction zone exist in which instabilities can occur. This leakage was demonstrated by Liñán to occur at low D_a in non-premixed flames, where the mixing rate can exceed the reaction rate, implying that one or both reactants can pass through the flame front without reacting completely. Response curves and their uses will be discussed further in section 3.2.1.

The use of large activation energy asymptotic allowed many parameters to be considered simultaneously in theoretical models. One of the first such theoretical investigation to be applied to the idealized one-dimensional configuration is that of Matalon & Ludford [69] who obtained explicit response curves for the whole range of D_a . Their asymptotic treatment of Kirkby and Schmitz's problem included a wide range of parameters that were initially overlooked because of the huge computing power requirements of the numerical method initially employed. Apart from the more complete response curves, their main results included explicit formulas for the extinction and ignition points.

At the time, the theoretical models on laminar diffusion flames mentioned above were considered to be more or less without practical applications since in practice most combustion occurs in turbulent flows with fuel and oxidant at least partially premixed. This view changed following the work of Peters [70] which views a turbulent diffusion flame as an ensemble of laminar diffusion flamelets. In this perspective, the counter-flow laminar diffusion flame used in the theoretical studies mentioned above becomes a representative configuration to investigate the behavior the laminar flamelets. These flamelets are then used to model the partially premixed turbulent combustion regime present in most practical applications. The flamelet model accounts for the fact that in partially premixed turbulent flames, the local diffusion time scales can vary considerably, locally lowering D_a and breaking the fast chemistry assumption, leading to non-equilibrium effects such as increased pollutants or soot formation.

Since then, numerous research groups have investigated the stability of diffusion flames using the planar flame produced in the simplified one-dimensional configuration as the base state. Among the most notable and active ones are those of Matalon [44, 71], Kim [42, 72] and Miklavcic [73, 74]. Each group used a slightly different theoretical burner configuration, set of boundary conditions, simplifying assumptions and mathematical treatment, yielding different results. The crux of their approaches involves taking the Zeldovich number Θ (the ratio of the activation energy to the thermal energy, also called the activation-energy parameter) as a large perturbation parameter to perform activation-energy asymptotics. The detailed stability model formulation being outside of the scope of this work, the interested reader is referred to the above listed papers themselves for further details. Our work will be compared primarily to the models developed by Matalon et al. [44, 71] because they include effect of a relatively large number of control parameters on the stability of an unstrained 1-D diffusion flame with finite rate chemistry. For example, they allow for both Lewis numbers to be different than one as well as unequal while the other models assume equal Lewis Numbers or a

single *effective*¹ Lewis number.

Their results will be used extensively in this thesis which aims to provide the first experimental results allowing validation of these models. Most of the works cited above focused in identifying the regions on the S-Curves where instabilities can occur and investigating the nature of these instabilities. The highlights of these papers is that as the Damköhler number is decreased, bringing the flame closer to extinction, instabilities can arise from the competing mechanisms of thermal and molecular diffusion. These instabilities can result in stripped quenching patterns (cellular flames) or intensity pulsations. The type of instability, if they occur at all before extinction, will depend on the Lewis numbers of both the fuel (Le_f) and the oxidant (Le_o) which are defined as the ratio of thermal to molecular diffusivities.

All of these research groups generally predict cellular type instabilities for Lewis numbers below 1 and intensity pulsation for Lewis numbers above 1, with slight variations in critical Lewis numbers depending on other flame parameters such as mixture strength ϕ . According to the work using linear stability theory carried out by the Matalon group, the cell size is expected to scale with the diffusion length l_d , which is defined as D_{th}/U , divided by the critical wavenumber in the marginally stable state, σ^* [44]. In a similar manner, the pulsation frequency is also expected to be well defined and scale with D_{th}/U^2 multiplied by the critical frequency ω_I . Kukuck and Matalon predicted that the pulsation frequency should be in the range of 1-6 Hz for typical experimental flames [71]. A recent paper by Wang et al. [75] presents a detailed mapping of the pulsation instabilities, using bifurcation analysis based on the asymptotic approach of Cheatham and Matalon. They predict that stable oscillations are possible in a restricted parameter range. These oscillations can either stabilize by themselves or grow in amplitude and lead to flame extinction.

2.2 Experimental studies

Thermal-diffusive instabilities have been observed since the late 19th century in pre-mixed flames through the polyhedral structure they confer to Bunsen flame in certain burning conditions [58, 59]. The first evidence that this type of instability can also occur in diffusion flames came up much later in 1951 and is attributed to Garside and Jackson [62], who were originally investigating polyhedral flame structures in the pre-mixed configuration. They noticed that when the reactants are provided separately to an axi-symmetric jet burner, a polyhedral flame structure can be observed if the fuel, hydrogen in this case, is mixed with an inert gas. Since these first chance observations, many experimental investigations have been aimed specifically at thermal-diffusive instabilities in diffusion flames.

Using a splitter plate burner, Dongworth and Melvin [76] also observed cellular pattern at the base of diffusion flames close to the lean extinction limit. They postulated that these instabilities were caused by fuel leaking through the base of the flame and forming a composite premixed/diffusion flame where instabilities could develop on the premixed side. Later Ishizuka and Tsuji [77] observed striped quenching patterns in diffusion flames formed at the forward stagnation surface of a porous cylinder. The fuel is inserted through the cylinder that is placed in a stream of oxidant. Using hydrogen as

¹Following this approach [72], the effective Lewis number is determined from the Lewis numbers of both reactants weighted by the mixture strength. Information is lost in this process because the same effective Lewis number can be produced from different combinations of the reactants Lewis numbers and result in different stability characteristics.

the fuel and air as the oxidant, they observed cells when the fuel was diluted in nitrogen or argon, but not when diluted in helium. They argued that the cells were caused by preferential diffusion of H_2 relative to O_2 . Cells occurred when the flame was located on the fuel side of the stagnation layer and were prevented when the flame moved to the oxidant side.

A exhaustive review of the counterflow diffusion burner configurations available for research purposes was presented by Tsuji [53]. Some of these burners were illustrated in figure 1.4. The burner types that are treated in this paper are: the opposed jet flame, opposed matrix burner, flames located at the forward stagnation point of a porous hemispherical cap, and flames located at the forward stagnation point of a porous cylinder, also called the Tsuji burner. The author presents the characteristics of each burner but very little is said about the potential of each configurations for research aimed at thermal-diffusive instabilities, save a mention of striped quenching pattern observed before extinction in the Tsuji burner with some reactant compositions. It should be noted however, that all of these burner types induce a significant strain on the flame. Little has changed since then so far as burner configurations are concerned, except a few improvements aimed at reducing the strain experienced by the flame. A notable improvement is of course, the recent introduction of the burner configuration used in this thesis.

With the rise in interest towards diffusion flames in the last two decades, more systematic experimental investigations on thermal-diffusive instabilities in this configuration were realized. One of the first such study is that of Chen et al. [78], who used a slot-jet (Wolfhard-Parker) burner with a wide variety of fuels and inerts to produce cellular flames. The authors point out that the choice of the burner configuration was guided by the flame strain in opposed jet flames inhibiting cellularity and axisymmetric burners of the type used by Burke and Schumann exhibits curvature effects that also perturb the instabilities. Their results include maps of where cells were encountered as a function of the inert used, the oxidant concentration and the flow velocity. They concluded that the non-premixed instabilities observed were similar in nature with the cellular instabilities observed in premixed flames. They were observed close to extinction when leakage and intermixing are expected to be significant across the flame front. The cellular instabilities are associated with conditions where the Lewis number of the more consumed reactant is sufficiently below unity, a threshold that they estimated at about $Le \approx 0.8$.

In a recent paper by Han et al. [52], great efforts were taken to reduce as much as possible the strain in a flame formed at the forward stagnation point of a porous hemispherical cap immersed in a stream of oxidant. To do so, a sintered porous burner of very large radius (5.22 m) and a very low speed oxidant stream were used. However, since the combustion products are still evacuated radially, the flame is strained. The magnitude of the strain is evaluated on the order of $K_s \approx 1.4s^{-1}$ in the center of the burner, but was not evaluated across the whole burner cross-section and the effect of curvature was not included. Using methane diluted in nitrogen, they observed holes and stripes in the flame sheet. The stripes they observed were always aligned along the unstrained tangential direction and being advected radially outwards by the bulk flow of products. This indicates at least some aerodynamic effects on the instabilities they generated since no static flame patterns were observed. The flame stability was plotted as a function of the nitrogen dilution and the fuel injection speed, identifying regions where cellular instabilities occur. However, no mention of the Lewis number of the reactants, their variations or their effect of the flame patterns observed were made.

Within the Laboratory of Fluid Mechanics (LMF) at the Swiss Federal Institute of

Technology in Lausanne (EPFL) our research group has been active in experimental investigations of thermal-diffusive instabilities in diffusion flames. Using methane and propane flames, Furi et al. [79] observed thermal-diffusion induced pulsations in a axisymmetric jet flame. These heavy fuels with oxygen diluted in nitrogen allowed the Lewis numbers to be above unity, enabling the onset of this type of instability close to extinction. The occurrence of pulsation instabilities was mapped as a function of the jet velocity and the oxygen content of the oxidant stream. The observed pulsation frequencies were in the order of a few Hz.

Cellular flames were also observed and investigated in the same axisymmetric jet burner and in a two-dimensional slot burner (Wolfhard-Parker). Lo Jacono et al. [80] considered the effect of both reactants Lewis numbers and the initial mixture strength on the cellular patterns found, in addition to the parameters considered in the papers presented above. The regions where cellular flames formed close to extinction were plotted in the Lewis numbers (of both reactants) parameter space and as a function of both reactants initial concentrations in the supplied streams. Using H₂-O₂ diluted in CO₂, they found that when decreasing initial mixture strength, cells appeared over a larger portion of the parameter space. Depending on flow conditions, they observed between 1 and 6 cells on their 7.5 mm diameter burner. In the flames having between 1 and 3 cells, the pattern was rotating.

In a subsequent paper using the same configuration, Lo Jacono and Monkewitz [81] investigated the effect of numerous parameters on the cell size. These included burner geometry, injection velocities, mixture strength and reactant transport properties. The observed cellular pattern was carefully mapped in the reactant concentration-jet velocity for both the axisymmetric and slot burners. The scaling of the cell size was reported as a function of the vorticity thickness of the mixing layer where the flame is located and the Reynolds number based on the injection nozzle. A variation of the cell size was also observed as a function of the mixture strength ϕ , with the cells growing with increasing ϕ .

Our group recently introduced of a novel research burner configuration [55] that allows the creation of quasi-unstrained one-dimensional diffusion flames. This opened new research opportunities for the investigation of thermal-diffusive instabilities in diffusion flames in the absence of hydrodynamic effects. The first results in this new burner were published by LoJacono et al. [55, 56]. The results gathered covered the variation of the flame position as a function of mixture strength and a preliminary mapping of the instabilities as a function of the fuel and oxidant composition of the feed streams. However, drawback in the first version of this new design were pointed out, namely that a residual strain remained, inducing cell motion and that the effective mixture strength could not be determined a priori from the supplied reactants streams. Therefore, these results should be considered only qualitatively. One of the first tasks in the present thesis was modifying the experimental setup to allow quantitative measurements and comparison with theory.

2.3 Numerical methods

The recent advances in computer hardware that now provides colossal amounts of computing power at the disposal of research scientists has changed the way that numerical methods can be used in the field of combustion. The numerical results of Kirkby & Schmitz [41] were of limited scope because of the limited amount of computing power available at the time. Comparatively, the asymptotic methods available shortly

after allowed for models to include more parameters and yield analytical results for important flame characteristics (i.e. ignition and extinction).

However, using asymptotic methods to find the dispersion relation used in the modeling of the instabilities, as in the last papers listed in section 2.1, still requires substantial numerical treatment because the dispersion relations found are transcendental. This explains why many of the most recent work cited in section 2.1 include substantial numerical results. Modern computer hardware allows the free-boundary problem to be solved directly using numerical methods, an approach that permits inclusion of more parameters in the analysis that the asymptotic method, such as density variations [82]. Here will be presented a selection of recent numerical investigations on the stability of diffusion flame that will also benefit from the unique experimental results presented in this thesis for validation.

Direct numerical simulation work on pulsating flames by Sohn et al. [83] have revealed the occurrence of pulsations that can either decay or grow in amplitude and lead to flame extinction, depending on the Damköhler number before the perturbation. The authors suggested that the threshold Damköhler number, below which the flame cannot recover stability, could be used as a revised extinction criterion for diffusion flamelet library in the laminar flamelet regime of turbulent combustion. However, this analysis assumes that both Lewis numbers are equal and only a limited range of Lewis numbers has been investigated.

In a numerical simulation including the effect of more parameters, such as a variable density, Christiansen et al. [84] investigated thermal-diffusive oscillations in hydrogen and methane flames. They concluded that while all oscillations would ultimately lead to extinction, in certain flames this process could be slow enough to allow experimental observation. They also argued that oscillations in hydrogen flames would be too low in amplitude ($5K$) and too high in frequency (60 Hz) to be observed experimentally.

In the numerical study of cellular instabilities, striped patterns have been observed for Damköhler numbers slightly above extinction. Lee and Kim [85] reported that after the emergence of the cellular pattern, a further decrease in the damköler number results in a reduction of the number of cells observed on a two-dimensional opposed jet burner. Recently, Valär et al. [86] performed numerical simulations on the cellular pattern developing in axi-symmetric jet flames and reported good agreement with the experimental results of Lo Jacono et al. [80, 56]. However, no recent numerical results have been found that address cellular flames in the idealized one-dimensional diffusion flame that is the focus of this work.

The results obtained by Metzener and Matalon [45] will be used extensively in this work because their model is the most complete we have encountered and was developed for a burner configuration compatible with our experimental realization. It accounts for the effects of many parameters and covering regimes of both cellular and pulsating flames. Parameters considered includes both Lewis numbers, which can be distinct and different than 1, the initial mixture strength and the flow conditions. The instability map presented in figure 2.1 is reproduced from their work and shows the predicted regions where different types of instabilities are expected close to extinction, as a function of both Lewis numbers. The flame parameters for which this map was generated can be reproduced in our experimental burner and the results presented in this thesis will be compared to this numerical model. The same reference also provides other maps and general trends for different mixture strength and flow conditions, the validity of which can also be tested using our experimental methodology.

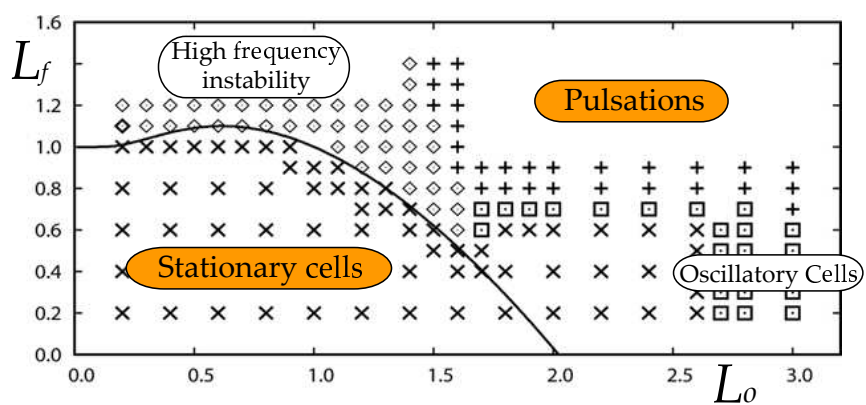


Figure 2.1: Detailed map of the instabilities expected close to extinction as a function of the Lewis numbers of both reactants, with an initial mixture strength of $\phi = 0.5$. Reproduced from reference [45].

Chapter 3

Theoretical considerations

In this chapter will be presented the fundamentals of the theoretical developments used in the models that this experimental study aims to validate. The details of the linear stability analysis are outside of the scope of this work and the interested reader is referred to the literature review of section 2.1 for a list of papers that covers this topic. The first section will present a simple model for the stable flame generated in the idealized one-dimensional counter-diffusion burner. The simplifying assumptions made will be listed and the main steps of the development explained. The results of interest are the theoretical species and temperature profiles as well as the relation for flame position. These will be used later to assess how well our experimental realization approaches the idealized theoretical construct.

The only aspect of stability theory that will be presented here is the response curve of the flame, which links the flame burning rate to the Damköhler number. This characteristic S-shaped curve is very useful to illustrate the mechanisms that lead to the onset of instability and flame extinction. Finally, numerical modeling was also employed in this thesis to provide stable flame structure data beyond the drastic simplifying assumption of the theoretical modeling. The strategy used was based on the Cantrea software package and will be detailed in the last section of this chapter. This tool was also used to determine the mixture transport properties from the measured composition and temperature data.

3.1 Simple one-dimensional model for the baseline flame

We start from the simplified theoretical model for the idealized chambered diffusion flame of figure 3.1(a) (see e.g. Cheatham & Matalon [44]). In the original configuration, one reactant (usually the fuel) is supplied from the bottom with a uniform velocity \tilde{U} , while the oxidizer is introduced from the top and reaches the reaction area solely by diffusion against the flow of products. The distribution of oxidizer and products is ‘magically’ kept uniform over the cross section by the fast top stream which removes combustion products and supplies reactant. In the following, this model is adapted to the more general symmetric configuration shown in figure 3.1(b) with arbitrary bulk flow magnitude and direction imposed.

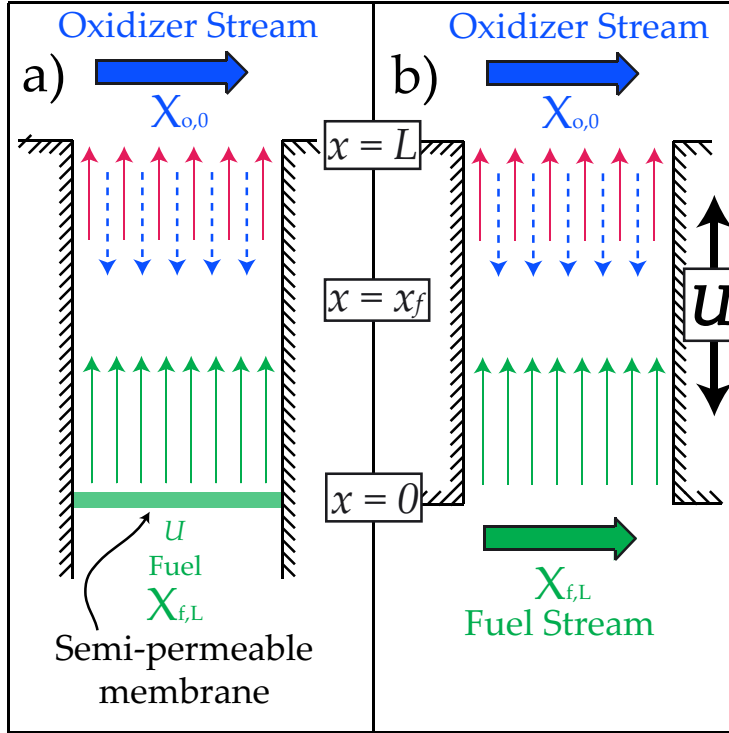
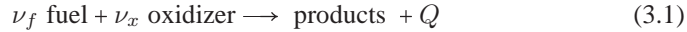


Figure 3.1: a) Conventional chambered diffusion flame. b) Symmetric chambered diffusion flame with reversible bulk flow.

3.1.1 Reaction-sheet approximation

In the symmetric configuration, the fuel and oxidant are introduced uniformly over the burner cross section at $\tilde{x} = 0$ and $\tilde{x} = L$, respectively. In the following, dimensional variables and unscaled mass fractions X are designated by $\tilde{\cdot}$. It is assumed that both reactants follow Fick's law of mass diffusion and burn in a global one-step irreversible reaction 3.1.



Next, we make the assumption of constant mass flux $\tilde{\rho}\tilde{U}$ and transport properties D_i , κ and C_p , independent of temperature. In addition, it is reasonable to assume that both reactants and the combustion products have identical mean molecular weight \bar{W} , thermal diffusivity D_{th} and specific heat C_p since both reactants are diluted with an inert (CO_2 in this case) that constitutes the bulk of the mixture. The steady-state dimensional equations of conservation of species are:

$$\tilde{\rho}\tilde{U} \frac{\partial \tilde{X}_o}{\partial \tilde{x}} - D_o \tilde{\rho} \frac{\partial^2 \tilde{X}_o}{\partial \tilde{x}^2} = -\nu_o W_o \tilde{\omega} \quad (3.2)$$

$$\tilde{\rho}\tilde{U} \frac{\partial \tilde{X}_f}{\partial \tilde{x}} - D_f \tilde{\rho} \frac{\partial^2 \tilde{X}_f}{\partial \tilde{x}^2} = -\nu_f W_f \tilde{\omega} \quad (3.3)$$

$$\tilde{\rho}C_p\tilde{U}\frac{\partial\tilde{T}}{\partial\tilde{x}} - \lambda\frac{\partial^2\tilde{T}}{\partial\tilde{x}^2} = \tilde{Q}\tilde{\omega} \quad (3.4)$$

Here ω is the chemical reaction rate, ρ the density of the mixture and W_f, W_o the molecular weights of the fuel and oxidant, respectively. The system is made dimensionless using the chamber length L as characteristic length and D_{th}/L as characteristic velocity. The reference temperature is \tilde{q}/C_p where $\tilde{q} = \tilde{Q}\tilde{X}_{f,L}/\nu_f W_f$ represents the heat released per unit mass of fuel consumed. The mass fractions of fuel and oxidizer, finally are scaled with the conditions where they are introduced: the fuel mass fraction by $\tilde{X}_{f,0}$ at $\tilde{x} = 0$ and the oxidizer mass fraction by $\phi\tilde{X}_{o,L}$ at $\tilde{x} = L$, where ϕ is the fuel-to-oxidizer equivalence ratio.

$$\phi = \frac{\tilde{X}_{f,L}/\nu_f W_f}{\tilde{X}_{o,0}/\nu_o W_o} \quad (3.5)$$

Invoking the large activation energy approximation, where it is assumed that no reaction occurs outside of a thin reaction sheet located at $\tilde{x} = \tilde{x}_f$, the dimensionless equations are obtained as

$$U\frac{\partial X_o}{\partial x} - Le_o^{-1}\frac{\partial^2 X_o}{\partial x^2} = -\omega\delta(x - x_f) \quad (3.6)$$

$$U\frac{\partial X_f}{\partial x} - Le_f^{-1}\frac{\partial^2 X_f}{\partial x^2} = -\omega\delta(x - x_f) \quad (3.7)$$

$$U\frac{\partial T}{\partial x} - \frac{\partial^2 T}{\partial x^2} = \omega\delta(x - x_f) \quad (3.8)$$

where $\omega\delta(x - x_f) = \nu_f W_f L^2 \tilde{\omega}(\tilde{x}) [D_{th} \tilde{\rho} \tilde{X}_{f,0}]^{-1}$. Here are introduced the Lewis numbers for the fuel Le_f and the oxidant Le_o , which are the ratios of the thermal to the molecular diffusivities.

$$Le_f = \frac{D_{th}}{D_f} \quad (3.9)$$

$$Le_o = \frac{D_{th}}{D_o}$$

with D_{th} the thermal diffusivity and D_f, D_o the molecular diffusivities of the fuel and oxidant, respectively. The Lewis numbers of both reactants will play a critical role in determining which type of instability, if any, can grow in the flame. The non-dimensional boundary conditions at the location of fuel and oxidizer injection at $x = 0$ and $x = 1$, respectively are

$$x = 0 : \quad X_f = 1, X_o = 0, T = T_0 \quad (3.10)$$

$$x = 1 : \quad X_o = \phi^{-1}, X_f = 0, T = T_L \quad (3.11)$$

To link the solutions across the flame sheet at $x = x_f$, equations (3.6) - (3.8) are integrated from $x = x_f - 0$ to $x = x_f + 0$ to yield the jump conditions

$$[[T]] = [[X_o]] = [[X_f]] = 0 \quad (3.12)$$

$$\begin{aligned} \left[\frac{\partial T}{\partial x} + Le_o^{-1} \frac{\partial X_o}{\partial x} \right] &= \\ \left[\frac{\partial T}{\partial x} + Le_f^{-1} \frac{\partial X_f}{\partial x} \right] &= 0 \end{aligned} \quad (3.13)$$

where the operator $[[\cdot]]$ represents the jump of the respective quantity across the reaction sheet (the difference between its value at $x_f + 0$ and $x_f - 0$). These jump relations (3.12) and (3.13) represent respectively continuity of all variables and the fact that the reactants have to reach the flame sheet in stoichiometric proportions to have complete combustion, i.e. to satisfy the boundary conditions $X_o(x = 0) = 0$ and $X_f(x = 1) = 0$.

3.1.2 Model results

The above model corresponds to the leading order of the activation energy expansion of Cheatham [44], with slightly different boundary conditions resulting from the finite chamber length, and represents a stable planar flame sheet. Solving equations (3.6) - (3.8) in each sub-domain $0 \leq x \leq x_f$ and $x_f \leq x \leq 1$ and applying the boundary and jump conditions (3.10) - (3.13) yields the flame position x_f given by equation (3.14) and the exponential species and concentration profiles (3.15) - (3.17), where T_f is the adiabatic flame temperature defined by the jump relation. The theoretical profiles obtained from this simplified theory applied to a stable lean flame ($\phi = 0.5$) are presented in figure 3.2.

$$\frac{e^{-ULe_f x_f} - 1}{e^{ULe_o(1-x_f)} - 1} = -\phi \quad (3.14)$$

$$X_o = \begin{cases} 0 & \text{for } 0 \leq x \leq x_f \\ \frac{1}{\phi} \frac{e^{ULe_o x} - e^{ULe_o x_f}}{e^{ULe_o} - e^{ULe_o x_f}} & \text{for } x_f \leq x \leq 1 \end{cases} \quad (3.15)$$

$$X_f = \begin{cases} \frac{e^{ULe_f x} - e^{ULe_f x_f}}{1 - e^{ULe_f x_f}} & \text{for } 0 \leq x \leq x_f \\ 0 & \text{for } x_f \leq x \leq 1 \end{cases} \quad (3.16)$$

$$T = \begin{cases} (T_f - T_0) e^{Ux} + T_0 e^{Ux_f - T_f} & \text{for } 0 \leq x \leq x_f \\ \frac{e^{Ux_f - 1}}{(T_f - T_L) e^{Ux} + T_L e^{Ux_f - T_f} e^U} & \text{for } x_f \leq x \leq 1 \end{cases} \quad (3.17)$$

It is interesting to notice in equation 3.14 that the flame position in the present finite length burner depends on the Lewis number of *both* species, in contrast to the semi-infinite configuration of Cheatham and Matalon [44] where x_f depends only on the Lewis number of the species which has to diffuse against the bulk flow. In our burner, when the bulk velocity is very small, both Lewis numbers become relevant for the determination of flame position since for both species diffusion plays an important role in transport towards the flame.

When the bulk velocity is high, equation 3.14 agrees with the expression given by Cheatham and Matalon [44] as one would expect. In the limiting case of vanishing bulk flow $U = 0$, the expressions (3.14) - (3.17) have to be evaluated with Hôpital's rule to yield the limiting flame position:

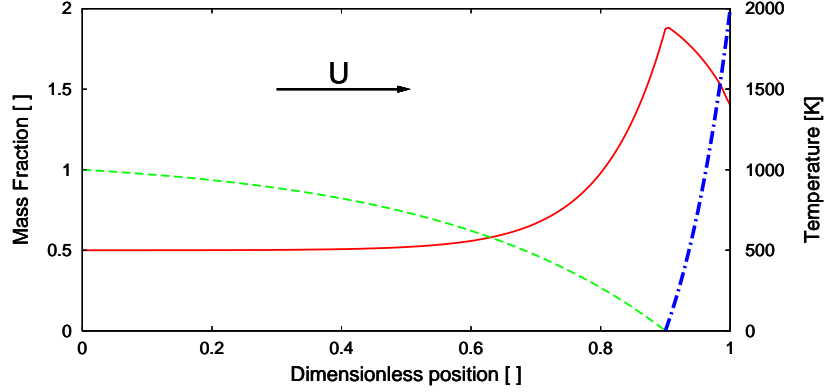


Figure 3.2: Theoretical species concentration profiles (fuel $---$, oxidant $- \cdot -$) and temperature ($—$) profiles obtained from the simplified one-dimensional model. The results shown are for a CO_2 -diluted H_2 - O_2 lean flame ($\phi = 0.5$) with a bulk flow of 20 mm/s.

$$x_f(U = 0) = \frac{\phi Le_o}{\phi Le_o + Le_f} \quad (3.18)$$

In this limit of a purely diffusive flame without bulk flow, the temperature and species concentration profiles become linear and will not be shown here.

3.1.3 Adiabatic flame temperature

In premixed flames, the calculation of the adiabatic flame temperature is a relatively straightforward process. Assuming a complete depletion of the fuel, one simply has to determine the amount of heat released and find the resulting temperature increase for the unburned species and the products. In the diffusion flame configuration used here, the situation is complicated by the fact that the amount of the counter-diffusing reactant that removes heat from the reaction zone is unknown. Considering the particular case of complete combustion with the oxidant counter-diffusing, simply taking into account the amount of oxidant consumed results in a large overestimation of the flame temperature.

In the theoretical treatments of the problem found in the literature, the adiabatic flame temperature is often determined using a relationship (dimensionless) of the form given in equation 3.19 [44]. This equation is valid for the case where the oxidant is the counter-diffusing species. The parameters used are $T_{-\infty}$, the temperature at the advected end of the chamber, ΔT the difference between the two supply temperatures, ϕ the mixture strength and Le_o the Lewis number of the counter-diffusing species. However, since this approach assumes constant transport properties, it results in a considerable underestimation of the flame temperature when compared to the experimental results available.

$$T_a = 1 + T_{-\infty} + (\Delta T - 1)(1 + \phi^{-1})^{-1/Le_o} \quad (3.19)$$

In this thesis, the adiabatic flame temperature was determined considering that the heat released by the combustion is used to raise the temperature of three species. The

first two are the inerts contained in the advected stream and the products of combustion. These are assumed to be raised to the flame temperature. The third contribution to the heat expenditure includes part of the supplied counter-diffusing species that never reaches the flame but is nonetheless heated above its supplied temperature. The choice of the temperature at which this last contribution is raised is somewhat arbitrary and has a huge influence on the resulting adiabatic flame temperature. The assumption used here is simply that the whole of the oxygen present at the counter-diffusing end of the burner is raised to a temperature halfway between the injection temperature and the flame temperature. This choice yielded results in very good agreement with the experimental results and the values obtained from the numerical models presented in section 3.3.

3.2 Stability considerations

Theoretical investigation of the stability of diffusion flames usually involves applying asymptotic methods to a simplified model similar to the one presented in the previous section. The linear stability analysis is often performed by introducing a small perturbing parameter in the stable base state [72, 44]. In these studies, it is customary to assume constant density to remove hydrodynamic effects from the analysis. The resulting dispersion relation reveals the nature and flame conditions under which instabilities can develop in unstrained diffusion flames. Important parameters that must be included in the analysis include both reactants Lewis numbers, the initial mixture strength ϕ , the temperature difference between the two ends of the chamber and the Damköhler number. This critical parameter can be used to characterize the burning state of a flame using the response curve concept that will be presented in section 3.2.1.

In the present thesis, the results of the group lead by Moshe Matalon will be used extensively because they include the effect of more control parameters [44, 71, 45]. Of special significance is the inclusion of both reactants Lewis numbers, which are allowed to be different from each other and different from unity. Other linear stability analysis often uses a single *effective Lewis number* which is derived from both reactants Lewis numbers weighted by the mixture strength [87, 73]. This operation, while simplifying the mathematics of the analysis, loses the information about the physical role of each reactant in the onset of the instabilities.

In the limit of infinitely fast chemistry, the Burke-Schumann limit, there is not leakage of reactants across the flame sheet and there is no real solutions to the dispersion relation with a positive growth rate, the flame is unconditionally stable. In the case of equal diffusion coefficients, where $Le_f = Le_o = 1$, the dispersion relation again admits no real positive growth rates and the flat flame is again unconditionally stable [44]. For all other cases of unequal diffusivities and finite-rate chemistry, instabilities can arise.

3.2.1 The response curve

A response curve relates the flame maximum burning temperature or reaction rate to some flame parameter such as the reactants initial temperature, bulk flow velocity, etc. It is used to visualize certain states of the flame, ignition, stable burning solution, instabilities or extinction. In this section, the response curve linking the flame reaction rate to the Damköhler number will be used to illustrate the parameters involved in the onset of instabilities close to the lean extinction limit of diffusion flames.

The Damköhler number \mathcal{D}_a is defined as the ratio of the residence time in the reaction zone to the chemical reaction time. The formulation of the Damköhler number can vary depending on the context it is intended to be used in. The form presented in equation 3.20 is applicable to the one-dimensional configuration used here and is taken from reference [44]. It covers the range of Damköhler numbers from an infinitely fast rate of burning, the Burke-Schumann limit at the high end, down to instabilities and extinction at the low end. This range is sufficient here since our interest is in the onset of instabilities from an initially stable flame and not with phenomena involving ignition.

$$\mathcal{D}_a = \frac{\lambda}{\rho_a c_p U^2} \left(\frac{R^0 T_a}{E} \right)^3 \frac{\nu_x c_p \bar{W}}{q R^0 \bar{W}_f} P \mathcal{B} X_{f,-\infty} \exp(-E/RT_a) \quad (3.20)$$

Response curves for diffusion flames are typically S-shapes with the three branches representing different burning regimes. They were first studied by Fendell [88] and Liñán [67], for a more recent and broader presentation, see [46]. A typical S-shaped response curve is shown in figure 3.3. On the bottom branch of the curve, the flow is nearly frozen, with a very small reaction rate. As the Damköhler number increases progressively, so does the reaction rate until \mathcal{D}_a reaches a critical value $\mathcal{D}_{a,I}$ corresponding to ignition. The reaction rate then increases in an infinite manner and the burning state jumps on the upper branch of the curve corresponding to intense burning rates. If \mathcal{D}_a is further increased, the system approaches the Burke-Schumann limit of infinitely fast and complete combustion. On the other hand, if \mathcal{D}_a is decreased the reaction rate will follow the top branch and decrease slowly until another critical value is reached, $\mathcal{D}_{a,E}$ corresponding to extinction. The system state then jumps back on the lower branch of the curve with nearly frozen flow. The central part of the curve corresponds to unstable states with a reaction rate decreasing with increasing \mathcal{D}_a that can therefore be considered physically unrealistic [46]. The portion of the top branch of the S-curve immediately before extinction is where the thermal-diffusive instabilities are predicted and observed.

In figure 3.4 is presented a close-up of the portion of the top branch of the S-Curve immediately adjacent to the extinction point. The solid red line represents stable burning states and towards the right, as \mathcal{D}_a is increased towards the Burke-Schumann limit, the flame temperature tends asymptotically to the adiabatic flame temperature. The dashed line represents unstable burning states with the transition point located at $\mathcal{D}_a = \mathcal{D}_a^*$ being a marginally stable state. It is between this critical value \mathcal{D}_a^* and extinction that the thermal-diffusive instabilities can develop and therefore it is there that the experiments should be conducted.

In our experiment, we would like to be able to move downward on the top branch of the S-curve to reach the unstable regime located immediately before extinction. The ways available experimentally to change the Damköhler number are limited and involve altering the characteristic flow time or the characteristic reaction time. The latter can be used to lower \mathcal{D}_a by reducing the flame temperature, either through increasing the reactants dilution while maintaining their proportions constant or simply by changing the mixture strength. Changing the dilution without changing the mixture strength ϕ is difficult because of the inherent complexity of our experimental configuration. In practice, it is difficult to predict the effective boundary condition on the counter-diffusive injection side resulting from a change in dilution level, as will be explained in section 4.1. Therefore, the most convenient way to decrease the Damköhler number in our experimental realization is to reduce the mixture strength by decreasing the amount

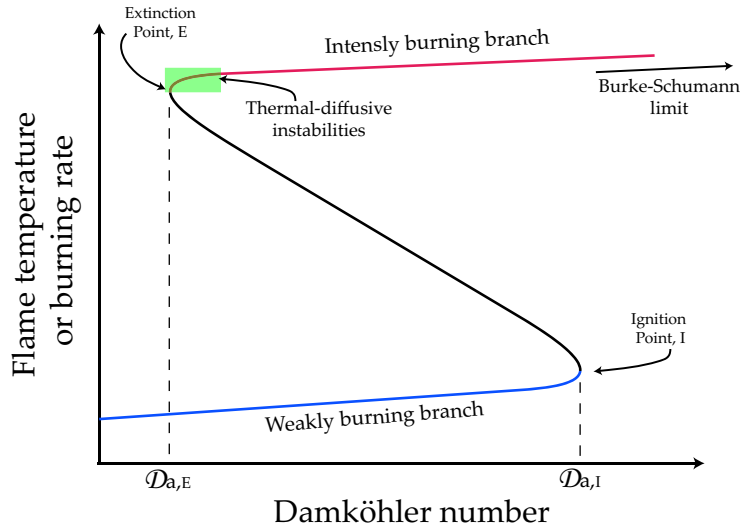


Figure 3.3: Typical S-shaped response curve linking the flame maximum burning temperature to the Damköhler number of the system. The square shaded region where thermal-diffusive instabilities are observed is enlarged in figure 3.4.

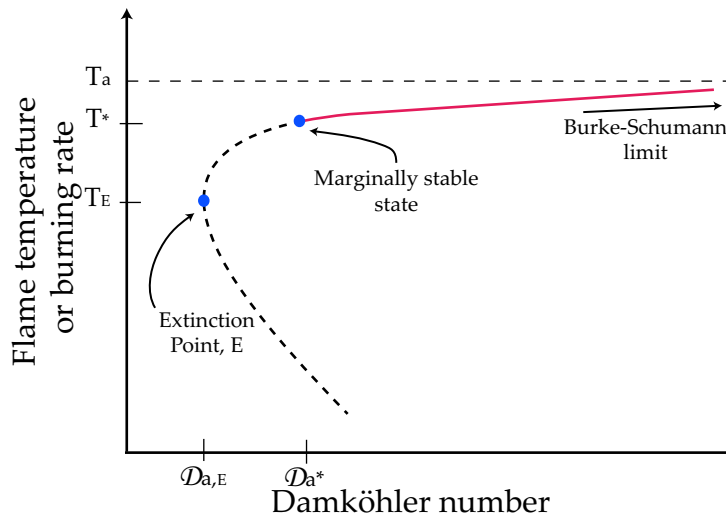


Figure 3.4: Enlargement of the S-curve region close to the extinction limit. The solid line represents stable burning states on the upper branch of the S-curve of figure 3.3. On the dashed line, between the marginally stable state D_a^* and extinction, are located the unstable states where thermal-diffusive instabilities can grow.

of fuel supplied in the fuel stream.

It is also possible and easy to change the residence time by changing the bulk flow. However, the range of experimentally achievable bulk flow is limited, ranging from very small values to about 30 mm/s. From the expression given in equation 3.20 we

see that \mathcal{D}_a varies as the inverse of the square of the bulk velocity and with the third power of the adiabatic flame temperature T_a . The inability to significantly increase the bulk velocity to reach the low \mathcal{D}_a where the instabilities are observed means that the flames are usually brought to instabilities simply by lowering the mixture strength to decrease the heat release, increasing the chemical reaction time.

3.2.2 Thermal-diffusive instabilities

The thermal-diffusive instabilities that can develop close to extinction in diffusion flames can take many forms, the distribution of which in the parameter space has been the subject many of the works reviewed in section 2.1. Of interest here are the instabilities that can be observed in the laboratory: mainly cellular flames and planar intensity pulsations. Other instability regimes are also expected from theoretical modeling, such as oscillatory cells at the transition between the two modes. The concept of a thermal-diffusive instability evolving on very fast timescales, comparable to the characteristic chemical time was also demonstrated by Buckmaster et al. [89].

The driving mechanism behind these thermal-diffusive instabilities is the differential diffusion between species and heat, both of which being necessary to sustain the combustion reaction. The ratios of these quantities, the Lewis numbers introduced earlier in equation 3.10, are the key parameters that will determine what type, if any, of instability that will develop as the Damköhler number is decreased to approach extinction. Naturally, if all diffusivities are equal, the flame is unconditionally stable to TD instabilities. However if they are not, there will be either an excess or deficiency in available enthalpy in the reaction zone.

The sketch presented in figure 3.5 show qualitatively the location of the regions of cells and pulsations expected in the Lewis number space. The figure is adapted from reference [29], with pictures obtained in this work inserted in the regions of cells and pulsations. The solid line represents the conditions where there is no excess or deficiency of available enthalpy h_f in the reaction zone. Above this line, there is a deficiency of enthalpy while below the line there is an excess of enthalpy. The vertical dashed line represents the effective mixture strength at the flame γ , with lean conditions having a negative γ on the left and the rich conditions on the right.

Generally speaking, when the Lewis numbers are below unity, the thermal diffusivity is smaller than the molecular diffusivity and since all the heat cannot be carried away, there is an excess of available enthalpy in the reaction zone. This situation favors the creation of a cellular flame pattern at low \mathcal{D}_a . The opposite situation where Lewis numbers above unity yields a deficiency of enthalpy close to the flame results in planar intensity pulsations. When considering the initial mixture strength, cells are more likely to occur in lean flames and pulsations in rich flames [45]. The high-frequency instability regions shown in figure 3.5 corresponds to the fast-time instability introduced by Buckmaster et al. [89] and intervenes on such small time and length scales that they are not expected to be observable in practice.

Stationary cellular flames are found when the fastest growing mode has a finite wavenumber and pulsation when this wavenumber is zero. In between those two domains, the two types of instabilities can co-exist, resulting in oscillatory cellular flames. Theoretical studies [44, 71] reveal that the typical size of the cellular patterns is expected to scale with the diffusion length $l_D = D_{th}/\rho c_p U$ divided by the critical wavenumber in the marginally stable state. In a similar fashion, the pulsation frequency should also be well defined and scale with D_{th}/U^2 multiplied by the critical frequency in the marginally stable state.

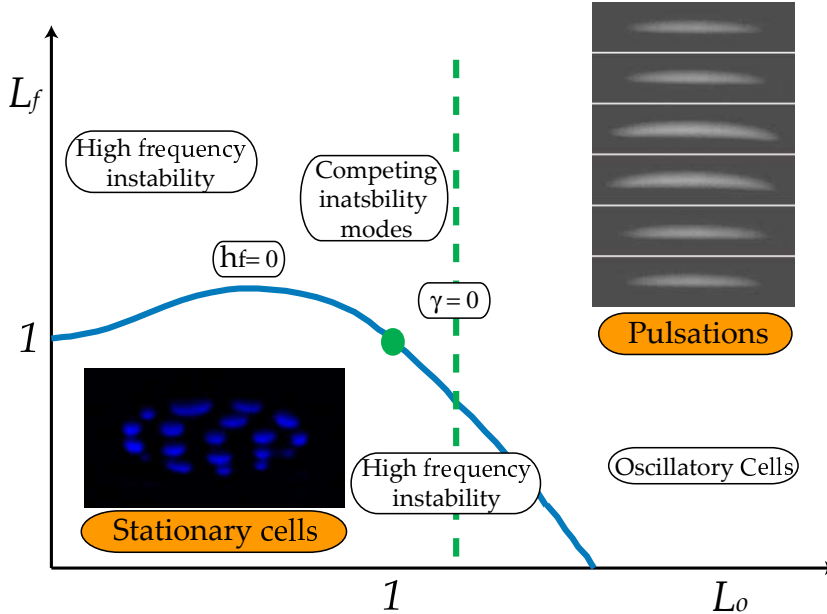


Figure 3.5: Qualitative sketch of the types of instabilities expected close to extinction as a function of the Lewis number of both reactants. This figure was adapted from reference [29]. The inserted pictures illustrated the cellular flames that will be discussed in chapter 7.3 and the planar intensity pulsations that will be discussed in chapter 7.4.

The locations of the various regions illustrated in figure 3.5 depends strongly on the flame parameters, especially the mixture strength. In a rich flame the graph is stretched along the vertical axis and compressed on the horizontal axis with lean configurations having the opposite effects. If the roles of the two reactants are inverted, with the fuel now having to counter-diffuse to the reaction zone, a similar map could be drawn. In this reversed configurations, the same regions would be found but their location would have to be flipped relative to a line passing through $Le_o = Le_f$.

3.3 Numerical tools

In this thesis, numerical tools were used to perform three tasks. First, to evaluate transport and thermodynamic properties for the complex gas mixtures encountered in this experiment. Second, to gather needed flame parameters, such as the maximum flame temperature without having to perform lengthy experiments for every flame configurations used. Finally, to calculate species and temperature profiles beyond the drastic assumptions of the theoretical model, allowing comparison with the experiment. The Cantera software package [90, 91] was used for all of these tasks. Cantera is an open-source (distributed under the BSD software license), extensible software suite created and maintained by D. G. Goodwin of Caltech. For the results presented here, Cantera was used only from within the Matlab environment.

The transport properties were evaluated using the NASA thermodynamic database for gas phase mixtures [92, 93]. Matlab code was written to interact with Cantera,

either through a command line or a GUI interface. From the supplied mixture composition and temperature data measured experimentally, the program returned the relevant mixture properties. Since at least one end of our burner is open to the atmosphere and the pressure drop in the exhaust path is very small, the pressure in the burning chamber was always assumed to be one atmosphere.

For all results presented here, the mixture composition at both ends of the burner was always measured or known from the prescribed gas stream. However, measuring the composition and temperature in the reaction zone itself where they are the most relevant to the analysis is difficult, lengthy and induces perturbations on the flame. Moreover, the mass spectrometry instrumentation implemented here to measure the composition in the chamber can only account for stable species. In the reaction zone where radicals are abundant, this can induce errors in excess of 10% [94].

When the mixture composition at the flame or the temperature data was not or could not be measured experimentally, these values were evaluated from a numerical model of the burner. Supplying the measured boundary conditions to this model and solving using the routines built into the Cantera package yielded the desired information about the conditions prevailing at the flame front. The reaction mechanisms used in this model for both the methane and hydrogen flames encountered in this thesis was GRI/Mech 3.0 [95]. This mechanism includes 53 species and 325 reactions. Although optimized to model methane combustion, this mechanism is also widely used for hydrogen combustion [95].

The use of numerical tools also allows to go beyond the assumptions used to develop the simple one-dimensional model for the baseline flame presented in section 3.1. Using the same numerical model provided results on flame position, species and temperature profiles that can be compared to both the simplified model and the experimental data. Numerical results are presented in figure 3.6 for the same stable flame that was used to generate the theoretical profiles of figure 3.2, which are also shown for comparison purposed.

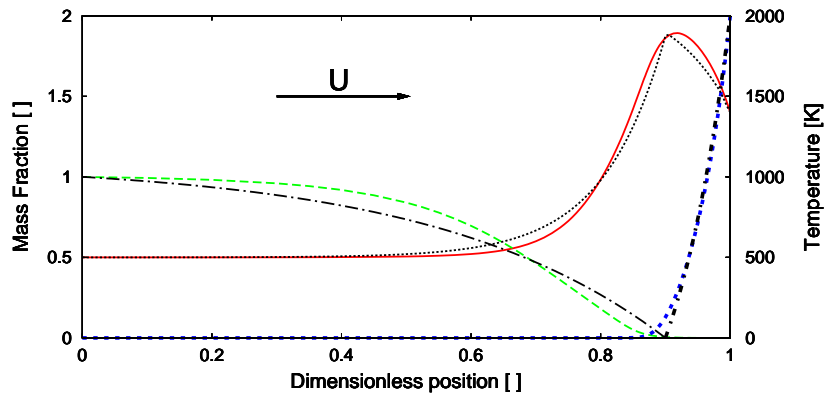


Figure 3.6: Species concentration (fuel $---$, oxidant $---$) and temperature ($—$) profiles obtained using the Cantera software package. The theoretical profiles from figure 3.2 are shown with the black lines. The results shown are for a CO_2 -diluted H_2 - O_2 lean flame ($\phi=0.5$) with a bulk flow of 20 mm/s.

The main differences between the two datasets is seen in the concentration profile

of the advected species and in the location of the flame front. These discrepancies are expected since in the theoretical model constant transport properties are assumed and evaluated at the flame conditions. The advected species being supplied at a temperature significantly lower than the flame temperature it is normal to see a poor accuracy of the theoretical model in this region. There is also a slight difference between the theoretical and numerical models regarding flame position. Again, this difference can be explained by a drastic assumption made in the simplified theory. By assuming that the chemistry is infinitely fast, the reaction zone collapses to an infinitely thin surface, which is not the case in reality or in the numerical model which accounts for finite-rate chemistry and results in a finite thickness flame sheet.

Chapter 4

Experimental facilities and methods

At the core of this thesis is the gathering of experimental data on the thermal-diffusive instabilities of diffusion flames in the absence of strain. In this chapter will be presented the experimental facilities and techniques that were used for this purpose. In the first section will be described the two burners featuring the novel species injection arrays that allow the creation of the sought after unstrained flames. A more lengthy description will be given for the second, or Mark II, version of the burner since it was built specifically for this thesis.

Subsequent sections will cover the experimental means that were implemented to probe the flame and measure its characteristic. First will be discussed the photographic and cinematographic techniques used to record flame shape and motion. Then the way the velocity and temperature profiles were measured will be presented. The last section will cover the mixture generation setup. An extensive suite of mass spectrometric techniques were also developed specifically for this thesis and because of its extent, this topic will be treated separately in the next chapter.

4.1 The burners

The main challenge when attempting to create an unstrained chambered flame is to supply the reactants and remove the products evenly across the reaction area. A novel way to address this problem and produce a truly unstrained flame has recently introduced at EPFL by Prof. Peter Monkewitz and successfully implemented [55, 96]. In this novel burner configuration, this difficulty is overcome by supplying the reactant through an array of closely spaced needles while allowing the products to escape between them. The result is a flame with very little residual strain which results mainly from temperature inhomogeneities in the supply and exhaust paths. This strain can be minimized and the supply configuration poses no restriction for the strain to be completely eliminated, contrary to burners where the products are evacuated radially. This unique configuration is ideally well suited to provide experimental validation for theoretical diffusion flame stability models and accordingly has been developed in close collaboration with Prof. Moshe Matalon who heads a very active research group working on the theoretical side of the problem.

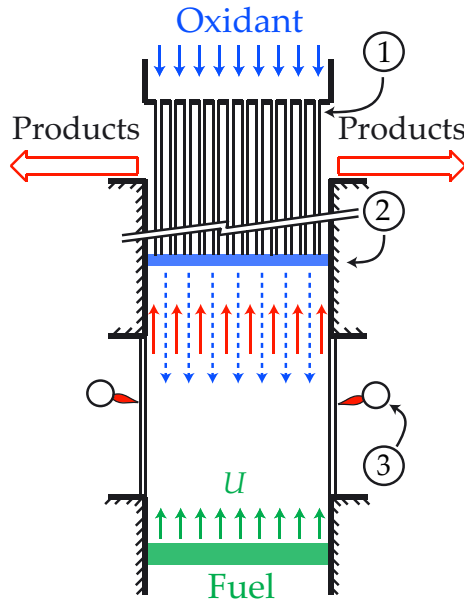


Figure 4.1: Schematic of the Mark I version of the burner. (1) The in injection array, (2) the injection layer and (3) the secondary burners.

4.1.1 Mark I burner

The first (Mark I) version of the burner was built by David Lo Jacono under the supervision of Peter Monkewitz, starting in 2003. The first results gathered in this unique burner were published in 2005 [55, 56]. No results generated in this thesis were gathered using this first iteration of the burner design as it was used for the publications listed above. The first results presented in this thesis and published in reference [96] were achieved using an improved version of the Mark I burner where great care at been taken to reduce the residual flame stretch.

A sketch of this modified version is presented in figure 4.1. The injection array, labeled (1) in the figure is made of 625 stainless steel hypodermic needles capillaries 210 mm long (Unimed S.A., Lausanne). The needles have a 1.0 mm outer diameter, a 0.1 mm wall thickness and are arranged in rows of 25 on a 1.78 mm Cartesian grid. The result is a 46×46 mm square cross section burner. The burning chamber is surrounded entirely by quartz walls, 3 mm thick. One pane features a 10 mm diameter hole to allow the insertion of an open flame for ignition. Immediately below the needles, there is a layer with localized tri-dimensional flow where the injected stream mix with the hot flow of products escaping upward from the reaction zone below. This layer is referred to as the *injection layer* (labeled (2) in figure 4.1) and since the needle spacing is small, the flow is expected to be strictly one-dimensional only a short distance below the tip of the needles. This introduces the problem that the mixture composition below the injection layer is not known *a priori* from the supplied gas streams since it a significant proportion of the mixture injected through the needle array can go straight back up the chimney with the flow of products, as illustrated in figure 4.2a). To obtain this information about the effective boundary conditions of the burner, mass spectrometry

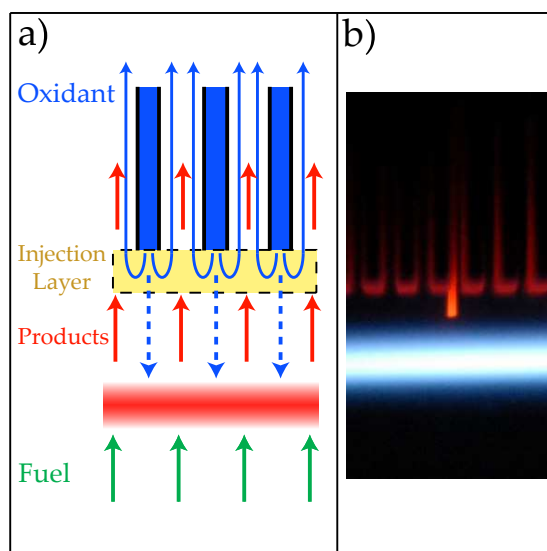


Figure 4.2: a) Detailed representation of the injection layer immediately below the tip of the needle array. b) View of the mass spectrometer capillary inserted to probe the mixture composition below the injection layer.

was used to sample the mixture composition throughout the burning chamber. This topic will be discussed in chapter 5.

In the top injection plenum the needles originate from, a porous metal filter creates a pressure drop high enough to ensure uniform conditions at the top of the array. The reactant advected from the bottom is inserted in the chamber after passing through a stabilization chamber and a flow straightener composed of closely packed 3.0 mm stainless steel tubes. Porous metal filters and other means to generate strong pressure drops were avoided to allow the flow to be seeded, enabling laser-based velocity measurements.

The initial measurements made in the Mark I version proved the validity of the concept, but revealed a number of problems in the implementation. Addressing these problems was the first task carried out in this thesis. Two main issues with the flame created compromised the quantitative comparison with the theory are illustrated in figure 4.3. In the first frame, significant curvature can be seen on the edges of the flame and the second frame illustrates the rapid cell motion observed in the pattern formed in unstable flames. Some asymmetry can also be noticed in the flame shape, with the left side of the flame appearing dimmer. Temperature measurements in the exhaust path revealed that one side was significantly colder than the other. This was caused by all hot components of the burner being attached to the support column from the same side. All of these components were made of metal (brass and aluminum) resulting in colder temperatures in the chimney on the attached side. A new symmetric attachment scheme was implemented that improved the symmetry of the flame shape.

The flame curvature was initially believed to be caused by heat loss at the windows in the burning chamber. To alleviate this problem, a set of secondary burners, labeled (3) in figure 4.1, were fitted on the outside of the burner, at the same level as the flame. A picture of the lit burner with the side burners in action is shown in figure 4.4. The

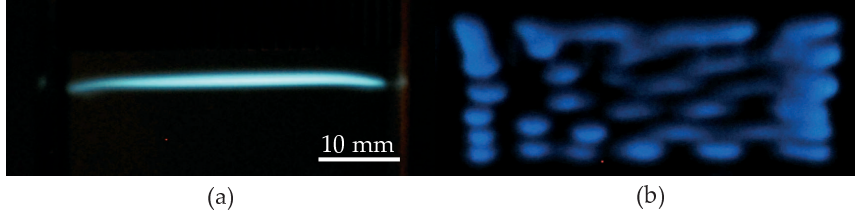


Figure 4.3: Typical pictures of flames from the unmodified Mark I version of the burner. (a) Stable flame seen from the side with noticeable curvature on the edges. (b) Unstable flame seen from below. The blur in the cellular pattern is caused by the residual flame stretch induced rapid motion of the cells.

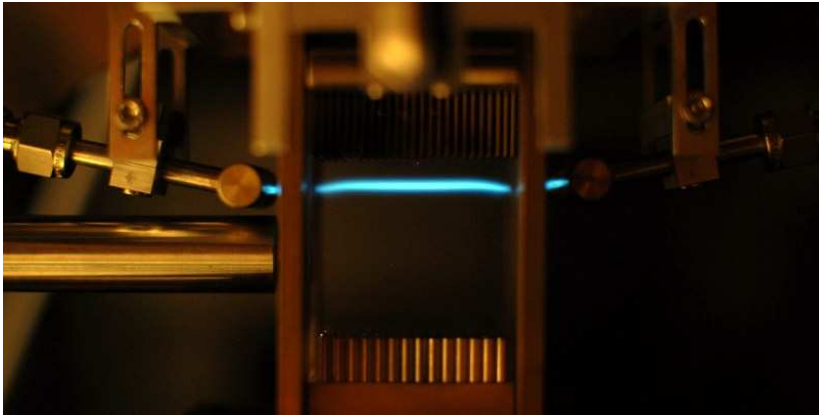


Figure 4.4: Picture of the improved Mark I version of the burner with a flat flame present and the lit secondary burners.

removal of the lateral support did improve the symmetry of the flame, but even with the side burners the flame curvature on the edges is still visible. This fact hinted that the cause of the curvature and residual strain was not in the burning chamber but rather in the exhaust path and injection layer. In both the initial experiment of Lo Jacono and in this modified version, the influence of a residual strain on the flame is revealed by the rapid motion of the cellular patterns observed close to extinction. The picture of figure 4.3b) shows this motion through the streaks and fuzziness of the cells capture with a moderately long exposure time of $1/10$ s. Velocity measurements made in the lit burner by Lo Jacono [56] showed an acceleration of the flow toward the sides of the burner. The residual strain was evaluated at the time to be on the order of 1.5 s^{-1} .

Several aspects of this first burner design are thought to contribute to the curvature of the flame edges and the residual strain observed. They can globally be referred to as wall effects since they all take their origins in inhomogeneities close to the chimney and burning chamber walls. First, since there is no row of half cylinder emerging from the chimney walls, the escape path between the last row of tubes and the walls offers a lower resistance to the flow of products that the space between two rows of tubes. Second, heat loss at the chimney walls, which are made of brass and not insulated,

implies that the flow in the colder region of the exhaust adjacent to the walls is less viscous. These two phenomenon have the effect of increasing the flow velocity on the periphery of the chimney and upper part of the burning chamber. This effect is clearly seen on the velocity measurements of Lo Jacono [56] and somewhat counter-balances the velocity boundary layer that develops on the burning chamber windows.

There is a third wall effect however that appears to be dominating the two others since it is the only one that can explain the curvature of the flame *downward* at the edges. From the temperature gradient in the chimney it follows that the supply needles routed through it will experience different pressure drops depending on their location. Needles on the edges are colder than at the center, about 20°C on average. The flow in the needles of the central core of the injection array being hotter and more viscous, the counter-diffusing reactant will exit the needles with a lower velocity at the center of the burner than on the edges. The result is that the effective mixture strength is not the same over the burner cross-section. In the case of the flame pictured in figures 4.3a) and 4.4 the excess of oxidant on the edges lowers the mixture strength and pushes the flame further from the injection array.

4.1.2 Mark II burner

The lessons learned from the experiments made in the Mark I version of the burner were extremely useful in designing the improved Mark II version. In this new version, all of the issues listed at the end of the previous section were addressed and corrected with some level of success. One important new feature was also added by inserting both reactants through needle arrays thus providing the possibility to allow the products to escape through both ends of the burning chamber. This gives simultaneous control over both the bulk flow magnitude and direction. This feature was implemented to allow the investigation of unstrained diffusion flames with very small bulk flow and eventually the limit situation where there is no bulk flow across the chamber, all transport being through diffusion only.

A schematic representation of the burner is provided in figure 4.5a). The injection arrays consist of $31 \times 31 = 961$ stainless steel hypodermic needles with an outer diameter of 1.2 mm and a wall thickness of 0.1 mm on a Cartesian grid with 2.5 mm spacing. Both arrays are introduced in a quartz walled burning chamber with a square cross-section of $77.5 \times 77.5 \text{ mm}^2$. The products are allowed to escape through a second set of $32 \times 32 = 1024$ tubes of 1.2 mm I.D. located between the injection needles. These extraction tubes are bent outwards to deliver the exhaust gas into annular exhaust plenums which are heated to prevent condensation in the exhaust manifolds resulting in non-uniform product extraction. To accommodate the two sets of needles, the spacing of the arrays was increased from 1.78 mm in the Mark I version to 2.5 mm in the Mark II version. The same diameter injection tubes (0.8 mm I.D., 1.0 mm O.D.) were used in both version due to geometrical constraints in the region of the chimney where both sets of tubes overlap. However, to ensure that the jets exiting the injection tubes had roughly the same speed in the two versions, a small section of larger diameter tube (1.0 mm I.D., 1.2 mm O.D.) was attached at the end of each injection tube. This compensated for the larger grid spacing and kept the injection layer in the two version geometrically similar.

The spacing between the two injection arrays is adjustable between 10 mm and 80 mm but for the results presented here was either 20 mm or 40 mm. Figure 4.5b) shown a photograph of the partially assembled burner. The symmetric arrangement of the product extraction manifolds exhausting into two plenums on both ends (not shown

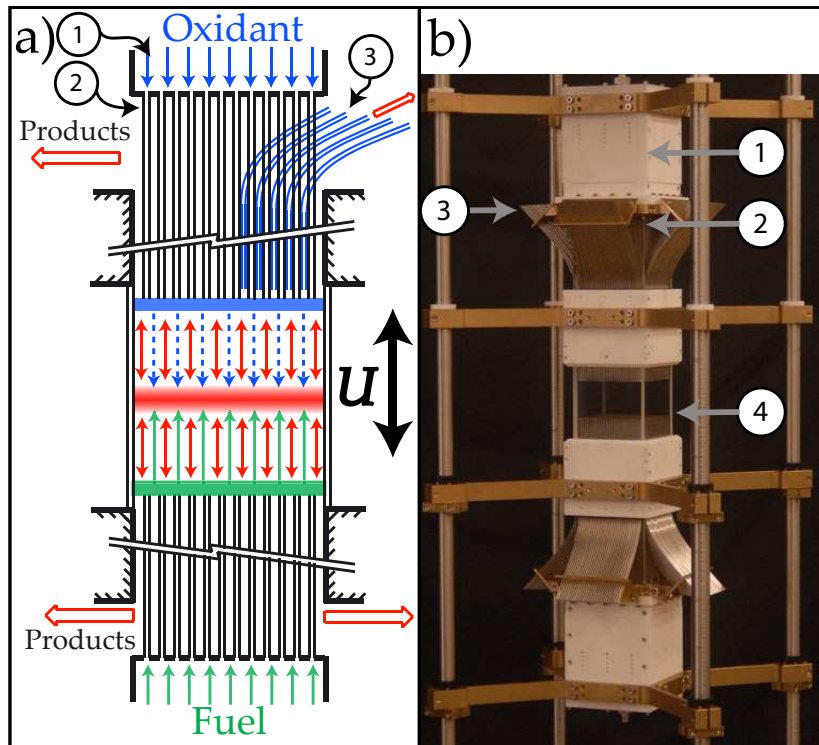


Figure 4.5: (a) Representation of the symmetric Mark II version of the burner; (1), Reactant injection plenums; (2), Straight injection needle arrays emerging from plenums; (b) Photograph of the partially assembled burner (without exhaust plenums and thermal insulation) with all needle arrays in place. (1) and (2), same as in (a); (3), Extraction needles bent outwards between injection needles; (4), Quartz-walled burning chamber.

on the photograph) allows control over both the magnitude and direction of the bulk flow through the flame by adjusting the pressure difference between the two exhaust plenums.

The use of the secondary array of extraction tubes to remove the products helped manage the wall effects that caused most of the undesirable features of the Mark I version. To account for the presence of the wall, the diameter of the last row of extraction tubes was reduced to provide roughly the same exhaust flow rate for each supply tube of the array. A sketch of the extraction and supply tubes configuration is provided in figure 4.6. Even if the tube diameters could only be chosen from a limited set of values available from our supplier, this improvement had a significant effect on the flame produced. The parasitic motion observed in the cellular flame produced was reduced drastically, hinting at a significant reduction of the residual flame stretch.

To further isolate the central portion of the burner from the walls where velocity, species and temperature gradients remains, a large diameter quartz tube was placed in the chamber. The tube covers the entire distance from the top to the bottom injection arrays. This creates two flames at the same position in the burning chamber, ensuring homogeneous temperature boundary conditions for the central flame. In figure 4.7a), a side view of the burning chamber is shown, with a 45 mm O.D. (43 mm I.D.) quartz

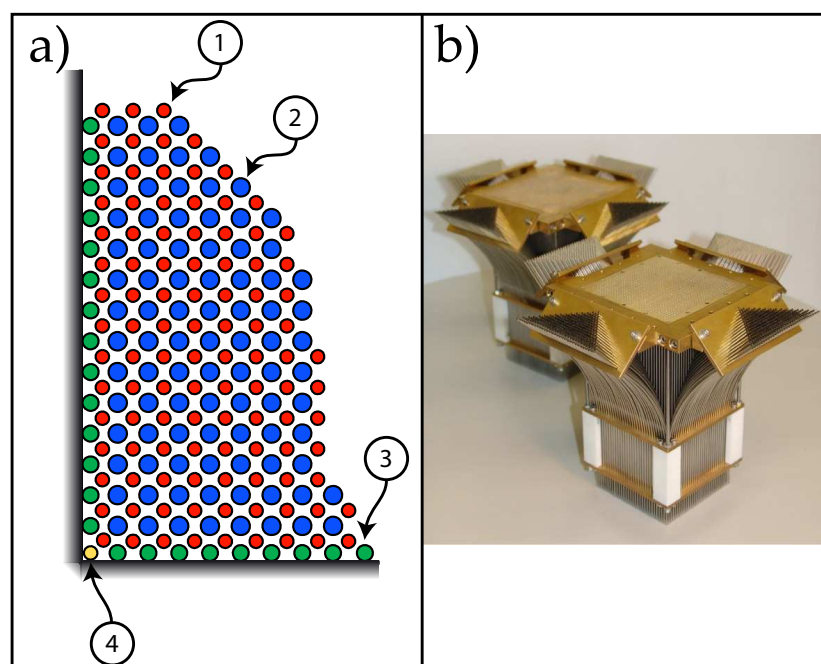


Figure 4.6: (a) Configuration of the injection and extraction tubes. (1) In red, the straight injection tubes (0.8 mm I.D., widening to 1.0 mm further down). (2) In blue, the extraction tubes, bent outward between the injection tubes (1.2 mm I.D.). (3) In green, the edge row of the extraction tubes (1.0 mm I.D.). (4) In yellow, the corner extraction tube (0.8 mm I.D.). (b) The two injection/extraction arrays fully assembled, each made of close to 3'000 stainless steel tubes each.

tube inserted. The presence of the tube ensures that only the velocity inhomogeneities caused by the boundary layers remain inside the cylinder where the experiments are conducted. The typical flame shape obtained in this setup is shown in figure 4.7b) with the central portion of the burner exhibiting remarkable flatness. Tubes with different diameters (35, 40, 45, 50, 55 mm O.D.) were custom made with thin walls of 1.0 mm (VQT S.A., Neuchâtel) for two chamber lengths (20 and 40 mm).

The other improvements implemented in the Mark II burner had a less spectacular result, although their combined effect contributes to the outstanding performance of the whole apparatus. To reduce the temperature gradient in the exhaust path, the chimney walls were made of machinable ceramics (Macor, Corning Inc., New York, USA) to reduce heat conduction. The chimney was also insulated from the outside using amorphous glass wool (Superwool 607HT, Thermal Ceramics LLC, Windsor, U.K.). The extraction plenums were also insulated and heated to prevent condensation in the extraction tubes. A picture of an extraction plenum with half of the outer shell removed is shown in figure 4.8 with the insulation and heating visible. The insulation is made of compressed glass wool boards (Superwool 607HT boards, Thermal ceramics LLC, Windsor, U.K.). The heating is electrical and done using coiled nickel-chromium wire (NIC80, Omega Engineering Inc., Stamford CT, USA) inserted in a Pyrex tube to prevent ignition of the combustible mixture that might form in the exhaust plenum.

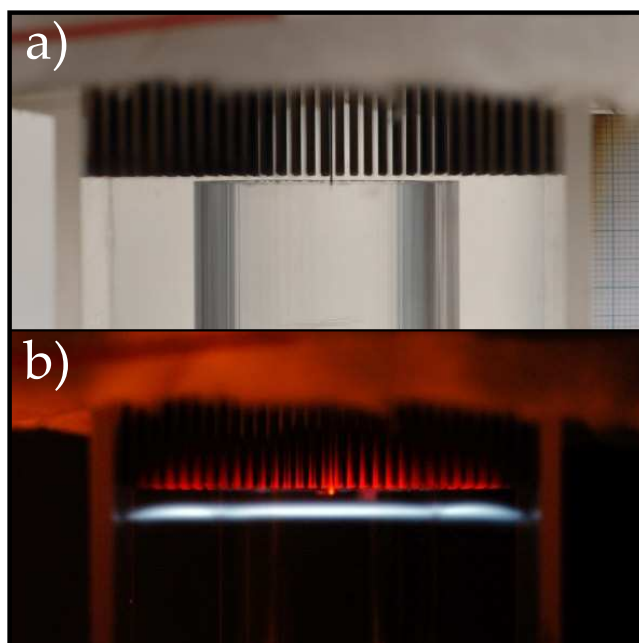


Figure 4.7: a) 45 mm O.D. quartz cylinder inserted in the burning chamber to isolate the uniform central portion from the edges where small gradients remain. b) Flame shape in the Mark II version of the burner with the quartz cylinder inserted.

These heating element were then formed into coils using a blowtorch to increase the power density. Four such heating elements are placed in each extraction plenum, connected in series for a total heating resistance of about 400 Ohms. The assembly is connected to an autotransformer, with the voltage varied to produce the desired heating power. Using thermocouples inserted at different locations in the exhaust plenums, the temperature is regulated manually at around 200°C to avoid the formation and accumulation of condensation. This heating system has the advantage that it also helps to keep the temperature of the injection array uniform. In the Mark I version of the burner, the formation of a hot core in the array resulted in important lateral gradients in the counter-diffusing species boundary condition, contributing to flame curvature.

Finally, to ensure a symmetrical repartition of the heat losses in the burning chamber and chimney, all of the attachment are symmetrical in this version. All components are held by the corners only, which also improves the optical access to the burning chamber. The ignition port (present in one of the chamber windows) used in the Mark I version caused significant heat loss, especially because of the rod used to close it. To avoid this problem, the flame is now lit with an electrical arc. A device as built which can produce electrical arcs up to 25 mm in length. Two small holes in the chimney allow the introduction of electrodes in the chamber. This technique proved safer and more reliable than the open flame ignition used in the Mark I version of the burner.

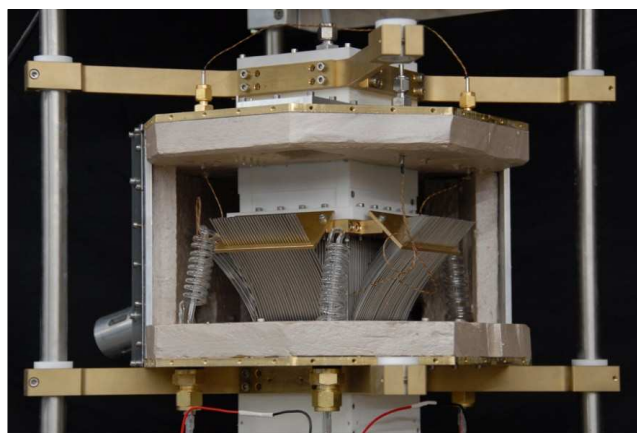


Figure 4.8: Picture of one of the extraction plenums in the Mark II burner, half of the outer shell removed, with insulation and electrical heating installed.

4.2 Image Acquisition

For all data relevant to flame position and shape were gathered using the visible light emission of the reaction zone. It is therefore an indirect measure of the chemical reaction rate but one that should be representative of the flame temperature. To measure flame position and the patterns formed by cellular instabilities, digital still photography was used. To capture the very dim dynamics of the intensity pulsations, high-sensitivity video cameras were used. Laser based techniques such as laser-induced fluorescence (LIF) could have allowed the reaction rate distribution to be measured more directly. But in the hydrogen flames that constitutes the bulk of the work presented here, the low concentration of radicals in the reaction zone mean that large integration time have to be used, providing little advantage over photography of the visible light emission. For this reason, this potentially helpful but surely time-consuming technique was not implemented in this thesis.

In this section will be briefly reviewed the experimental means and techniques that were used to produce the images presented in this thesis and the experimental data derived from them.

4.2.1 Photography

The instabilities at the heart of this work occur close to flame extinction when the burning intensity is weak and the light emission very dim. To capture the flame shape it was necessary to use sensitive cameras, wide aperture lenses (low $f/\#$) and long exposure time. Two viewing angles were used and are illustrated in figure 4.9. To measure the flame position or the location of probes (thermocouples, mass spectrometer capillary) in the chamber the images were taken from the side (position 1). To record the shape of cellular flames the burning chamber was imaged from below, with a viewing angle of about 30° (position 2) from the horizontal. Typical exposure time for cellular flames ranged from $1/2$ to about $1/10$ in the weakly luminous hydrogen flames studied and using the most sensitive equipment available. This explains the extensive efforts taken to reduce the strain-induced cell motion, allowing these long-exposure pictures to reveal

the true flame shape without streaks behind the cells.

Custom image treatment software was developed under Matlab to extract the flame standoff distance relative to the injection tubes from the images captures from the side. A reference picture was taken in ambient light with a scale reference inserted at the flame location. From this picture, reference points are chosen for the location of the injection array and scale factors. A semi-automated procedure then identifies the flame position from the location of the peak of light emission. Provided that the images used are not saturated, this method for determining flame position proved very repetitive and reliable.

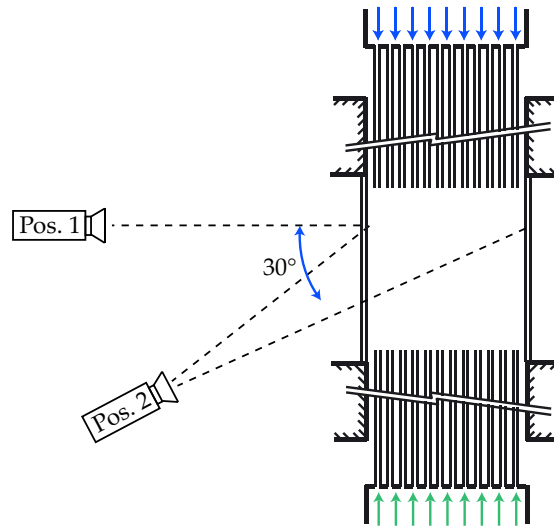


Figure 4.9: Viewing angles used to capture flame and probe locations relative to the top injection array (position #1) and the shape of the cellular pattern formed (position #2).

Two cameras were used, the first is a Nikon D200 digital SLR with which most of the images presented in this thesis were captured. The specifications include a 10 megapixels sensor ($3'872 \times 2'592$) with a maximum ASA/ISO rating of 1600. The Lenses used were either a 105 mm f/1.8 or a 50 mm f/1.4 for very low light conditions. For both lenses, extension rings were used to maximize the spatial resolution offered by the camera. Typical resolutions are on the order of 40 pixels/mm. The camera was usually piloted directly from the computer using the Nikon capture software that allow the control over all camera functions through a USB interface. This avoided the vibrations resulting from triggering the camera manually for long exposure shots.

The second camera used is a SONY Cybershot DSC-F828 digital still camera ($3'264 \times 2'448$ px, 8 megapixels) with fixed optics (28-200 mm zoom f2.0-1.8). The maximum ASA/ISO rating of the sensor is 800. Although manual control over all essential features is possible, it is through complicated menus since this model is intended as a straightforward point-and-shoot camera rather than a research tool. The limited light gathering capabilities and working distance (no macro photography possible) resulted in this camera being used only when two simultaneous viewing angles were necessary. For example to get the flame position (side view) and the cellular pattern (viewed from below).

4.2.2 Video

The other type of thermal-diffusive instabilities investigated in this thesis, planar intensity pulsation, proved harder to record than the cellular flames which have the advantage of remaining more or less steady, allowing long exposure time. For pulsation, temporal resolution is required more than spatial resolution and that, for the dim flames in which pulsations are observed, can be challenging. Intensified cameras are usually the obvious choice for this type of task, but none was available at the time with sufficient bandwidth.

In the field of high-speed imaging, very sensitive light sensors are sought because of the short exposure time available between the frames. The use of a high-speed camera at a low speed setting provides a remarkable light sensitivity. For this reason and because of availability, a very-high-speed digital video camera was used to capture the dynamics of the pulsating flames. The instrument used was a Photron FastCam APX (Photron Limited, Tokyo, Japan) capable of recording up to 120'000 frames per second (fps). In these experiments, the frame rate used was between 50 fps (the minimum) and 250 fps, with the exposure time being simply the inverse of the frame rate. The camera was positioned at the position 1 of figure 4.9 to gather as much light as possible. Another image treatment program was coded under Matlab to extract intensity variations from the produced movies and compute the frequencies present in the signal of the pulsating flames.

To observe pulsations in hydrogen flames, where very little light is emitted, the Photron video camera was not sensitive enough, even at 50 fps. However, the digital still cameras described in section 4.2.1 also had limited video recording capabilities. The Sony can reach 30 fps. Unfortunately, the poor light gathering capabilities and limited sensitivity of the Sony camera made it unusable to record pulsations in hydrogen. The Nikon camera is capable of taking up to 4 fps with full resolution and it is with this limited temporal resolution that these instabilities were documented.

4.3 Velocity measurements

In the idealized one-dimensional chambered flame model of figure 3.1, the velocity is simply assumed to be strictly parallel to the burner axis. Therefore, a set of very important measurements to validate and characterize our experimental realization are the velocity profiles. Only a limited number of experimental techniques are available to measure the very small gas velocities (10-100 mm/s) that are encountered in this experiment without inducing too much perturbations on the flow, two were used in this thesis. In the Mark I version of the burner, the velocity measurements were taken using the non-intrusive Laser Doppler Anemometry (LDA) technique. However, in the Mark II version, the flow cannot be seeded to enable the use of LDA since both reactants are inserted through needles array. When seeding is attempted, the seeding particulates stick to the walls of the needles and an insufficient amount reaches the burning chamber. For this reason, another more invasive technique based on heat transfer from a heated element inserted in the flow was implemented to gather at least some data on the flow field in the Mark II burner.

4.3.1 Laser Doppler Anemometry (LDA)

Velocity measurements techniques that are based on optical techniques such as LDA provides the advantage that all measurement instruments can be located outside the flow being measured. The perturbation of the flow is therefore minimal and limited to the seeding particulates inserted in the fluid and used as tracers. The technique of LDA works by intersecting two beams of collimated, monochromatic and coherent laser at a point in the flow where the velocity should be measured. When they interfere, the beams produces a set of straight fringes. It is these fringes that the tracer particles reflect toward a detector where velocity of the fluid can be deduced from the frequency of the backscatter signal, provided that proper calibration is carried out.

The experimental setup used for this purpose includes a Ar-Ion laser (Coherent Innova 90) that produces the three laser lines used to measure velocity along three axis in the flow. The laser beams are aimed at the burner by a optical head located on a three-axis computer-controlled motorized traverse system. The backscatter signal is processed by a burst spectrum analyzer (Dantec BSA model S, 57N10 and 57N25). A detailed description of the setup used is provided in reference [56].

The flow is seeded with alumina dust, nominal diameter $0.3 \mu\text{m}$ (Micropolish IIA, Buehler, Lake Bluff, IL, USA). To achieve satisfactory particle suspension in the very low flow rates used in this experiment, a new seeder had to be constructed. The fluidized-bed seeder used is based on a design by Willmert and Jarius [97]. The gas to seed is inserted from the bottom of a cylinder partly filled with particulates through a porous metal plate to ensure even distribution. To avoid the formation of channels in the dust, part of the gas is also inserted through a hollow stirring device inserted in the mass of dust and rotated by an electrical motor. This design proved very effective and allowed hours of uninterrupted operations before the device had to be refilled with dust.

4.3.2 Hot thermistor anemometry

The Mark II version of the burner preventing the seeding of the flow, another technique was implemented to gather some insight about the nature of the flow in this new burner. The technique used is a derivative of hot wire anemometry, based on the heat transfer between a heated element and the flow. As the name implies, in this technique an extremely thin electrically heated wire, usually platinum, is inserted in the flow to measure. The velocity is deduced from the fact that the resistance of the wire changes with temperature. If a certain amount of electrical energy is dissipated in the wire, its temperature will depend on the amount of energy that can be carried away by the flow, which is a function of its velocity. With proper calibration of the wire resistance dependence on temperature it is possible to get accurate results, provided that the probes are constructed to minimize the perturbations they induce in the flow field.

However, hot wires cannot measure the very small flow velocities prevailing in the burning chamber, down to 10 mm/s. To do so, another resistive element with a resistance that depends more strongly on temperature can be used, the thermistor. This passive electronic component is designed specifically as a solid-state temperature sensor, its name being a portmanteau for thermal and resistor. Examples of such systems can be found in the literature [98, 99] that can measure gas velocities as low as a few centimeter per second. Although commercial system based on this technique exists, they are not aimed at research applications and must be modified to enable the extraction of a usable signal. One such device that was tested with limited success is the

Testo 405 (Testo A.G., Germany), which is made for the ventilation industry.

The actual device used was developed at EPFL for measurement of thermally-induced air flows in models of various landscapes [100]. The system works by supplying a constant current to the thermistor (constant current anemometry CCA) and recording the variation of the element resistance as a function of the flow velocity. A sample of a typical response curve of the output signal, measured in millivolts, as a function of the flow velocity is given in figure 4.10. From this calibration curve it is possible to obtain the velocity profile across the burning chamber.

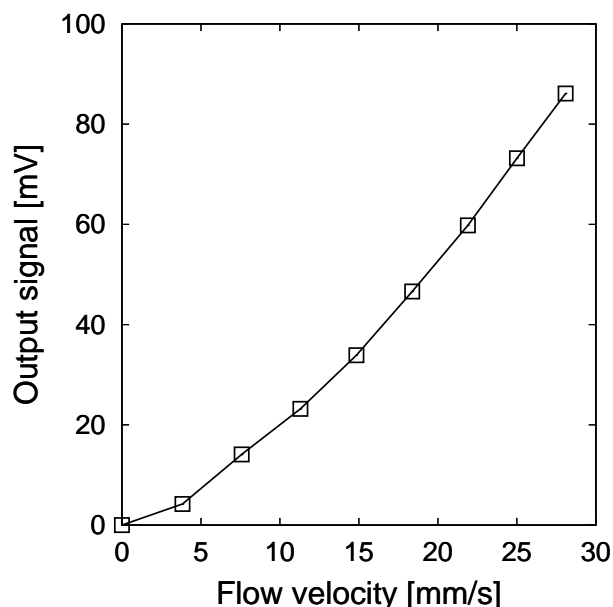


Figure 4.10: Sample of calibration curves typically obtained from the hot thermistor anemometer.

The probes were too big to be inserted in the burning chamber through one of the extraction tubes. The burner was therefore opened and the probes leads inserted from the inside through one of the extraction tubes before being connected to the rest of the instrument. After each change in position the system was calibrated since changes were observed in the zero flow response following the unmount and re-mounting of the probes. Probably because the advanced age of the electronics used (exceeded a quarter-century), the repeatability of the measurements was limited and their accuracy is not expected to be better than 10%.

4.4 Temperature measurements

The flame temperature is an important parameter to assess the quality of the flame realized experimentally and compare it with the theoretical configuration where models are developed. The measurement of temperature in flames is a challenging task, the extremely high temperatures, high radicals concentrations and probe induced pertur-

bations are all complicating factors that must be overcome. Two mainstream methods are available to obtain the temperature of a flame. The first is based on optical techniques while the second, which is used in the current work, uses specially designed thermocouple probes.

Optical techniques are used extensively in combustion research to obtain both temperature and species concentration measurements. They rely either on linear (Laser-induced fluorescence (LIF), absorption, spontaneous Raman scattering (SRS)) or non-linear (coherent anti-Stokes Raman spectroscopy (CARS), degenerate four wave mixing (DFWM)) processes. Using these methods, it is possible to determine the rotational distribution of some ion (frequently OH^-) from which the temperature of the gas can be determined. The errors resulting from the fits of the experimental spectra can be as low as ± 17 K [101] or 5% [102], depending on the technique used. However, this approach is complicated, expensive, time-consuming and requires quality optical access to the flame. For a complete treatment of laser diagnostics techniques in combustion, see the book of Eckbreth [103].

The use of thermocouples is considerably less material intensive but the direct probing of the flame implies complications that must be accounted for. Nevertheless, the simplicity of thermocouples based temperature measurements has motivated many researchers to devise ways to overcome these complications. Comparisons with optical techniques confirm that good precision can be achieved with thermocouple flame temperature measurements, on the order of ± 50 K [104] or better. To achieve such results, proper care must be used in the fabrication of the probes and the interpretation of the output signal.

4.4.1 Temperature measurements with thermocouples

When a conductor is placed in a temperature gradient it will generate a potential difference, this is called the thermoelectric effect or Seebeck effect. Since the magnitude of the effect is a function of the conductor used, two different conductors connected together at one end and exposed to the same temperature gradient will each produce a voltage of different magnitude and opposed sign. The resulting net potential difference across this thermocouple will then be a function of the temperature of the junction only. The topic of temperature measurement from thermocouples is mature and extensive literature is available regarding the subjects of probe design, calibration and compensation which will not be treated here [105, 106]. In the measurements presented here, the signal from the thermocouple probes is read and compensated by commercially available thermocouple readers. The instruments available consisted of a 16 channel desktop unit (model SR636, Stanford Research Systems, Sunnyvale, CA, USA) and a two channel handheld reader (model HH502, Omega Engineering, Stamford, CT, USA).

4.4.2 Probes fabrication

When performing measurements in combustion systems, the temperature as determined from the voltage between the two thermocouple leads is the result of a balance between the different processes supplying and removing heat from the junction. These include conduction and radiation losses, catalytic heating through surface reactions on the probe material and convective heat transfer with the gas environment. A graphical representation of the situation is presented in figure 4.11. In order to be able to calculate the gas temperature with reasonable accuracy from the junction temperature,

probe design generally aims to eliminate conduction and catalytic effects. The heat exchange problem then reduces to equating the radiations losses of the probe to the heat transferred from the surrounding gas by convection. The techniques implemented in this thesis and presented here constitute the state of the art in thermocouple based flame temperature measurements.

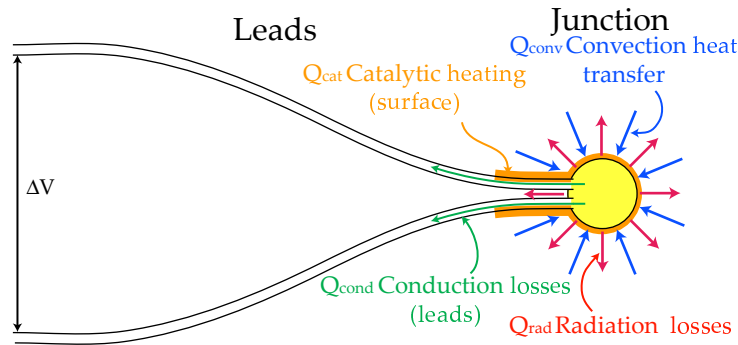


Figure 4.11: Schematic of a thermocouple illustrating the contributions in the heat transfer problem.

Several thermocouple metal pairs suitable for flame temperature measurements are available commercially. All the thermocouples used in this thesis were of R-type (platinum - platinum/13% rhodium) or B-type (platinum/30% rhodium- platinum/6% rhodium), because of their high temperature stability and widespread availability in various wire diameters. Such thermocouples can measure continuous temperatures up to 1600°C and 1700°C respectively. Other metal pairs are available with characteristics suitable for specific applications, the interested reader is referred to the literature [107]. The junction between the two leads can be soldered, welded or simply twisted, as long as good electrical contact is provided. However, the size of the junction determines the spatial resolution of the measurement and must be able to sustain the high temperatures of the flame front. For these reasons, all the thermocouples used had a welded junction.

The thermocouples were acquired from Omega Engineering Inc. (Stamford, CT, USA). The R-type thermocouples are of the P13R model while the B-type are P30R model and were all bought pre-welded with a spherical bead junction. The dimensions of the leads and junctions of the different thermocouples used are provided in table 4.1. This table also includes the K-type general use thermocouples (chromel-alumel™) used to monitor the low-temperature regions of the burner, to detect the risk of condensation. These thermocouples have a maximum measurable temperature of 1250°C.

In the instances where the thermocouple junctions had to be welded, either for repair or to create new probe geometry, electric arc welding was used. In this technique, an electric arc generated by discharging a capacitor bank is used to melt some lead material and form the junction. The arc can also simply be produced by short-circuiting a DC power supply. The operation is delicate and must be realized under a microscope and using micro manipulators. The use of a carbon electrode helps to produce spherical bead junction while an axial (or butt weld) junction without bead can be produced by placing the wires end-to-end with only a small gap. This welding technique can be used on wire as small as 30 μm [107].

Probe #	Type	Junction type	Wire diameter [mm]	Junction Diameter [mm]
0	R-adjacent	Bead	0.125	0.195
1	B-opposed	Bead	0.203	0.386
2	B-opposed	Bead	0.203	0.365
3	B-opposed	Butt welded	0.203	0.230
4	B-opposed	Butt welded	0.203	0.280
5	R-adjacent	Bead	0.125	0.192

Table 4.1: Characteristics of the thermocouples used, before coating. The opposed type probes are the Y-shaped design of figure 4.12(a) used to minimize conduction losses.

Conduction losses

The classical approach to minimize conduction losses starts by using lead wires as small as possible. The platinum wires used for R and B type thermocouples are found easily in diameter as low as 0.001" and 0.0005" (25.4 μm and 12.7 μm) but these are so fragile that a strong breath will break them[107]. The thermocouples used here had nominal diameters of 0.003, 0.005 and 0.008 inch (76, 127 and 203 μm), as can be seen in table 4.1.

To further minimize the heat transfer out of the junction by conduction in the leads, the wires are often arranged axially (opposed) out of the junction and aligned perpendicular to the temperature gradient. This is of course only possible in flat flames and ensures that the wire immediately next to the junction does not experience a temperature gradient and therefore does not transfer heat. Some of the probes used in this thesis were constructed in a Y configuration to use this technique and an example is shown in figure 4.12a).

These probes have the disadvantage of being relatively bulky and are impossible to insert in our burner design through the extraction tubes. To position them in the burning chamber, the burner had to be opened, the chamber windows removed and the sheathed probe leads inserted unconnected in two separate extraction tubes from the inside. Once the leads ends reached the outside of the burner, they were connected to the measuring instrument and moved to control the junction location in the chamber. Simpler probes with adjacent wires were also constructed, with limited attempts made to minimize conduction losses, such as the one presented in figure 4.12(b). These could be inserted directly in the 1.2 mm inner diameter extraction tubes from the outside without the need to open the burning chamber. To build these probes, the finest thermocouple wires (76 μm diameter) were first coated with a thin layer of liquid ceramic adhesive (Cerambond 835M, Aremco, Valley Cottage, NY, USA) and then inserted in a stainless steel capillary (Unimed SA, Lausanne) of 0.5 mm outer diameter. At the probe tip, the leads are insulated with a double bore ceramic tube of 0.8 mm outer diameter (Omega Engineering) and glued to the metal capillaries with the ceramic adhesive.

Catalytic heating

The conditions prevailing at the flame front can be hard on the thermocouple probe material, with very high temperatures and significant free radicals concentrations. The noble metal pairs chosen above for the thermocouple materials ensure reasonable probe

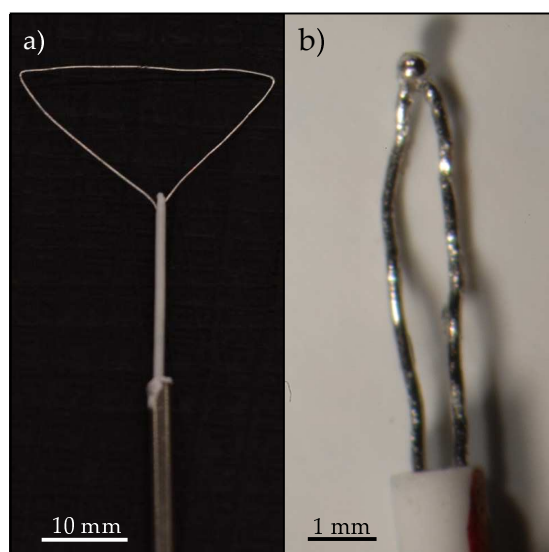


Figure 4.12: (a) Y-shaped (opposed leads) thermocouple probe, used to minimize conduction losses. (b) Compact probe with adjacent leads from the thermocouple junction to allow insertion through the extraction tubes.

lifetime and performance but their catalytic properties induces another significant source of error. All metal surfaces exhibit catalysis activity for atoms and radicals recombination reactions, liberating heat [107]. This activity is particularly strong for platinum alloys, as demonstrated by its widespread use in catalytic converters.

The magnitude of the catalytic heating effect varies significantly depending on the type of flame. In rich premixed flames, the radical concentration is low and the temperature increase can be as low as 60 K [108]. For premixed stoichiometric and lean flames however, the effect is much more pronounced and can reach 350 K [108]. In diffusion flames, the effect is relatively small and introduces errors on the order of one or two hundreds degrees Kelvin [109, 104] between thermocouple and optical measurements. It is customary to coat the exposed thermocouple wires and junction with a non-catalytic material to eliminate this effect. Results from both coated and uncoated thermocouples will be presented in section 6.3, allowing the evaluation of the amplitude of this effect in the present burner.

The first successful coatings developed for noble metal thermocouples is attributed to Kaskan[110]. It consist of a thin film of quartz silica deposited by immersing the thermocouple in a flame where a small amount of silicone oil is burner along with the fuel, usually methane. The oil use is typically hexamethyldisiloxane. When the strict procedure is followed, the coating is only a few microns thick (2 to 4 μm [111]) and successfully shields the probe from radicals. However this coating has been reported as delicate [112]. Additionally, the presence of silica in the coating can be detrimental [113] since silica is reduced by hydrogen at high temperature. The resulting free silicon can diffuses in the thermocouple material, causing embrittlement and calibration change.

Another approach has been developed by Kent [113] to deposit a coating of rare earth oxides (yttrium and beryllium). The procedure is once again tedious but good

results have been reported [113, 114]. This coating also has its lot of problems, while satisfactory at atmospheric pressures, the temperature drifts in low pressure flames [114]. More problematic is the fact that the compound is not stable over long periods and that the beryllium oxide BeO is highly toxic, causing lung problems and cancer among other conditions [115].

Recent work on thermocouple based flame temperature measurements have advocated the use of alumina-based ceramic adhesives as coatings [112, 116]. The procedure is very simple and was be the only used in this thesis. These products are available commercially and the probes simply coated by dipping. By using alumina based adhesives and adjusting the viscosity with an appropriate thinner, a suitable coating can be achieved. The thickness of coating deposited on the probes is significantly greater than with the two previous methods, usually a few hundreds microns. With proper characterization this does not constitute a problem other than loss of spatial resolution. The adhesives used for coating in this work are from Aremco Corporation (Valley Cottage, NY, USA), products number 503, 671 and 835M. All of these are delivered in single component liquids with different viscosities and rated for continuous use up to 1650°C. Pictures and dimensions of coated thermocouples are provided in figure 4.13 and table 4.2.

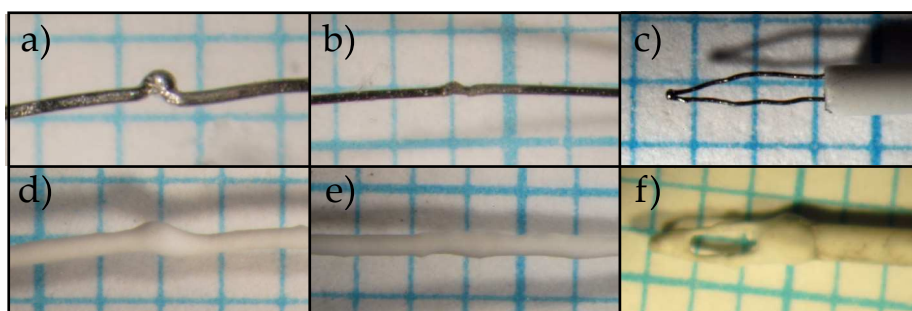


Figure 4.13: First row: (a) uncoated thermocouples probes with opposed leads with bead junction and (b) butt-welded junction. (c) Thermocouple probe with adjacent leads. Second row is the same probes as the first row but coated with ceramic adhesive to prevent catalytic effects. The background grid has 1 mm spacing.

Probe #	Type	Junction type	Wire diameter [mm]	Junction Diameter [mm]
0	R-adjacent	Bead	0.793	0.530
1	B-opposed	Bead	0.362	0.605
2	B-opposed	Bead	0.375	0.520
3	B-opposed	Butt welded	0.394	0.526
4	B-opposed	Butt welded	0.322	0.424
5	R-adjacent	Bead	0.206	0.570

Table 4.2: Characteristics of the thermocouples used, after coating with alumina based adhesive.

Radiation losses

The thermocouple, the burning gas mixture and the chamber walls being at different temperatures, they will exchange energy through electromagnetic radiation. The transfer will generally be away from the thermocouple and will result in a junction temperature lower than the temperature of the surrounding gas. This effect can be significant, inducing errors up to 500 K [116] and must be quantified for thermocouple measurements to be meaningful. Through comparison with optical measurements or numerical models the accuracy of thermocouple measurements of flame temperatures has been estimated to be within 10 – 20 K [107] when proper probe fabrication and radiation correction are used.

The level of sophistication in the radiation correction can vary greatly and will determine the precision of the thermocouple measurement. The probe surface will exchange heat with every surface it has a line of sight with and ideally, all of these surfaces should be taken into account. Such an approach was taken by Kim et al. with a probe surrounded by 3 surfaces. They solved the four-body problem following the methodology of the circuit equivalent analysis of Holman [117]. However in the burner used here, all of these surfaces are likely to have different temperatures distributions, emissivities and specular properties¹. The problem is further complicated by the presence of hot gas in the enclosure, with H₂O and CO₂ absorbing and radiating infrared radiation significantly [117]. This explains the red glow observed above the thermocouple (on the water rich side) when inserted in the flame zone.

To simplify the problem, two assumptions can be made alternatively at the expense of some accuracy in the radiation correction. First, the probe can be assumed to only emit radiation, neglecting the radiation it receives from its surroundings. This assumption is valid for a small radiating body in a large enclosure and will result in an overestimation of the radiation correction and of the measured temperature. The alternative, which is used here, consists of assuming that the whole enclosure is large and behaves as a gray body with a single temperature. The resulting net heat flux between the radiating body (the probe) and its surrounding is given by equation 4.1, where q is the net heat flux, A_1 the surface of the hotter body, ϵ_1 its emissivity, $\sigma = 5.669 \times 10^{-8} \text{ W/m}^2 \cdot \text{T}^4$ the Stefan-Boltzmann constant and T_1, T_2 the temperatures of the hotter body and its colder enclosure, respectively. For results presented in section 6.3, the temperature used was the measured temperature of the surface with the largest shape factor with the probe².

$$q_r = A_1 \epsilon_1 \sigma (T_1^4 - T_2^4) \quad (4.1)$$

Convective heat transfer

When the junction is inserted in the hot gas stream, heat will be supplied to it at a rate limited by the properties of the flow. This rate must be known in order to balance the other exchange processes listed above. The fluid mechanics of such problems is complicated and therefore it is customary to use empirical correlations for the heat transfer dependence on the flow conditions. The relevant dimensionless numbers in this situation are the Reynolds number, the Nusselt number and the Prandtl number,

¹The radiation reflected by the quartz windows has both a significant specular and diffusive character. Additionally, the transmission and absorption of the material cannot be neglected.

²The shape factor between two surfaces is the fraction of the energy that leaves the first and reaches the second [117].

which are given in equation 4.3. The Reynolds number is the ratio of the inertial and viscous forces, illustrating the strength of the convection. The Nusselt number relates the magnitudes of the convective to the conductive heat transfer and the Prandtl number is the ratio of the viscous to the thermal diffusion rates. In these expression U is the bulk velocity, D is the probe diameter, ν is the kinematic viscosity, D_{th} is the thermal diffusivity, h the convective heat transfer coefficient and λ the coefficient of thermal conductivity. The net convective heat flux q_c between the flow and the probe can then be found using the convective heat transfer coefficient, as shown in equation 4.3, with T_∞ the unknown temperature of the gas measured.

$$\begin{aligned} Re_D &= \frac{UD}{\nu} \\ Nu &= \frac{hD}{\lambda} \\ Pr &= \frac{\nu}{D_{th}} \end{aligned} \quad (4.2)$$

$$q_c = h \cdot A_1 (T_\infty - T_1) \quad (4.3)$$

Empirical correlations are numerous for the low Reynolds numbers flow prevalent around the probe with the one developed by Kaskan [110], following work by McAdams [118] being used frequently. The correlation used here was developed by Holman [117] and is given in equation 4.4. It is valid in the Reynolds number range encountered in this work ($0.4 \geq Re \geq 4$) and accounts for the influence of the Prandtl number.

$$Nu = 0.989 \cdot (Re)^{0.330} \cdot Pr^{1/3} \quad (4.4)$$

4.4.3 Effective temperature

The probe fabrication technique used here minimized the conduction losses from the probe and the catalytic effects on its surface. Accordingly, both of these phenomena were neglected. The determination of the effective gas temperature from the measured temperature of the thermocouple junction then simplifies to balancing the radiation losses with the convective heat transfer to the probe. When equating the net heat fluxes by radiation and convection (equations 4.1 and 4.3) it is possible to solve for T_∞ , the unknown temperature of the gas surrounding the probe.

$$\frac{\lambda Nu}{D} (T_\infty - T_1) = \epsilon \sigma (T_1^4 - T_2^4) \quad (4.5)$$

The parameters that need to be determined experimentally or from the literature are the temperature representative of the surroundings T_2 , the probe diameter D and the emissivity of the thermocouple coating ϵ . The first two can easily be measured. The temperature representative of the surroundings has to be averaged from the values of the different chamber walls but plays only a small role in the equations because of its relatively small variation. The more important probe diameter was determined precisely from optical microscope measurements (see tables 4.1 and 4.2).

The most critical parameter determining the accuracy of the radiation correction procedure is the emissivity of the thermocouple surface. This value can vary considerably with temperature and it obviously has a huge effect on the radiated heat flux.

Both experimental results and theoretical predictions are available in the literature for the emissivities of various materials with reasonable agreement between the two. For the uncoated thermocouples, the emissivity of pure platinum was used since for the platinum-rhodium alloys used here the difference in emissivity is small [119]. Since the effect of radiation is most important at high temperature and to minimize the error in determining the flame temperature, the emissivity used was chosen for a relatively high temperature of 1500 K. For this temperature representative of the region close to the flame front, the emissivity of platinum found in the literature was 0.29 [120, 121].

It was considerably harder to find reliable data for the emissivity of the ceramic adhesives used to coat the thermocouples. Other researches have assumed a value of $\epsilon = 0.8$ [112], corresponding to the emissivity of alumina (Al_2O_3 , the major constituent of the Cerambond adhesive used) at ambient temperatures. However, the emissivity of alumina decreases significantly even for moderate temperature increases [122], resulting in overestimation of the radiation correction [112]. Data for high temperature emissivity of alumina was found in the review paper of Whitson [123] and the value used of $\epsilon = 0.38$ corresponds to a temperature of 1500 K. This last reference also contains data consistent with the value of $\epsilon = 0.16 - 0.20$ used by Kim et al. [116] for magnesia-based ceramic coatings.

The gas transport properties are also highly temperature dependent, especially the viscosity used to compute the Reynolds number in equation 4.4. This dependence is taken into account either through an iterative procedure based on the numerical tools described in section 3.3 or by using Sutherland's formula for the temperature dependence of gases. This procedure was implemented to obtain the results presented in section 6.3 of the burner characterization chapter.

4.5 Gas mixtures preparation

Before being supplied to the burner, the fuel and oxidant are mixed with an inert gas to achieve the necessary mixture strength and Lewis numbers to observe instabilities. When a set of reactants is diluted in a given inert gas the range of Lewis numbers resulting from different dilution levels is very limited. For example, between a mixture of 80% O_2 in CO_2 and a mixture of 20% O_2 in CO_2 the Lewis number changes only from 0.97 to 0.79. More importantly, changing the dilution level is not a convenient way to control the Lewis number since it also changes the mixture strength³. The use of different reactants or dilution gas allows other Lewis numbers to be investigated, but again only in a narrow range. Additionally, CO_2 is a convenient dilution gas, especially for hydrogen flames because it contributes significantly to light emission. It is therefore desirable to have at least some of it in the inert gas mixture used.

To enable the generation of a wider range of Lewis numbers the reactants were diluted in a mixture of two inert gases. CO_2 was always used as one of the dilution gases to ensure that hydrogen flames emitted enough light to be easily detectable. The gas mixtures supplied to the burner were prepared using a set of 6 mass flow controllers (model HFC 202 *Low Flow*, Teledyne-Hastings, Hampton, VA, USA), 3 for each of the fuel and oxidant streams. The precision of these units is 1% of the full scale and all of were used in the 0-10 standard liters per minute (SLMP) range. The mixture com-

³Ideally the mixture strength could be maintained while changing the dilution level. However, with the counter-diffusing species injection technique used here it is very difficult in practice because the boundary condition needs to be measured for each mixture composition used. Maintaining the mixture strength constant would require a lengthy iterative procedure to set the desired effective boundary condition.

position was controlled through a Labview application using data acquisition boards (PCI-6025E and PCI- 6713, National Instruments, Austin, TX, USA) to interface with the equipment. The calibration of the system for each gas used was made using a flow calibrator (DryCal DC-2, Bios International Corporation , Butler, NJ, USA). The gas mixtures are then fed to the burner through long lines to ensure homogeneous mixing.

Precise gas mixtures were also required to calibrate the mass spectrometer for all the species present in the various flames, enabling quantitative measurements of the mixture composition inside the burner. The critical importance of the accuracy of this task is discussed in section 4.1 and the mass spectrometry technique used is described in chapter 5. The instrument used required extensive calibration and because of a strong mixture dependence of the response, a very large amount of reference mixtures had to be measured. For all species except water the reference mixtures were simply generated using the setup described previously.

For water, it was necessary to develop a apparatus that could vaporize a precise amount of water and mix it with a stream of the other gases. The first approach consisted of simply injecting liquid water in a heated gas stream. This proved ineffective as water boiled in the supply tube resulting in a very irregular flow (slug flow). Moreover, the amount of water that could be vaporized was limited by the heat that could be stored in the gas before it reached the auto-ignition temperature of the hydrogen-oxygen mixtures that needed to be calibrated. The resulting maximum water concentration that could be achieved in this way was about 5% by volume. This would have required multiple vaporization stages to reach the 30% water vapor expected in the flame.

In the approach developed to reach this water content, the liquid is injected in a porous ceramic wick, made from machinable insulation (Sali-II, Zircar Ceramics, Florida, NY, USA). This wick is heated from the outside by a coiled heating element shielded by a Pyrex tube, as shown in figure 4.14b). This ensured constant water vapor production and allowed the system to generate mixtures with arbitrary water content. The other gases are heated before being inserted in the water vaporization chamber. The whole mixture is supplied to the mass spectrometer through another heated line, as shown in figure 4.14a). The liquid water is supplied to the unit using a medical syringe pusher (model B88801, Fisher Bioblock Scientific), which allow precise pumping in the ml/h range.

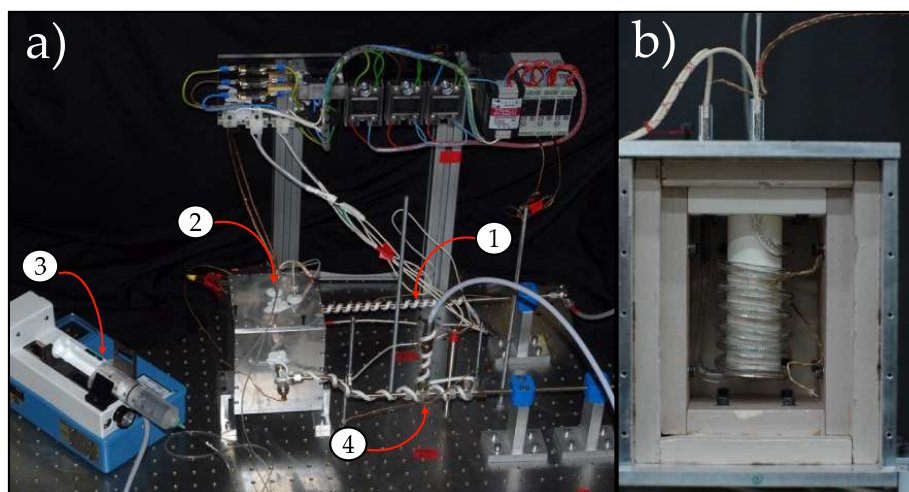


Figure 4.14: (a) Water vaporisation scheme used to produce calibration mixtures with high water content. (1) Input gases heating line, (2) Water vaporization unit, (3) Syringe pusher and (4) Mass spectrometer sampling point. (b) Close-up of the heated ceramic wick used to vaporize the water.

Chapter 5

Mixture composition measurements

The reactant supply method described in section 4.1.1 implies that effective the composition of the mixture injected in the burning chamber will not be know *a priori* from the gas streams prescribed at the flow controllers. The determination of the initial mixture strength requires the measurement *in situ* of the mixture composition at the burning chamber boundaries.

5.1 The choice of experimental technique

To measure the effective mixture composition it was first necessary to identify a suitable experimental technique. The field of analytical chemistry provides many instrumental means to obtain a quantitative measurement of the composition of a gas sample. The choice of a particular technique was guided by the following factors:

- **Low perturbation of the flame.** The sampling of the gas mixture must not significantly affect the gas flows to the flame, which are on the order of 5 – 10 SLPM.
- **Precision.** Should obviously be as good as possible, a few % error (2 – 5%) would be acceptable.
- **Repetition rate.** Since the whole burning chamber will have to be scanned multiple times, one data point should be collected in a few minutes at the most.
- **Cost**

The instruments commercially available from manufacturers intended for this task rely on various principles to extract information from the sample. Generally, the sample is subjected to a stimulus and then a transducer captures its response to be analyzed. For gas mixture composition measurements, most instruments rely on electromagnetic radiation (spectroscopy), electric and magnetic fields (mass spectrometry), separation (chromatography) or a combination of these techniques to probe the sample.

Fourier transform infrared spectroscopy (FTIR) was initially considered because of its wide availability and simplicity. The optical nature of the instrument allows for

stable performance over time and good linearity of the response over the wide concentration range to be investigated. However, due to the low absorption of gas samples the instrument requires long interaction length with the sample, on the order of 10 cm. This implies the use of large sample volumes, on the order of 200 ml for the most affordable models. The collection of such samples in the reaction area would either perturb the flame or prevent the use of a decent repetition rate. Moreover, presence of a large amount of water in the sample can prevent such instrument to function normally since water vapor has a broad absorbance range in the region of the spectrum used. Since the water produced by hydrogen combustion in the burner can exceed 30-40% by volume¹ at the flame, the option of using FTIR had to be rejected.

Gas chromatograph are often used for the type of low sampling rate gas analysis needed for this work. In this technique, the gas samples are inserted in a flow of an inert carrier gas and circulated through a long thin tube. The different species present in the sample will then be advected with the carrier gas at different rates depending on their weight. At the end of the tube a detector measures some property, such as thermal conductivity, of the flowing mixture to identify the different species. However the batch nature of this technique, limiting the achievable sampling rate, and the non-specific nature of the detection made this technique unsuitable for the needed real-time monitoring of the mixture composition.

In a mass spectrometer, the sample is first ionized and then the individual molecules composing it are separated (deflected) using an electric or magnetic field. The ability to measure very small ionic currents (picoAmperes) implies that a very small sampling rate is required to obtain a usable signal. It is mainly based on this argument that the choice of mass spectrometry was justified. A model using a sampling rate of 0.2 ml/min was selected (MKS Cirrus), ensuring that the probe could be placed very close to the flame or even inside it without inducing significant perturbations. A separation technique such as gas chromatography is often combined with mass spectrometry to form hybrid systems (GC-MS in this case), with the associated increase in the performance of the instrument mainly directed towards improved molecule identification. For the task at hand, which is the identification of the proportions of known species in a gas sample, a mass spectrometer alone was considered the most suitable option.

The burner configuration investigated here prevents the use of wide angle quartz probes that aerodynamically quench the reactions and allow the measurements of radicals through a molecular-beam mass-spectrometry system (MBMS). It is a widely used technique in combustion research for its ability to detect both stable and unstable species [124, 125, 126]. In our experiment, the samples being directly collected through a thin capillary, we expect the stable species concentrations to be reliable where the radical concentration is negligible, away from the thin reaction zone. In the reaction zone, the presence of atoms and free radicals can induce errors up to 10% [94] in the stable species concentration because of radical-radical recombination reaction occurring as the sample is transported towards the mass spectrometer. The introduction of the small sink that constitutes the capillary in a concentration gradient unavoidably induces perturbations. The reliability of the sample collected compared to the concentration at the probe tip has been investigated in the past [127], with the effect of suction of the capillary resulting in the collected sample being representative of a location slightly upstream of the probe tip. This offset has been measured to be up to 5 orifice diameters for some wide angle cone probes[128], but more typically 2 orifice

¹The water can even reach 60% by volume when the inert mixture used contains a large proportion of helium

diameters[129, 130]. For the straight capillary used in this experiment, we expect the perturbation to be of the same magnitude or smaller and the sampling system to deliver representative samples of stable species immediately in front of the probe tip, which has a 0.1 mm inner diameter.

5.2 Mass spectrometry based partial pressure analyzer

The instrument used for gas analysis is a compact quadrupole mass-spectrometer (QMS) based residual gas analyzer (RGA) or partial pressure analyzer (PPA). This type of instrument is used extensively for measuring the composition of gas samples in industrial settings. Their low cost, ease of use and wide application range has led to their widespread adoption in applications where qualitative data is sought, i.e. to assess the integrity of vacuum systems [131], detect the presence of contaminants in semiconductor manufacturing [132, 133] or monitor chemical processes for deviation from optimal operating parameters [134, 135].

The response of PPAs for a particular mass-to-charge ratio (m/z) is usually assumed to be a linear function of the partial pressure of the species with mass m in the sample, provided that there is no overlapping peaks. The validity of this assumption is limited by the precision expected from the measurements and must be investigated to ensure proper interpretation of the results. For the applications mentioned above, the concentration of the species of interest varies only in a narrow range in an otherwise constant mixture. Accordingly, the assumption of linearity is usually reasonable and can yield results accurate within a few percent [134] at best following proper calibration.

On the other hand, the use of PPAs to gather quantitative composition data for arbitrary mixtures of a given number of species is much more limited. While trivial to interpret for qualitative analysis, the instrument response necessitates extensive calibration to yield useful quantitative results. The interpretation of the data is complicated by the numerous factors that can compromise the instrument linearity when varying mixture composition over a wide concentration range. In this thesis, a custom calibration procedure is developed to account for the intrinsically non-linear behavior of the QMS response over a wide concentration range in a complex mixture of reactive gases, drastically improving measurement precision.

5.3 The instrument working principles

The working principles of mass spectrometry are considerably more complicated than for techniques based on interaction of the sample with electromagnetic radiation (spectroscopy). A mass spectrometer is made from three basic units: a ion source, a mass analyzer and a detector. A schematic representation is presented in figure 5.1. In order to properly calibrate the instruments and interpret its results, it is essential to properly understand these basic units. The mass spectrometer used throughout the current investigation presented here is manufactured by MKS Instruments Inc.(Andover, Ma, USA) . The Cirrus mass spectrometer is a bench-top unit that can only be controlled remotely by a computer through an Ethernet connection. A picture of the instrument is presented in figure 5.2(a). The assembly is built around a Microvision plus IP Residual Gas Analyzer (RGA). A view of the opened instrument identifying various components is presented in figure 5.2(b).

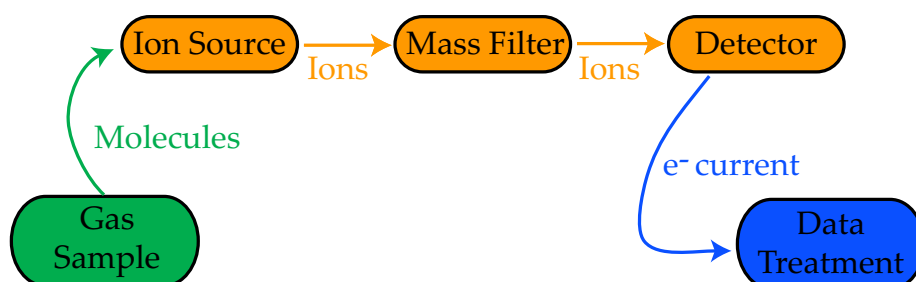


Figure 5.1: Outline of the different components involved in the mass spectrometer function.

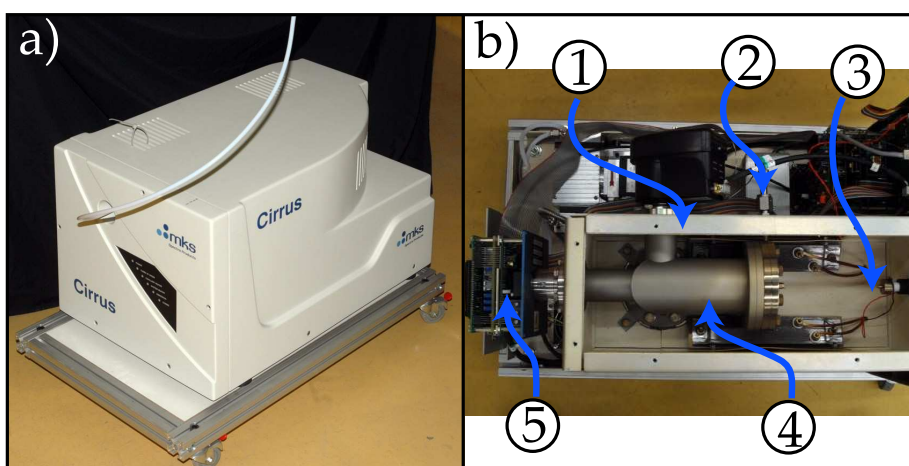


Figure 5.2: (a) Picture of the MKS Cirrus RGA used in this thesis. (b) View of the opened instrument with: (1) the oven enclosure; (2) Bypass line; (3) the capillary inlet; (4) high vacuum chamber housing the ion source and mass filter; (5) detector and associated electronics.

The sensitivity of the instrument is defined as the magnitude of the output signal per unit of the quantity measured. For PPA, this quantity is therefore expressed as the ionic current detected per unit of pressure of the species measured. Accordingly, the units used will either be Amperes per Pascals or Amperes per millibars. The instrument sensitivity is expected to be constant, producing a linear response as a function of the partial pressure, but in practice this is not the case. This is especially significant over the wide concentration ranges measured in this work. Various phenomena can induce non-linearities in each component of the instrument and in order to achieve a suitable calibration, these need to be understood. The calibration strategy will aim at establishing the instrument sensitivity separately for all species of interest and as a function of the factors that were found to be relevant (mixture composition, operating parameters). Because of limited access to the system internal states (operating pressures, ion currents) and for simplicity, the procedure described in section 5.4 calibrates the instrument as a whole without separating the different components. The possible origin

of these non-linearities of the mass-spectrometer will be discussed in the individual components described in the following sections.

5.3.1 Sampling

The sample is collected through a fused silica capillary, which can be heated to prevent condensation and the resulting flow perturbations. The sampling rate is a function of the diameter and length of the capillary used. For the results presented here, the capillary diameter was $100\ \mu\text{m}$ and its length was 230 cm. The resulting flow rate removed from the burning chamber was small enough to never induce observable perturbations on the flame. This issue is further discussed in appendix A. The capillary exits in a vacuum chamber housing the RGA that is purged by a turbomolecular pump backed by a dry diaphragm pump. The diaphragm pump also serves as a by-pass pump for the capillary aspiration and ensures a pressure sufficiently low at the entrance of the high vacuum vessel. The whole vacuum chamber is housed in an oven to help water vapor removal after startup (bake setting, 180°C) and pumping efficiency throughout normal operation (warm setting, 80°C). This arrangement is visible in figure 5.2(b) and a detailed schematic representation is provided in appendix A.

The sample collected is representative of the composition immediately in front of the sampling point. Particular attention was taken to properly characterize the flow regimes present in the different components of the system to avoid mass separation effects, or fractionation. A detailed analysis of the system used is presented in appendix A. Readers interested in sampling issues in PPA are directed to the exhaustive review paper of Blessing et al.[136]. The very small sampling rate (0.2 ml/min) results in the conditions throughout the capillary being laminar ($Re = 4.9$) and subsonic $Ma = 1.59 \times 10^{-3}$. From the estimated pressure distribution in the sampling system, the intermolecular forces are important and the flow can be considered viscous. Therefore, no mass separation effect is expected in the mixture. The conductance of such capillaries operating in the viscous regime, given by equation A.6 is the same for every species. Accordingly, the composition in the bypass chamber is identical to the composition at the sampling point since the flow is viscous in both the input capillary and the bypass line.

5.3.2 The ion source

In the MKS Cirrus, part of the sample is ionized in the ion source through electron impact ionization (EI). Electron ionization is a common technique in mass spectrometry, especially when dealing with gas samples with unknown organic molecules. Electrons are produced by heating a tungsten filament (thermionic emission) and then accelerated towards the sample by a static electric field. The sample molecule or atom M is ionized following relation 5.1.



The proportions of sample molecules that will be ionized will vary greatly depending on many parameters and will be a great source of variability in the calibration procedure. These include the specie nature (weight, diameter, etc.), its partial pressure, the total pressure, the electron energy, the presence of reactive species in the chamber, the state of the filament (age, surface adsorption of certain species, etc.) and many others to a lesser extent. For the particular model used here, the ion source comprises

two tungsten filaments located close to each other. The particular filament used will have an influence on the electrons trajectories and hence on the ionization efficiency. To ensure stable operation, ion source design has to account for physical phenomena that can affect electron production.

As they are used, the filament lose material to evaporation. This loss of surface area means that the filament has to be operated at a higher temperature to supply the same electron current. Although the emission current is regulated automatically and in real time to account for the variation in the filament performance, the ionization efficiency can vary significantly over the course of a measurement. In this paper, we are mainly interested in the effect of mixture composition on EI efficiency. It has been known for a long time that the presence of even a small amount of gas around a thermionic cathode induces strong species-specific emission changes[137]. Over the course of our experiments two time scales have been noticed in the variation of the instrument performance: upon mixture composition change, some changes occurred over the course of a few seconds or minutes, while others took hours to set it. Recent experimental evidence [138] demonstrate that the nature of the gas species present in the vacuum chamber can also affect the work function of the thermionic emitter through diffusion in the filament material. The nature of the atoms adsorbed on the emitter surface is also believed to play a role. These phenomena imply that even if the ionization current is monitored and regulated, the energy of the electrons and the focusing of the ions vary with the mixture composition. This variation in the ionization efficiency of the source necessitates proper calibration to allow the instrument to be operated over a wide mixture composition range.

It has been shown that space charge effects can account for the almost instantaneous change in instrument sensitivity when the mixture composition is changed. The space charge effects can change both the local potential in the ionization chamber and the efficiency of ions focusing towards the mass filter [139, 140, 141]. This effect depends strongly on the geometry of the ion source and is therefore instrument specific. It is however found to some extent in all commercial mass spectrometers [142]. Space charge effects can also become significant when the absolute pressure in the vacuum chamber is increased while the mixture composition remains constant. This effect is probably the most investigated mass spectrometer nonlinearity [143, 142, 140, 134]. For the experiments presented here, the very small and constant leak rate into the vacuum chamber ensured that the pressure remained more or less constant, see appendix A for details. The small measured pressure changes² observed while the mixture composition was changed are attributed to the ionizing nature of the total pressure gauge used (Penning gauge). Accordingly, the calibration presented here do not include the effect of high pressure on the instrument sensitivity.

The introduction of reactive gases in the vacuum chamber causes, in addition to the short timescale phenomena mentioned above, a slow drift in the instrument response. Oxidation and evaporation of material from the filament [144, 145] should normally be compensated by the electronics regulating the electron emission. On the other hand, the adsorption of molecule on the source surfaces can have reversible effects on the order of 10% with timescales of hours [142, 134] following even brief exposure to reactive gases. Over the course of weeks or months of operation, ion source and mass filter fouling can also induce significant variation in the instrument sensitivity through the deposition of insulating films on conductors or conducting films

²The Cirrus model allows the monitoring of the vacuum chamber pressure in real time while the experiments are conducted.

on insulators [143, 142, 146], modifying the source optics. These long timescales effects collectively known as source fouling will be addressed by the implementation of a calibration transfer strategy [147, 146], described in section 5.4.2.

5.3.3 The mass analyzer

To separate ions based on their mass-to-charge ratio, a quadrupole arrangement is used. The RF (radio frequency) oscillating electric field it produces deflects the ions differently depending on their mass-to-charge ratio (m/z). The quadrupole is designed in such a way that for a given frequency only ions with a single m/z ratio will reach the detector. The variation of this frequency across a certain range generates a signal reaching the detector that is representative of a succession of m/z ratios. The resulting scan is the mass spectrum of the species present in the sample. The mass filter used in the Cirrus is able to filter ions having a mass from 2 to 200 amu. The transmission efficiency of the quadrupole mass filter is known to be strongly mass dependent, up to a factor 5 [142]. This effect will be addressed by the calibration procedure implemented in section 5.4.2.

Some ambiguity may arise if two species present in the sample have the same m/z ratio, for instance carbon monoxide and molecular nitrogen (mass 28). The electron impact ionization can also result in the fragmentation of target molecules, producing new species that can overlap with species of interest. Cracking tables provided by the manufacturer or found in the literature can be used to determine the height of these secondary peaks from the main ones to resolve the ambiguity. In the results presented here the only instance where this was necessary was when measuring molecular oxygen and methane simultaneously. The fragmentation of O_2 upon ionization produces a secondary peak of mass 16 (11% of the height of the main peak), corresponding to atomic oxygen that must be subtracted from the methane peak to get its true value.

All of the ions whose m/z ratios are discarded by the mass filter end up their courses on the quadrupole rods where they recombine with electrons. When measuring certain species, especially large hydrocarbons, this can result in a surface fouling phenomenon similar to the one described in the previous section. Because of the nature of the species measured in this experiment, this effect is not expected to be important. In any case, the resulting long term sensitivity drift will be corrected by the calibration transfer strategy described in section 5.4.2.

5.3.4 The detectors

The sensitivity of the ion detector itself is also subject to variations over time. The Cirrus instrument used here is equipped with two types of detectors: A Faraday cup and a secondary electron multiplier (SEM). The Faraday cup detector is the most stable detector type, with the observed sensitivity changes for some instruments as low as 10% over months of use [134]. The more sensitive SEM detector is considerably less stable, especially when new, with order-of-magnitude variations observed over the first few weeks of use [142].

The SEM detector is significantly more sensitive than the Faraday cup, allowing detection levels in the low parts per millions (ppm) to hundreds of parts per billion (ppb) for the type of instrument used. However, the most sensitive detectors are usually the most non-linear [134]. Consequently, for all of the measurements presented here, only the Faraday cup detector was used because ppm detection levels were not

required. This simplified the calibration by removing the detector voltage as a parameter and was more than enough for the parts per thousand precision expected from these measurements.

5.3.5 Control software

To interface with the RGA, MKS supplies a software named *Process Eye*. This software is *recipe-based*, which means that the instrument is not controlled directly by the user but rather through a file (the recipe) containing a set of instructions. The language used is Visual Basic for applications (VBA) but the user is discouraged edit or even look at the code and directed to the *software wizard* for the creation of the recipes. This interface only allows the creation of very basic tasks for the instrument, such as measuring specific ranges of masses for a given time interval and performing basic data treatment. The *wizard* then writes the code for the recipe and that's it as far as the average user is concerned. When the instrument is started, the software reads the supplied recipe file and follows the instructions supplied therein. The wizard only allows the measured data to be provided graphically to the user or saved to a proprietary file format and is always in units of pressure. The user software does not provide means to access, let alone control, the instrument operating parameters such as the measured currents.

The implementation of the more complex tasks expected of this instrument in the research context in which it is used was a monumental task. For instance, the calibration of the instrument described in the next section calls for the relationship between the input (the partial pressure of a specific species) and the output (the measured current) to be established. The *wizard* was completely useless for this task since it does not even allow the knowledge of the measured current, it is supplied to the user already converted to a partial pressure, with the intermediate steps unspecified. All of the recipes used were therefore coded by hand and since the user is not expected to be able to write de code, documentation was very scarce.

The software reference supplied with the product contains only information on how to use the *wizard* which, needless to say, is a disappointment. The most useful documentation obtained from the manufacturer is a scriptable object reference. It lists the name of the software object used to control the instrument, its inputs and its outputs. Unfortunately, it only lists the names of the object, not their authorized values nor their description. A lot of trial and error was therefore involved in getting anything to work at all. A more exhaustive reference intended for applications developers using this software was later acquired: the software development kit (SDK) reference manual for the *Process Eye* software. It included a more detailed reference of some the scriptable objects but proved of limited use for the understanding of the instrument control, behavior and responses.

In the end, the use of software and the instrument in general was a horrible experience. The writing of recipe files was a tedious task and necessitated endless trial and errors to achieve the desired outcome. Over 15'000 lines of code were written throughout this project only to achieve the calibration of the instrument, a task that easily swallowed the equivalent of six months of full-time work. The technical support staff at MKS was usually very friendly and helpful to answer specific questions, once they were identified. However, most of the time their answers to more general questions were that they don't know because the instrument and software were simply never intended for such tasks. The software is only aimed at providing a clueless user the ability to monitor small changes from a reference state in a mixture containing only

trace amounts of one specie of interest. Everything else is uncharted territories and had to be characterized for this specific instrument. I will end my rant now, I just wanted to point out that I hate this machine and especially its control software.

5.4 Mass spectrometer calibration

The issue faced when wanting to use a atmospheric pressure RGA such as the MKS Cirrus to perform quantitative mixture composition is one of purpose. The instrument is intended to measure small variation in species themselves present in a small quantity diluted in a more or less constant gas matrix (hence the name *residual*). In these conditions, it is reasonable to expect the instrument response to be a linear function of the amount of the species of interest present. To calibrate the instrument, one mixture close what is typically encountered in practice and containing all the species of interest should be sufficient. In the current work, the mixtures encountered have a wide concentration range, i.e. the composition of the gas matrix is the subject of interest. As a result, significant non-linearities arise in different parts of the instrument (ion source, mass filter, detector) and need to be calibrated extensively. In the following sections will be discussed first the calibration procedures supplied by the instrument manufacturer and then the one implemented to account for the observed non-linearities.

5.4.1 Built-in procedure

The calibration procedure built-in the MKS mass spectrometer proved very disappointing, to the point that the results initially gathered were unusable for their intended purpose. As it is delivered, the only available calibration procedure implemented involves determining the instrument sensitivity by measuring a single reference sample. The user has to supply the molecular mass of one of the species present in the sample and its partial pressure. The software then simply divides the measured signal by the supplied partial pressure to obtain a calibration factor, in amperes per unit of pressure (the millibar or the Pascal were used here). This calibration factor is the instrument sensitivity for the specific species used in the calibration under the conditions prevalent at the time. This *single* calibration factor was then used by the software to calculate the partial pressure of *every* species under *every* conditions. As it is delivered, the instrument is therefore assumed to have a constant sensitivity as a function of the analyzed mass and a linear response over its dynamic range.

Tillford [134] noted in his paper on the limiting factors in the use of RGA for process monitoring, that users and some manufacturers assume that the same relative sensitivities used in ionization gages can be used for RGAs. However, this shortcut fails to account for the mass dependence of the different constituents of the RGA system listed in sections 5.3.1 to 5.3.4. For instance, in this same paper, the mass filter transmission dependence on the mass of the ions measured changes the RGA sensitivities by a factor 5 to ten compared to the ionization gages relative sensitivities. The shortcomings of these simplistic assumptions soon proved significant when measuring the mixtures encountered in this experiment.

When analyzing initial measurements made using the instrument calibrated following the built-in procedure, outrageous errors were noticed if the measured mixture deviated from the one used for the calibration. Moreover, the sensitivities for different species measured in pure samples is drastically different, with one order of magnitude between the sensitivity of hydrogen and that of CO₂. Further investigations revealed a

strong variation of the instrument sensitivity as a function of the mixture content being analyzed. For instance, the sensitivity of the instrument to hydrogen doubles between a mixture containing only trace amounts of the gas in an argon matrix and an even mixture of the two gases. When concentration profiles are taken along the burner longitudinal axis, the fuel concentration varies from typically 15 – 30% to trace amounts and errors in excess of 100% can result from the use of a constant calibration factor. The effect was a little less pronounced for oxygen, and as low as about 20% for CO₂. Nevertheless the cumulative effect on the measurement of the mixture strength, which is the main task that the instrument is intended for, is nothing short of catastrophic.

From that point, it was clear that this specific mass spectrometer would be useless in this experiment without the implementation of an extensive calibration procedure. This will make the instrument more versatile, allowing to go beyond the assumption of linear response. Although simplistic, this assumption is nevertheless valid for the actual purpose this instrument is designed for. That is the on-line monitoring and analysis of gas mixtures including trace contaminants in process gases.

5.4.2 Calibration over a wide concentration range

The objective of the calibration procedure implemented here is to capture the instrument response for each species of interest as a function of the operating parameters and the mixture composition in which the measurements are conducted. This is done through the measurement of numerous reference mixture of different compositions, referred to as the *training set*. The result is multidimensional mapping of the instrument sensitivity, with the number of dimensions equal to the number of gases in the mixture minus one³. One of these maps has to be generated for each species of interest and each set of operating parameters of the instrument. The parameters that should be considered include the ionization current, the extraction potential, the filter voltage and the detector gain. For the sake of simplicity, after the optimal operating conditions had been found, all of the instruments settings were kept constant.

Since the extent and nature of the non-linearities in the response of QMSs is poorly documented and instrument specific, it was difficult to defined an optimized training set beforehand. Therefore, the initial treatment of the problem involved a large amount of different mixtures spread over the entire concentration space of interest. Efforts to reduce the training set to a minimum required by the nature of the instrument response can then be made for further calibrations. An experimental set-up had to be constructed that could provide a wide range of reference mixtures of the species of interest, which is presented in section 4.5. For the CO₂-diluted H₂-O₂ flames studied, the concentration space of interest is 0-100% for CO₂, 0-75% for O₂ and 0-50% for H₂, H₂O.

Calibration transfer

The term calibration transfer applies to methods aiming to establishing the current behavior of an instrument through a limited number of measurements, referred to as the *transfer set*, by transferring the knowledge of the instrument behavior gained using an extensive training set [148, 147, 146]. For the procedure implemented here, correction factors are determined for each species of interest by comparing the measured sensitivities from similar mixtures in the transfer and initial training set. It is assumed

³One dimension can be removed because we assumed that all gases present in the sample are measured. This allows the total of all the measured mole fractions to be set to 1 and an arbitrary species concentration to be considered a dependent variable.

that these effects while affecting each m/z ratios differently, hence the species specific correction factors, do not affect the interactions between the species. The sensitivity maps themselves are therefore retained from the initial training set and the correction simply applied as an offset. This account for the variations in instrument sensitivity that occurred since the initial calibration. Experimental results on two and three gas mixtures confirm that this assumption is reasonable because although the height of response surface changes over the course of weeks, its shape remains unchanged. This temporal drift in the instrument response is present in all QMS instruments and becomes significant over the course of days to weeks, depending on the nature of the mixtures measured.

In the present experiment, the transfer set was simply the species of interest either pure (for CO_2) or at the upper bound of their calibrated range (75% for O_2 , 50% for H_2 and H_2O) diluted in CO_2 . This allowed the calibration of the instrument to be refreshed daily from the measurement of only four simple mixtures.

Binary mixtures

The response of the instrument was first measured when exposed to various binary mixtures of the species of interest diluted in a inert gas. Argon was chosen since it is very stable and extensive literature for the mass spectrometric measurement is available on this species. The variation of the instrument sensitivity, in Amperes per Pascals⁴ is presented in figure 5.3 for the first three species of interest (H_2 , O_2 and CO_2). Since some of these measurements series were taken on different days, the calibration transfer strategy described above has been implemented to match the sensitivities of pure samples.

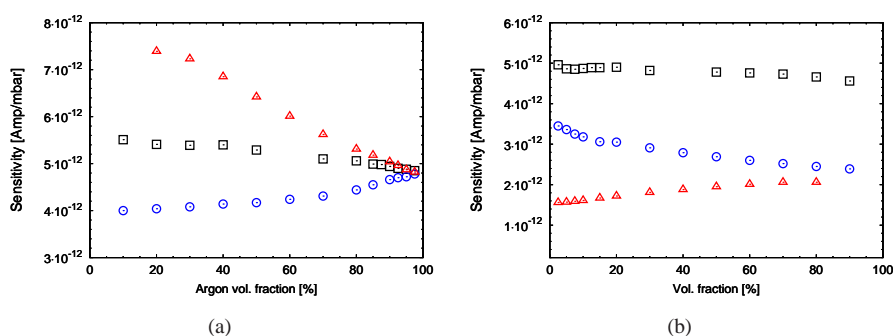


Figure 5.3: Mass spectrometer sensitivity in binary mixtures of H_2 (Δ), O_2 (\odot), CO_2 (\square) in Ar. a) Effect of the addition of the other gases on the sensitivity of argon. b) Sensitivity of H_2 , O_2 and CO_2 as a function of their volume fraction.

It can be seen from the results presented in figure 5.3(a) that the presence of hydrogen in the sample increases the sensitivity of the instrument for argon while oxygen

⁴In the determination of the instrument sensitivities, the atmospheric pressure is used as the reference state. This implies that the pressure drop in the sampling capillary is included in the calibration factor. The measured non-linearities are therefore the sum of the contributions of each component in the system, from the gas molecules sampled to the electrons counted at the other end. The interested reader is referred to appendix A for an analysis of the sampling and ionization part of the system.

decreases it. CO_2 has a small positive effect on the sensitivity, but less pronounced than for the two other species. To understand this phenomena, it should be noticed from figure 5.3(b) that the magnitude of the sensitivities differs significantly between the species. For instance, the sensitivity of the instrument to hydrogen is about 5 times smaller than for argon. Therefore, as the argon is replaced by hydrogen in the sample, the charge density in the ionization chamber and mass filter decreases. This hints towards space charge effects being one of the causes of the observed mixture dependence of the instrument sensitivity. The effect of water, the fourth species of interest, is shown in figure 5.4. As water added in a CO_2 sample, it can be seen that the sensitivity of both the H_2O and the CO_2 decreases. The phenomenon is similar in nature and magnitude to what was previously observed in O_2 and mixtures of argon.

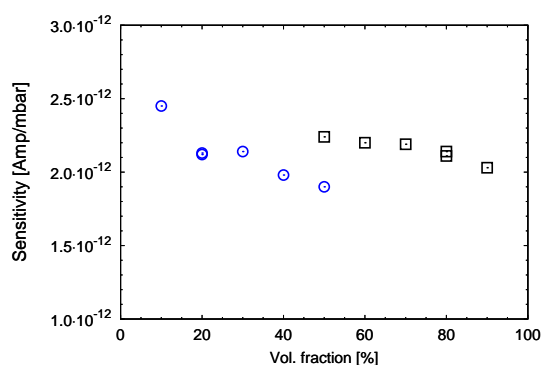


Figure 5.4: Mass spectrometer sensitivity variation in the presence of a variable amount of H_2O (\odot) in a CO_2 (\square) matrix.

The presence of O_2 , H_2O and to some extent CO_2 in a sample is known to induce oxidation and adsorption on the surface of the instrument exposed to these reactive gases. This results in changes in the properties of these surfaces intervening over the course of minutes to hours. When the exposure to the reactive gas is ended, these gases desorb from the surface which recovers some if not all of its initial properties. To study this effect, the composition of a binary mixture of argon and oxygen was changed several times over the course of a 6 hours period, the results are presented in figure 5.5. This experiment revealed that after initial exposure to oxygen, the system takes close to one hour to stabilize within 10% of its final sensitivity. The addition of 10% O_2 resulted in a 20% decrease of the instrument sensitivity to argon. Subsequent changes in the oxygen content of the mixture seemed to be equilibrated equilibrated slightly faster. These timescales had to be considered when conducting measurement over large oxygen concentration ranges. The sudden drops and recovery in both species sensitivity noticed between 2 and 3 hours are of unknown origin and have been observed sporadically. The global effect of these variation suggest that they are perhaps caused by partial and temporary blockage of the sampling system. In the event that such a variation were to become permanent, the calibration transfer procedure described in section 5.4.2 ensures that the instrument response is updated frequently.

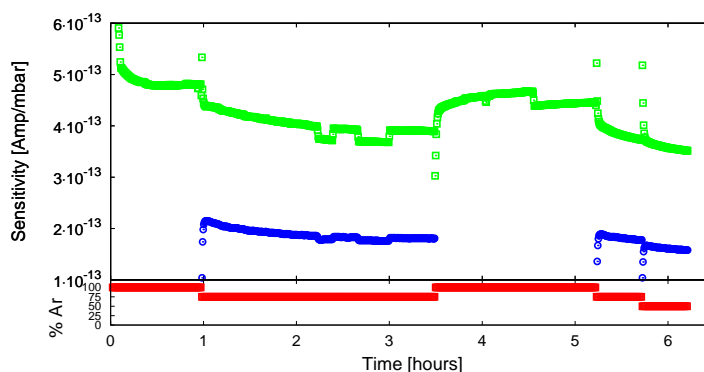


Figure 5.5: Time dependence of instrument sensitivity in a binary mixture of argon (\square) and oxygen (\circ).

Mixtures of three and four gases

In the simplest experiments presented in this thesis, the number of species present in the burning chamber is four and include both reactants, a single product and the inert. To properly characterize the mass spectrometer in this three-dimensional parameter space, a large number of reference mixtures evenly distributed in the region of interest were generated. For the measurements of concentration profiles in hydrogen-oxygen flames diluted in CO_2 , the ranges of interest are 0-50% for H_2 , 0-50% for H_2O , 0-75% for O_2 and 0-100% for CO_2 . For obvious reasons, an automated mixture generation setup was developed and is described in section 4.5. Mapping the sensitivity of the instrument in three gas mixtures (without water) using 49 reference composition sampled about 30 minutes each took a little over a day of measurements. An example of the sensitivity dependence in such a three gas mixture is presented in figure 5.6.

The addition of the fourth species to the mixture required the development of a precise water vaporization unit, described in section 4.5 to supply a controlled flow rate of water vapor to a heated mixture of the other three gases. The three gas procedure described above was then repeated 4 times with a different amount of water vapor to cover the range of interest for this species. This four gas calibration procedure required an extensive amount of time to be completed. Accordingly, to reduce the influence of the long term drift of the instrument on the accuracy of the calibration, the number of mixtures measured for each water concentration was decreased to 36 and the measurement time to 20 minutes. With these measures it was possible to complete the whole four-gas calibration in just under 48 hours. To ensure that the instrument long term drift did not induce a bias in the measurements, a pure sample of one of the species of interest was measured at regular intervals in the procedure to monitor the evolution of the absolute sensitivity. Unfortunately, the device available to supply the liquid water to the apparatus (a medical syringe pusher) required human intervention throughout this lengthy calibration process. It was necessary to change the syringe about every hour and manually set the flow rate, preventing the implementation of a truly automated procedure.

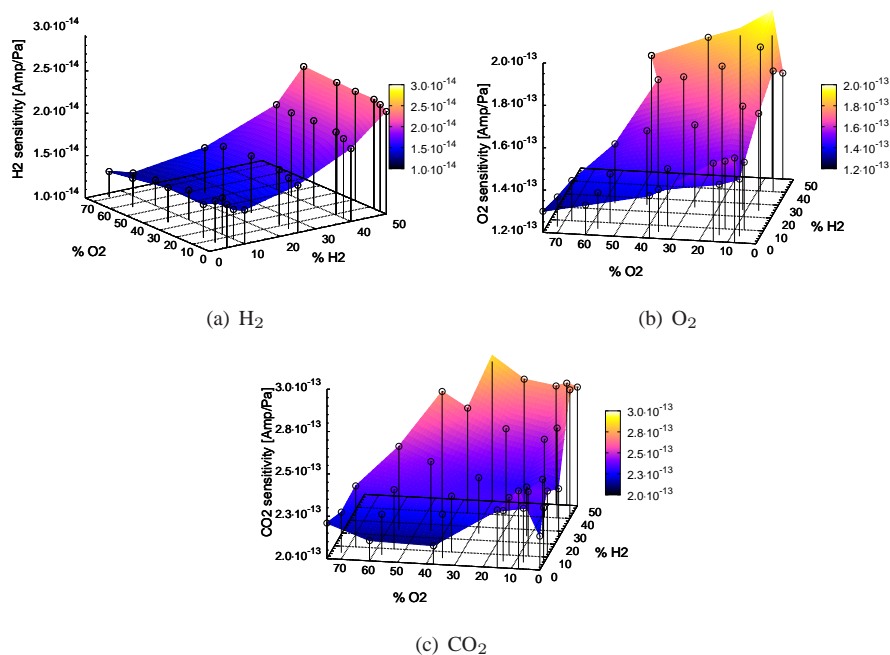


Figure 5.6: Mass spectrometer sensitivity in H₂-O₂-CO₂ mixtures. When the total of the volume fractions of the two species given on the base axes of the graph do not equal 100%, the remainder is CO₂.

Extension to more complex mixtures

To produce the wide ranges Lewis numbers necessary for the work presented here, a second inert must be added to the mixture. This means that the minimum number of species present in the burner climbs to five. From practical considerations it is evident that the calibration procedure described previously cannot be extended in its current form from four to five species. The time required to map such a complex parameter space implies that the state of the instrument cannot be assumed constant throughout the procedure. Accounting for this drift effect would add another level of complication to a process that does not need it.

The extension of the method to more complex gas mixtures therefore requires the use of a certain number of simplifying assumptions. The simplest solution would be to construct a multi-dimensional mapping of the instrument sensitivity from elementary knowledge gained in simple mixtures. Using the results from binary mixtures it is possible to quantify the effect that the concentration of a given gas has on the sensitivity of other gases. This approach was tested on the three gas mixtures presented in figure 5.6. However, no trick was found to account for the different effect of one gas on another as a function of the concentration of a third. It is believed that the interactions between the species are too important for such a simple approach to be effective.

One simplification can be found by exploiting the limit of infinitely fast combustion which specifies that the advected reactant should be consumed entirely at the flame. In the absence of leakage both reactants should therefore never be present simultaneously in any great amount at the same location in the burner. Each reactant can then be

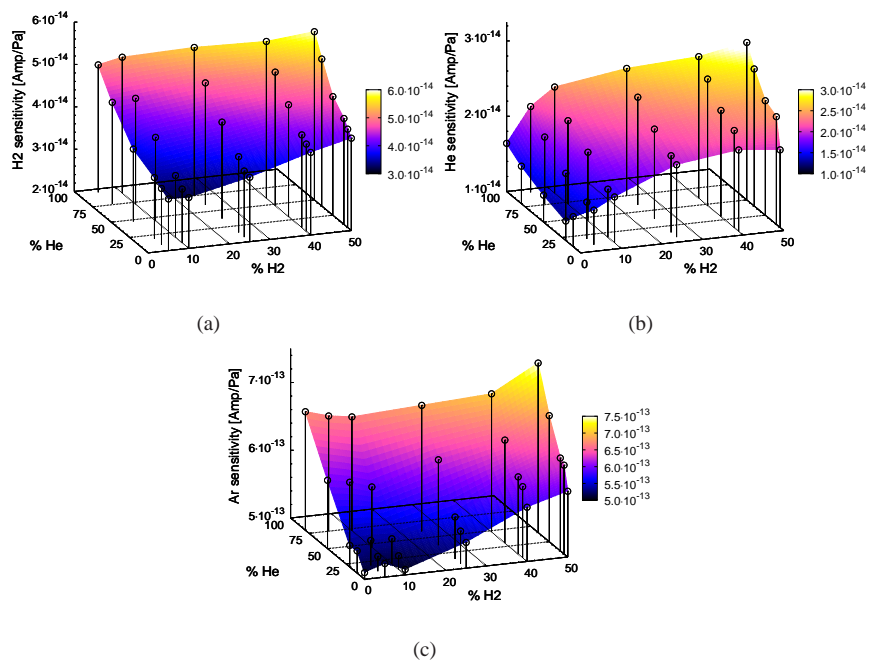
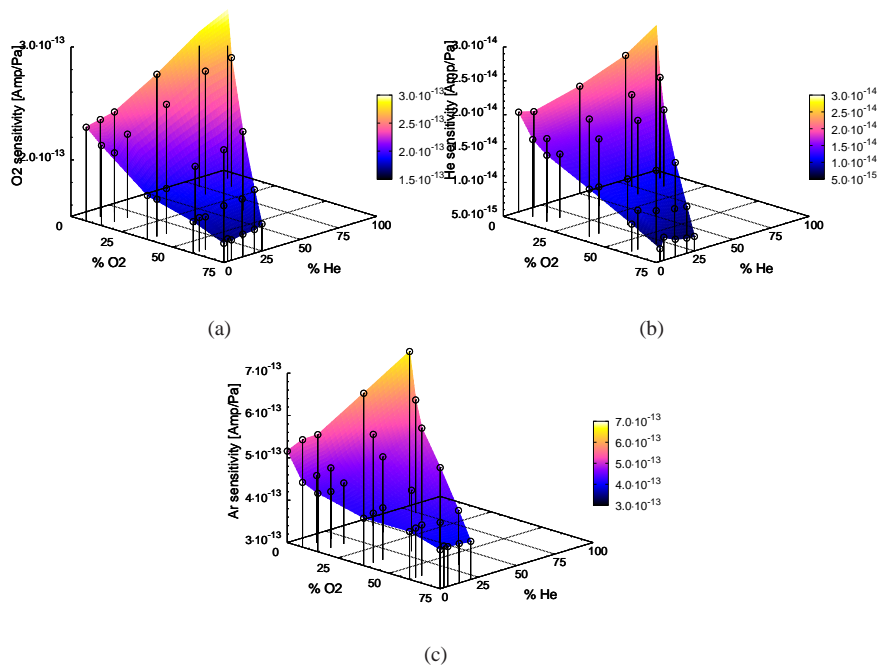
calibrated separately with the two inerts using the three gas procedure described previously. The effect of the product, water in this case, can be dealt with in the same fashion as previously, resulting in a mere doubling of the length of the calibration procedure from the four to the five gas scenario. Further simplification is possible by considering the effect of water as a multiplying factor applied on top of the three gas sensitivity maps available for each domain of the burner. The effect of the water concentration on the sensitivity of other gases can be derived from graphs such as the one presented for CO₂ in figure 5.4. This requires the assumption that the relative effect of H₂O on the instrument sensitivity is the same for every species which was measured to be reasonable for the H₂O range investigated here. The choice of the dataset to use for the mixture analysis will then be dictated by which of the reactants is present in the largest amount. The sensitivity of the scarce reactant was estimated from the other dataset by taking into account the general effect of the abundant reactant on other species.

The choice of the second inert to use in the five gas mixture was focused on finding an inert as light as possible, since it will result in higher Lewis number for the reactants. These high Lewis numbers are required to produce mixtures where the dominant thermal-diffusive instability mode close to extinction is intensity pulsations. This requirement made the choice of Helium natural. Unfortunately, the use of this gas complicates the calibration procedure since its very high ionization energy results in extremely low ionization efficiency and sensitivity. For reference, the typical sensitivity of helium measured here is 1/20 that of CO₂. The heavy inert used was only chosen sufficiently different from helium to ensure that the range of Lewis numbers produced was sufficiently wide to conduct meaningful experiments. Even if CO₂ is used in most of the combustion experiments, argon was also investigated because it is of similar weight but is known to be much more simple to measure in mass spectrometer systems. Examples of three gas sensitivity maps for both the fuel and the oxidant sides of the burner are presented in figure 5.7 and 5.8, respectively.

The use of helium and argon as the inert mixtures illustrates the effect of a large change in the mean properties of the mixture on the instrument sensitivity. The most important of these properties appear to be the mass and the first ionization energy. The graphs of figure 5.7(a) and 5.7(b) show a factor two change in the sensitivity of H₂ and helium as a function of mixture composition. The lowest sensitivities are associated with the highest concentrations of argon in the mixture. The calibration of the oxidant side presented in figure 5.8 yield similar results for O₂ and helium. A comparison between the two sides reveals that the sensitivity of argon seems to be more affected by the presence of O₂ than that of H₂.

5.4.3 Results and discussion

The effectiveness of the calibration method implemented was assessed regularly by measuring reference mixtures of known composition. At the beginning of each day of measurement, a reduced *transfer set* of mixtures was analyzed to perform the calibration transfer. Following this adjustment, a few other reference mixtures representative of the experiment being conducted at the time were measured. This provides an estimation of the error associated with the current measurements. The results gathered following this calibration update and verification routine over the course of 2 months are presented in figure 5.9. These results include the error evaluation for H₂, O₂, helium and CO₂. The measurement of reference samples containing water vapor generally yielded an error of about 5% for H₂O. The verification of measurements of the samples with a water content was carried out less often than for the other species because

Figure 5.7: Mass spectrometer sensitivity in H₂-He-Ar mixtures.Figure 5.8: Mass spectrometer sensitivity in O₂-He-Ar mixtures.

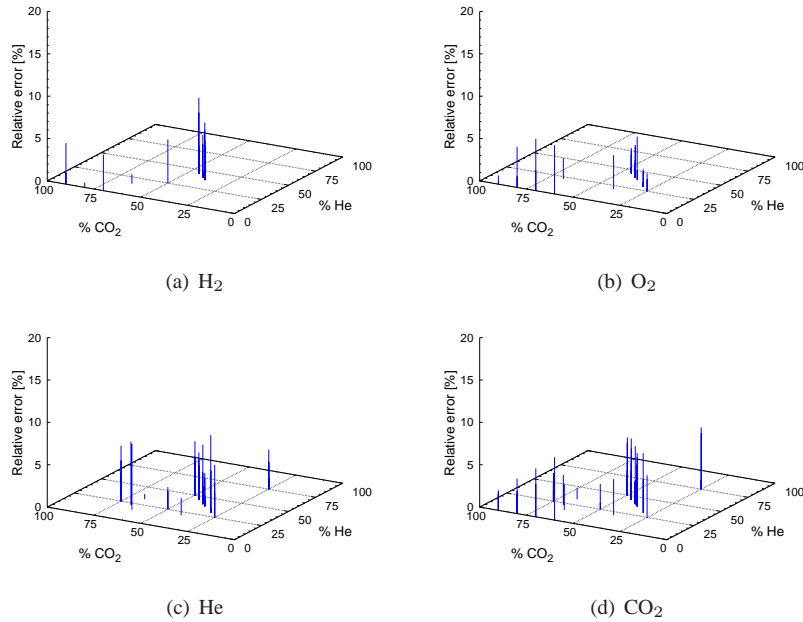


Figure 5.9: Evaluation of the mass spectrometer measurement error after the implementation of the five gas calibration.

of the long startup times associated with the vaporization apparatus.

To determine the effectiveness and usefulness of the complex calibration procedure implemented here, the measurements were also analyzed using a constant sensitivity. This average was determined from the available sensitivity maps of each species and yields results that should be expected from a simplistic approach neglecting the mixture dependences of the instrument response. In the results reported in figure 5.10 using this rudimentary calibration the maximum errors are close or exceeding 20% for every species. Achieving these relatively poor results still requires the implementation of a substantial calibration procedure to improve on the performance of the instrument as it is delivered from the manufacturer. Following the default mixture analysis approach and using a single sensitivity for all species would certainly have resulted in far worst results.

Comparatively, the results calibrated using the extensive five gas calibration presented here have a maximum relative deviation of 10% with respect to the reference mixtures measured. Over 100 such measurements were made and the typical errors associated with the oxidant volume fraction has been lower than 5%. This value is of special significance since when the fuel is advected to the flame, only the oxidant concentration at the counter-diffusing injection is required to define the mixture strength prevalent in the burner. The uncertainty on ϕ as measured by mass spectrometry is therefore believed to be on the order of 5% for the results presented in this thesis. More generally, the implementation of the extensive calibration procedure described in this section has allowed the error associated with the mass spectrometry measurements to be divided by at least a factor three.

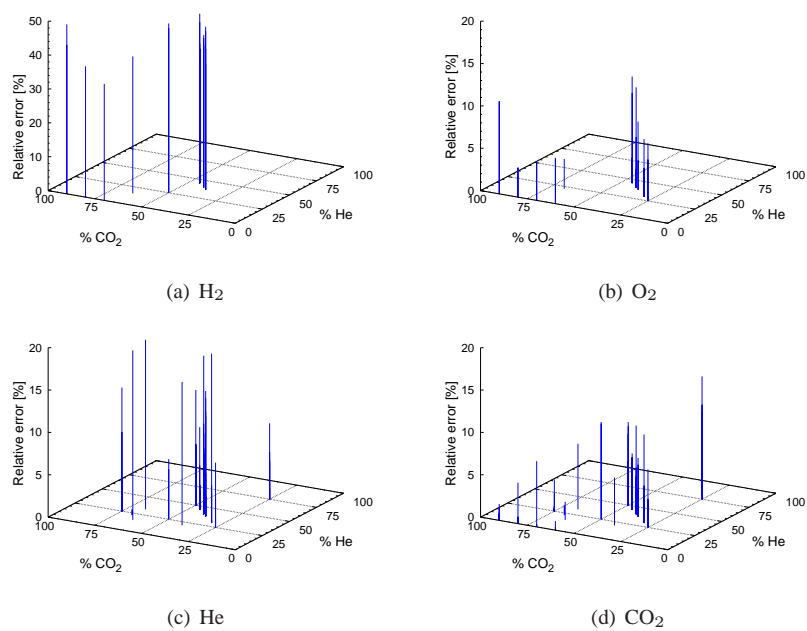


Figure 5.10: Evaluation of the mass spectrometer measurement error with rudimentary calibration, overlooking the mixture dependence of the instrument sensitivity but still considering its species specificity.

Chapter 6

Burner characterization

For the comparison between this experiment and the theoretical models to be of any significance, the burner and the flame it produces must first be characterized. The set of measurements presented in this chapter include data on the velocity, species and temperature distributions over the burning chamber width and length. The injection layer immediately next to the counter-diffusing species supply needles was investigated to ensure that it did not induce perturbations on the flame. The resulting flame shape was also measured along with its parasitic curvature and the parameter resulting in hydrodynamic instabilities (Rayleigh-Bénard convection cells). To assess how well this experimental realization approaches the idealized one-dimensional theoretical configuration, the flame position and the longitudinal species concentration profiles are compared to the theoretical relationships obtained from the simplified theory.

The burner used here is very versatile, allowing control over many parameters defining the diffusion flame generated. The bulk flow, reactant concentration at each end of the chamber as well as the nature and concentration of the inert gas mixture used can all be controlled independently. For the sake of simplicity, only a small number of stable flames configurations were used for the different measurements made to characterize the burners. The main operating parameters used for these flames are given in table 6.1. For all of these, hydrogen was used as the fuel since the mass spectrometer calibration was developed specifically for H_2 - O_2 flames. For simplicity considerations, the fuel was always the advected species in this chapter, except for specific measurements regarding flame position.

Config.	Burner	Advected mixture			Inert	Diffusing mixture	
		Fuel [%H ₂]	F.R. [SLPM]	U [mm/s]		Oxidant [%O ₂]	F.R. [SLPM]
Flame #1	I	30	2.25	17.7	CO ₂	100	3.0
Flame #2	II	35	7.0	19.4	CO ₂	100	8.0
Flame #3	II	35	7.5	20.8	CO ₂	90	7.0
Flame #4	II	35	8.5	23.6	CO ₂	90	7.0

Table 6.1: Parameters used to generate the stable flames used for burner characterization.

6.1 Flame shape

The shape of the stable flames produced in the Mark I and II is presented in figure 6.1a) and b), respectively. The photographic technique described in section 4.2.1 was used to capture these images. The red lines drawn on top of the flames represent the flame sheet location as determined by the position of the maximum visible light emission. The observed light is emitted through two distinct mechanisms. First and foremost, flames are chemiluminescent [107] with a peak of luminosity in the primary reaction zone. Chemical reactions radiating discrete lines or bands of frequencies in the visible part of the spectrum are numerous for carbon containing fuels and involve species such as C_2 and CH . For the hydrogen flames studied here the emission of the species excited in the reaction zone (OH^- and H_2O) fall in the ultraviolet part of the spectrum. As a result, H_2-O_2 flames emit very little visible light and are essentially invisible to the naked eye. The second source of light is the blackbody radiation emitted by the heated gas molecules and solid particles in the flow, the frequency of which increases with temperature. The temperature range of H_2-O_2 flames results in the blackbody radiation emitted falling mostly in the infrared range. Moreover, absence of carbon soot implies that it only emanates from the gas molecules, making it very faint.

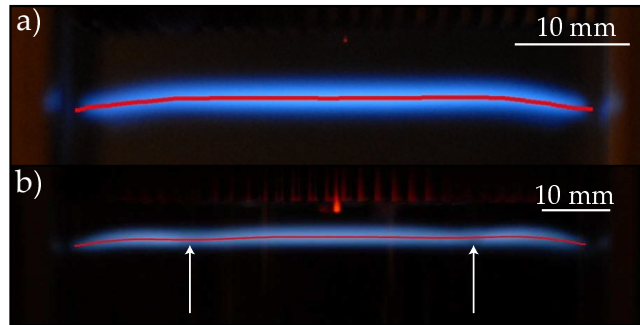


Figure 6.1: Flame shape observed in the burners using typical operating conditions, with the fuel advected. (a) Mark I burner, (flame #1) bulk velocity $U = 17.7$ mm/s. (b) Mark II burner, bulk velocity $U = 20.8$ mm/s (flame #3), with the white arrows indicating the position of the inner quartz cylinder. The red lines represent the location of the maximum light emission, associated with flame location.

The choice of the inert used for the dilution of the reactants used in this thesis was guided to increase the luminosity of the reaction zone. The presence of CO_2 allowed the flames to be visible to the naked eye and conventional photographic equipment to be sufficiently sensitive to measure them. When used in conjunction with helium for the dilution, at least 5% to 10% of CO_2 in the mixture was necessary to yield a visible flame. The use of noble gases only would have been convenient since they are significantly less complicated to measure with the mass spectrometer than CO_2 . However, dilution with only He produced entirely invisible flames and the tests made using argon (either alone or in conjunction with He) resulted in very dim greenish flames impossible to capture with the available equipment.

The enhanced luminosity of the reaction zone in the presence of CO_2 results in low-level continuum radiation in the blue region of the spectrum [107]. The continuous nature of this radiation is in contrast to the line or band emission of chemiluminescence

which takes its origin in electronic transitions between quantized states in an atom or molecules. The continuous emission of CO_2 observed in the $\text{H}_2\text{-O}_2$ flame used here is believed to take its origin in the excitation or ionization and recombination of the molecule in the reaction zone [149]. Water vapor is also known emit in the same way [47, 150], but apparently not sufficiently to allow observation in $\text{H}_2\text{-O}_2$ flames without CO_2 . The intensity of the visible light emission is therefore considered a reliable indicator of the position of the flame front [107].

An example of the measure light emission profiles across the flame sheet, extracted from figure 6.1b), is presented in figure 6.2. As expected, the blue component is the strongest and was used preferentially to determine the flame position. When this channel was found saturated in certain images, the green and red components of the profiles were used alternatively. The width of the light emitting region, measured as the full width at the half of the peak height, (Full Width Half Maximum, FWHM) was found to be 2.83 mm for the typical stable flame encountered in the Mark II burner and presented in figure 6.1b). The measured light results from the band emission of CO_2 mentioned above which peaks in the reaction zone and extends in the equilibration region downstream [107], explaining the relatively thick luminous layer. Accordingly, the light emission profile is not indicative of the reaction zone thickness but its maximum intensity can be used to identify its location.

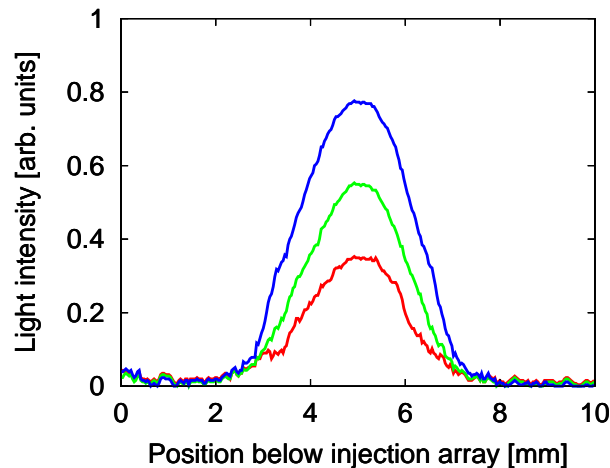


Figure 6.2: Profile of the flame visible light emission for each of the three channels of the RGB image, extracted from the flame presented in figure 6.1b). The width of the light emitting zone (FWHM) is 2.83 mm.

6.1.1 Flame parasitic curvature

The great care taken to minimize thermal and flow inhomogeneities in the burner resulted in the very flat flames presented in figure 6.1. The flame sheet found from the location of maximum light emission and illustrated with the red lines of figure 6.1 nevertheless exhibit parasitic curvature. This quantity was measured because it plays a role in the residual stretch experienced by the flame. The angle between the vector normal to the flame sheet and the vertical axis is presented in figure 6.3 for both the Mark I and

the Mark II version of the burner. This data is extracted from both pictures of figure 6.1 plus another flame (#4) with slightly faster bulk flow in the Mark II burner.

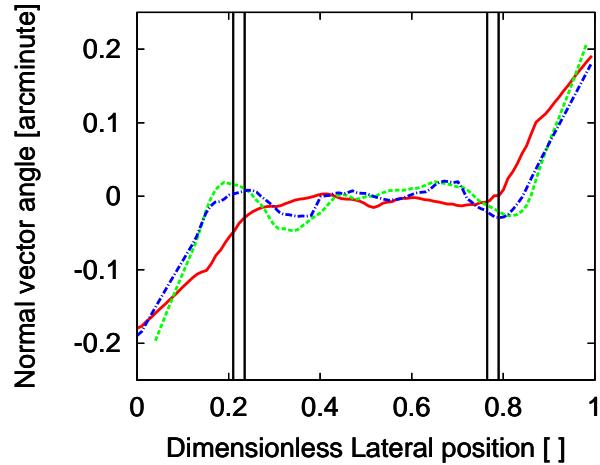


Figure 6.3: Angle of the vector normal to the flame sheet for typical conditions, in minutes or arc. In red for the Mark I version of the burner (flame #1 —, 30% H₂ in CO₂, 100% O₂ and $U = 17.7$ mm/s), in green and blue for the Mark II version (--- flame #3: $U = 20.8$ mm/s, 30% H₂ in CO₂, 100% O₂, --- flame #4: $U = 23.6$ mm/s).

The data presented in figure 6.3 confirm that the flame is extremely flat in the central portion of the burner. The small parasitic curvature results in the vector normal to the flame sheet pointing away from the vertical by less than 1/20 of a minute of arc. In this figure, the solid line is from a flame in the Mark I burner while the two dashed lines are from two distinct flames in the Mark II burner. Also picture is the location of the inner quartz cylinder, described in section 4.1.2 and used to isolate the most stable central part of the burner. From this figure it can be seen that the significant curvature is effectively kept outside the cylinder, with an almost perfectly flat flame on the inside. Part of the small variations observed in the central flame in the Mark II burner results from reflections on the inner cylinder causing slight errors in the optical determination of the flame location. These are small enough to induce only minimal errors in the determination of the flame stretch.

6.1.2 Formation of convection cells

The location of the hot layer that constitutes the flame below the colder injection array brings the question of the stability of this temperature stratification to hydrodynamic disturbances. The stability of a fluid layer sandwiched between differentially heated boundaries is one of the classical problems of fluid mechanics pioneered by the work of Lord Rayleigh and Henri Bénard. They showed that if a dimensionless number accounting for the effects of buoyancy, viscosity, momentum diffusivity and thermal diffusivity is high enough, the steady-state conduction mode becomes unstable and convection cells develop. This dimensionless number shown in equation 6.1 is called the Rayleigh number Ra and the critical value at the onset of the instability is Ra_C .

$$Ra = \frac{g\mathcal{B}}{\nu D_{th}} (T_1 - T_2) d^3 = GrPr \quad (6.1)$$

In this expression, g is the gravity acceleration, \mathcal{B} the thermal expansion coefficient, ν the kinematic viscosity and D_{th} the thermal diffusivity. The temperature difference is between the hot and cold boundaries, kept at temperatures T_1 and T_2 , respectively. The last parameter is the separation between the two boundaries d , which has a strong influence and is included to the third power. The Rayleigh number can also be expressed by the product of two other dimensionless numbers: the Grashof number and the Prandtl number. The Grashof number is the ratio of buoyancy and viscous forces while the Prandtl number accounts for the balance between thermal and momentum diffusivities. Treatments of this problem in the literature abound, the interested reader is referred to the classical book of Chandrasekhar [151] and the recent review of Bodenschatz et al. [152]. Variations on the classical configuration are also investigated with the introduction of complications such as a Poiseuille flow parallel to the boundaries [153].

In the burner, the problem is further complicated by the bulk flow going through the system, *perpendicular* to the temperature gradient. Additionally, the two boundaries need to be considered free because the flow is not restrained between the needles. This uncommon configuration has received little attention from theoreticians and experimentalists. A similar configuration exists industrially in the porous media of fluidized bed reactors which has received some attention [154] and the problem has also been treated analytically [155]. The most useful analysis found in the literature, albeit on a different scale, was found in atmospheric sciences and focuses on convection induced cloud formation. The extensive theoretical and experimental work of Krishnamurti [156, 157, 158] provides stability considerations including a large number of parameters.

The results of interest here is the influence of the bulk flow magnitude and direction on the stability of the layer. From the classical treatment of the problem it is known that the layer will be marginally stable for a critical Ra_c of approximately 1708 if both boundaries are rigid and 657.5 if they are both free [151]. The effect of a bulk flow directed from the hot to the cold boundary, such as in the burner used here, can have an opposite effect depending on the Prandtl number [156]. Small Prandtl numbers such as those prevailing in the burner (on the order of $Pr = 0.7$), we can expect the critical Rayleigh number at which convection cells will develop to *decrease* with increasing bulk velocity. This effect can be illustrated by considering the opposite case where a high Prandtl number results in thin thermal boundary layers on both sides of the domain considered. The addition of the bulk flow increases the boundary layers thickness and induces a curvature in the conduction profile. As a result, although the temperature gradient remains unchanged, it extends over a shorter depth and it follows an increase in the critical Rayleigh number.

When the flame position was lowered too far from the injection array, this resulted in the collapse of part of the flame and formation of stationary ridges in the reaction sheet, such as those shown in figure 6.4. Once the flame had collapsed, a strong hysteresis effect was observed, presumably from the heating of part of the injection array on either side of the burning chamber. The critical flame offset d of 12 – 15 mm achievable while maintaining a planar flame results in a critical Rayleigh number in qualitative agreement with the theoretical works mentioned above. Considering the uncertainties on the measured flame and injection array temperatures and the large number of parameters involved no further attempts were made toward a quantitative comparison.

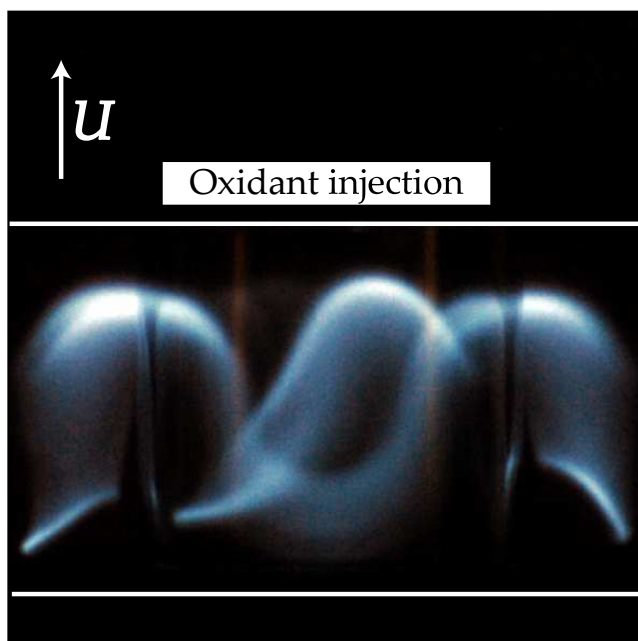


Figure 6.4: Flame pattern observed when the flame position is low enough below the injection array to result in the formation of convection cells in the burner.

6.2 Velocity measurements

6.2.1 Injection layer

The trick used to supply the counter-diffusing reactant to the burning chamber described in section 4.1.1 introduces localized inhomogeneities in the burning chamber. The introduction of hundreds of tiny jets in the bulk flow forms a thin region where the reactant intermixes with the flow of products. This region is called the *injection layer* and must be measured to ensure that it does not perturb the flame. The main concern is the determination of the thickness of this layer outside of which the transport of species can be considered strictly one-dimensional.

The only technique available with sufficient spatial resolution and the non-invasive character required to probe the narrow jets produced by the injection needles is Laser Doppler Anemometry (LDA). The velocity was measured following the procedure described in section 4.3.1. Unfortunately, it was impossible to seed the counter-diffusing species mixture with tracer particles since they tend to stick to the metal walls of the thin tubes of the injection arrays. Consequently, LDA measurements could only be carried out in the Mark I version of the burner where the bottom advected reactant is inserted through larger diameter tubes. The measurements were made without a flame present in the burner. When the burner is hot, the SiO_2 seeding particles used become polarized from the pyroelectric effect and tend to stick to the burner windows above the flame. As a result, frequent shutdowns and cleanups are required, interrupting the long acquisition times required to scan the region of interest.

Where the unseeded jets exiting the injection needles meet the seeded bulk flow,

the tracers are scarce and travel mostly vertically with the bulk flow. As a result, long integration times were necessary to gather a usable signal and compressed air was used in both streams to save pure gases. The transverse velocity profiles presented in figure 6.5 are taken at progressively greater depth below the injection arrays. Only the vertical component of the velocity is plotted since the horizontal component of the LDA produced no usable signal from the small velocities along this axis and the limited seeding issues mentioned above. The measurements of figure 6.5 show that the jets emanating from the needles have an effect on the bulk flow down to between 2.5 and 3.0 mm below the injection array.

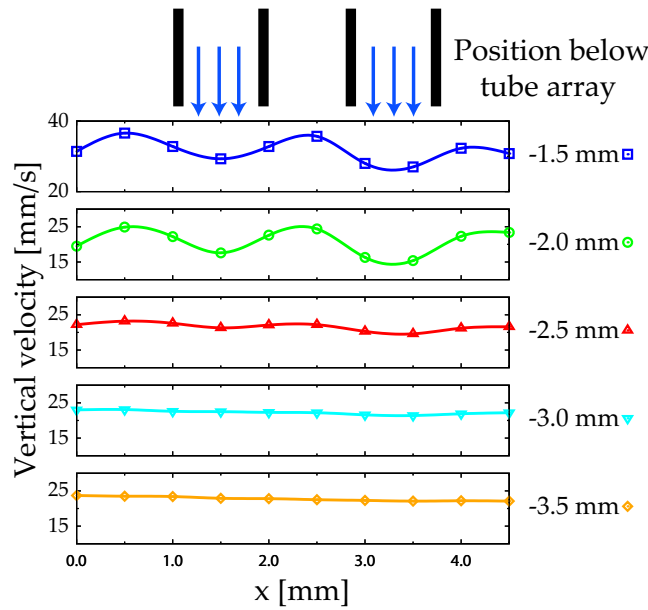


Figure 6.5: Velocity profiles taken at different depths below the injection array in the Mark I version of the burner. The injection layer thickness is seen to be between 2.5 and 3.0 mm.

The value of 2.5 mm is considered the upper bound for the injection layer thickness since the typical bulk velocity in the burner when considering thermal expansion are higher than the value used for this experiment. Moreover, this value is the velocity injection layer and the species concentration injection layer is likely to be smaller from the effect of diffusion. Below this layer, the flow can be considered one-dimensional with the transport of the species injected from the top being done only by diffusion against the bulk flow. All of the results presented in this thesis from this point onward have been gathered in this one-dimensional portion of the burner.

6.2.2 Transverse velocity profiles

The one-dimensional character of the flow throughout the burning chamber was verified by taking velocity profiles across the entire burner cross section at different heights. These measurements were taken with a flame present in the burner and using LDA when possible. In the region of the burner where these measurements are carried

out, below the flame, the seeding is good and the temperature relatively low. This means that more data points could be gathered before the windows became opaque from the accumulating seeding particles compared to the injection layer measurements presented above. The velocity profile span almost the entire width of the burner but the detailed measurements of the velocity boundary layers on the walls is prevented by limited optical access.

Mark I burner

In the Mark I version of the burner, it was possible to use LDA as in section 6.2.1 to get two components of the velocity. The resulting velocity vectors taken across the midplane of the burner are presented in figure 6.6. The uppermost profile was taken in the flame itself and each successive profile below it at increments of 5 mm. From this figures it can be seen that the flow is not homogeneous at the bottom of the burner. This is attributed to the limited performance of the flow equalization chamber used on the advected side of the Mark I burner. The imperative of letting the seeding particulates go through unimpeded prevented the use of a pressure drop sufficient to ensure uniform velocity distribution.

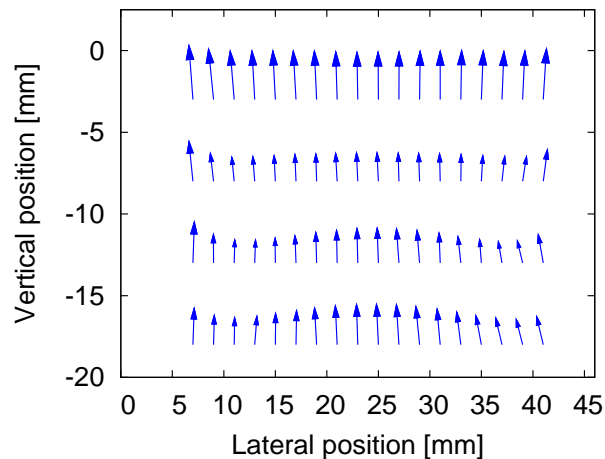


Figure 6.6: Vector plot of the velocity in the midplane of the Mark I burner. The uppermost profile is take in the flame itself.

As can be seen in the two uppermost profiles of figure 6.6, as the flow approaches the flame it becomes significantly more homogeneous as it is accelerated following thermal expansion. This can be more easily seen in figure 6.7, where each component of the velocity was plotted separately. From these plots, the burning chamber below the flame can be separated in two regions. In the lower part of the burner the flow is converging slightly towards the center of the burner but the opposite is observed when approaching the flame. From the horizontal component of the velocity it can be seen that this phenomenon is more pronounced on the right side of the burner. Since it is on that side that the ignition port is located, inducing higher heat losses, this converging-diverging flow can probably be attributed to thermal effects at the windows.

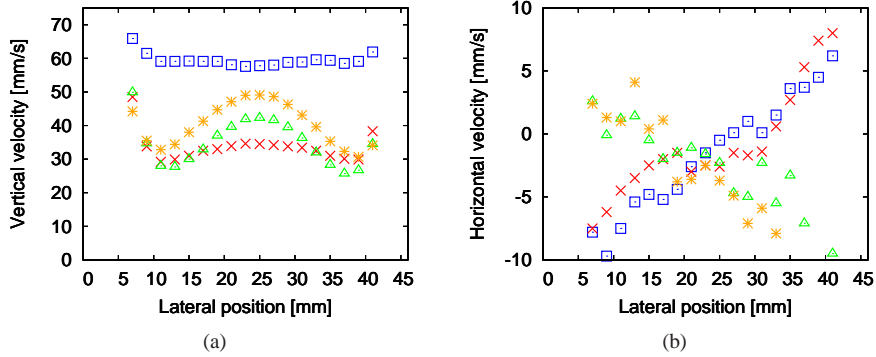


Figure 6.7: The two components of the velocity in the Mark I burner plotted separately. The same profiles as in figure 6.6 are used, taken at different heights in the burner: at the flame(\square) and below the flame (5 mm (\times), 10 mm (\triangle), 15 mm ($*$)). (a) Vertical component. (b) Horizontal component.

Mark II burner

Using the thermistor-based system described in section 4.3.2 it was also possible to get some measurement of the velocity distribution in the Mark II version of the burner. However, since the probe used is not directional, only the absolute magnitude of the velocity could be determined. This measurement could not be realized with a flame present in the burner, the thermistor having a maximum operating temperature of 250°C. Therefore, cold air was used to supply both streams. The profile shown in figure 6.8 was taken at half the height of the burning chamber. The relatively large size of the probe assembly used (about 5 mm diameter) prevented the detailed measurements of the boundary layers on the chamber walls. Nevertheless, the first data points on either sides of the profile still reveal the influence of the walls.

Comparing the Mark II profile of figure 6.8 to the ones taken at similar heights in the Mark I burner presented in figure 6.7(a) reveal that the velocity is much more uniform in the new version of the burner. This difference is attributed partially to the absence of a flame in these measurements but also to the improved injection plenums used in the second version. The long plenums (80 mm) allowed the use of numerous devices (screens, porous plates, honeycomb sections) to ensure homogeneous supply to the injection needle array. The new plenum design and the needles themselves induced a pressure drop in the advected species injection path sufficient to ensure a flat velocity profile throughout the burning chamber. The previously mentioned drawback of this approach is that the flow can no longer be seeded for LDA-based velocity measurements.

6.2.3 Residual strain

Transverse velocity profiles such as the uppermost one from figure 6.6 taken *inside* a stable flame typical of those encountered in this thesis allow the evaluation of the residual stretch imposed on the flame. This quantity is of critical importance because of the strong stabilizing effect it has on the thermal-diffusive instabilities. In the theoretical models it is expected to be zero but experimentally there is no such thing and inhomogeneous

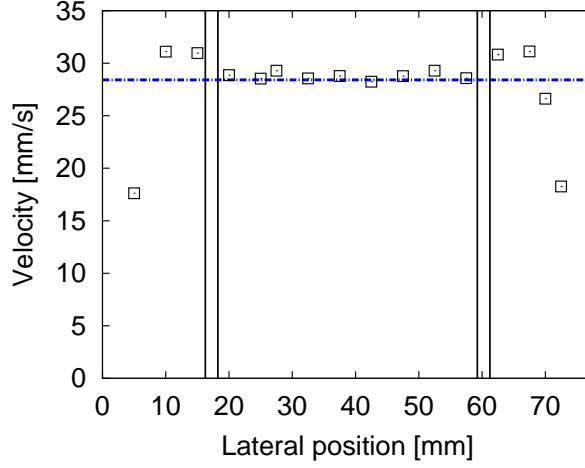


Figure 6.8: Transverse velocity profile in the Mark II version of the burner without a flame present acquired using the hot thermistor technique. The Black vertical lines represent the position of the inner quartz tube walls. The horizontal dashed line is the average value expected from the supplied flow rate (28.41 mm/s).

ogeneity in the velocity distribution will induce a finite strain that must be quantified. The flame stretch K is a measure of rate of deformation of a surface element of the flame sheet of area A as expressed by the following relation [159]:

$$K = \frac{1}{A} \frac{dA}{dt} \quad (6.2)$$

Accordingly, a stretched flame has a positive value of K while a compressed flame results in a negative K . The introduction of the concept is attributed to Karlovitz et al. [160] with the specific form of equation 6.2 depending on the geometric flame configuration. These authors investigated jet flames, where the reaction zone is located in a velocity gradient and found the the following form for the stretch rate:

$$K = \frac{1}{\delta} \frac{1}{U} \frac{dU}{dy} \quad (6.3)$$

This expression for the stretch rate is known as the Karlovitz number where U is the velocity parallel to the flame sheet and y the coordinate normal to it. The parameter δ is a diffusion length defined as $\delta = \lambda / \rho C_p S_f^0$ where λ is the thermal conductivity, C_p the specific heat and S_f^0 the adiabatic flame speed. The Karlovitz number is sometimes considered as a general definition of strain, but it is valid only in the specific configuration where it was developed. A general expression for flame stretch was derived by Matalon [161, 162] and is presented in equation 6.4. This formulation was selected because it is dependent upon physically measurable quantities, is independent on the flame configuration and the choice of coordinate system.

$$K = V_f \nabla \cdot \vec{n} - \vec{n} \cdot \nabla \times (\vec{v} \times \vec{n}) \quad (6.4)$$

Equation 6.4 was developed for the case of premixed combustion with V_f the flame sheet propagation speed projected on its normal vector \vec{n} and \vec{v} the velocity vector. In

diffusion flames, the reaction front does not propagate and the stretch equation used must be modified by setting $V_f = 0$. What remains is only the second term of equation 6.4, that can be expanded using the triple product rule in the following way:

$$\begin{aligned}
 K &= -\vec{n} \cdot \nabla \times (\vec{v} \times \vec{n}) \\
 K &= -\vec{n} [\vec{v}(\nabla \cdot \vec{n}) - \vec{n}(\nabla \cdot \vec{v}) + (\vec{n} \cdot \nabla)\vec{v} - (\vec{v} \cdot \nabla)\vec{n}] \\
 K &= -(\vec{n} \cdot \vec{v})(\nabla \cdot \vec{n}) - \vec{n} \cdot \left(\frac{1}{2}(\nabla\vec{v} + (\nabla\vec{v})^T)\right) \cdot \vec{n} \\
 K &= -(\vec{n} \cdot \vec{v})(\nabla \cdot \vec{n}) - \vec{n} \cdot E \cdot \vec{n} = K_c + K_s
 \end{aligned} \tag{6.5}$$

In this last equation, E represents the rate of strain tensor [163, 162]. The first term isolated in equation 6.5 represents a contribution of the flame curvature to the flame stretch that was hidden in the second term of equation 6.4. The second term of equation 6.5 is the change in flame surface area induced by the strain in the flow. The total stretch experiences by the flame is therefore the superposition of the stretch contributions induced by the flame front curvature (K_c) and by the flow strain (K_s), even in the absence of flame propagation.

Using this formula, a velocity profile taken in the flame front such as the one presented in figure 6.9(a) and the flame shape extracted from figure 6.1 it is possible to quantify flame stretch. The result is presented in figure 6.9(b) with total stretch and the separate contributions of curvature and strain plotted separately. As expected, the residual stretch is extremely low, below 0.15 s^{-1} everywhere in the burner. It should be noted that these results are from the Mark I burner since only in this version LDA could be used to gather the velocity vector field. From the data presented in figure 6.3 it is reasonable to expect that the maximum stretch in the Mark II version of the burner should be of the same order of magnitude. In this version, the central portion of the burner where measurements are conducted is shielded from the slightly stretched flame edges by the quartz cylinder. In the corresponding region of the Mark I burner, the stretch is below 0.05 s^{-1} and this value is expected in the center of the quartz cylinder in the Mark II version. However, it is necessary to remember that this inner quartz cylinder will induce a velocity boundary layer in the inner flame, which will cause its edges to be slightly more stretched than its center. However, without LDA velocity measurements, the magnitude of this stretch is impossible to quantify more precisely than the values given above.

6.3 Temperature measurements

The flame temperature was measured using thermocouples following the procedure described in section 4.4. A picture presenting two probes in the burner with a stable hydrogen flame present is shown in figure 6.10. The triangular shape of the probes was chosen to minimize the conduction losses of the thermocouple junction by placing the junction wires parallel to the temperature gradient. Because of this design choice, the temperature measurements could not be done with the inner quartz cylinder present in the burner. The measurements were done in the Mark II version of the burner with the size of the probes necessitating the use of the longer burning chamber length setting of 40 mm. The parameters used are typical for the stable flames presented in this chapter and are listed under flame #2 in table 6.1.

Great efforts were taken to mitigate the effects of catalytic heating and radiation losses of the thermocouple junction, as described in section 4.4. The effect of the coat-

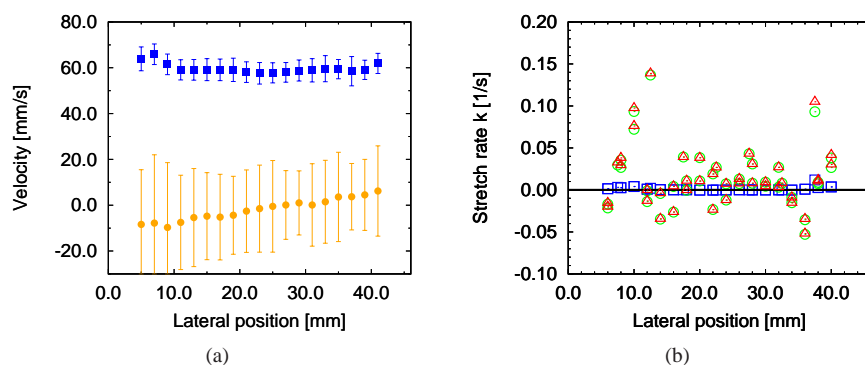


Figure 6.9: Velocity profile and residual stretch in the flame sheet. (a) Velocity profile used in determining the flame stretch, taken from figure 6.6. (b) Profile of the residual stretch experienced by the flame, with \square the contribution from flame from curvature (K_c), \circ the flow induced strain (K_s) and \triangle the total flame stretch.

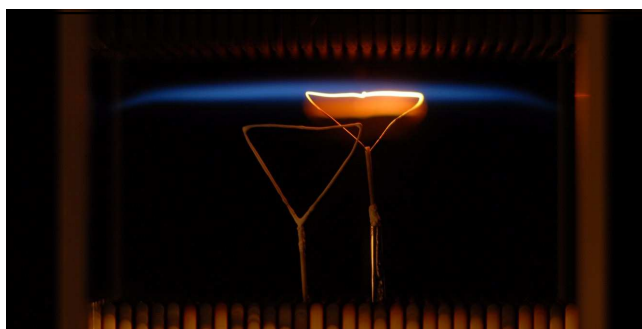


Figure 6.10: Picture of thermocouple probes inserted in the burner. The probe on the left is coated with ceramic adhesive while the one on the right is left bare.

ing used to shield the probes can be seen in figure 6.11(a) were the measurements from uncoated and coated thermocouples is presented. As expected, in this figure the catalytic activity of the platinum present in the thermocouple alloy promotes recombination reactions on the probe surfaces, raising its temperature. The uncoated thermocouple registers a maximum temperature of 1720 K while the coated one only measured 1532 K, for a difference of 188 K. However, since the measurements presented in figure 6.11(a) are not corrected for radiation, the real temperature increase caused by catalytic effects is somewhat lower. The diameter of the coated thermocouple being larger and its emissivity greater, its measured temperature is lowered more by radiation than that of the bare probe.

Nevertheless, this effect remains important for the accuracy of the measurements. Further proof of the strength of the platinum induced catalysis was clearly visible shortly after the flame was extinguished. As the unburned reactants located in the exhaust plenums diffused back in the chamber, they participated in surface reaction on the bare probe material. In figure 6.11(b), this resulted in the uncoated thermocou-

ple becoming incandescent from the surface reactions, with a measured temperature of 1400 °C without a flame in the burner. The phenomenon lasted from 5 to 10 minutes after the flame was extinguished and was sufficient to reignite the flame if the flow of gases was restored.

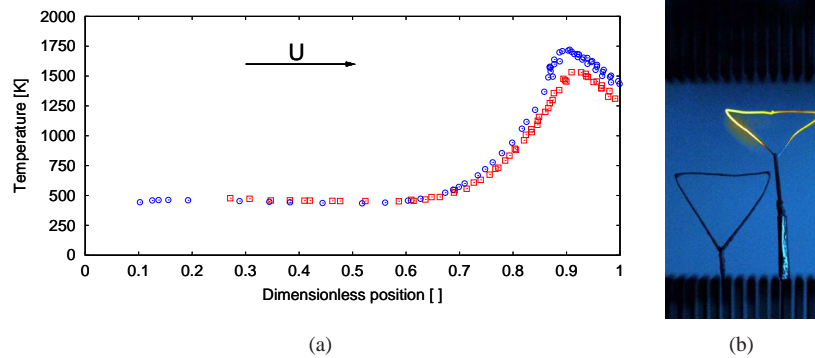


Figure 6.11: (a) Longitudinal temperature profiles from coated (\square) and uncoated (\circ) probes (flame #2). (b) Catalytic effect on platinum wire resulting in incandescent wire even in the absence of a flame.

The measurements were corrected for radiation following the procedure described in section 4.4.3 with values of the emissivities used for the radiation correction given in that section. The magnitude of the radiation correction as a function of the temperature, for a coated probe, is given in figure 6.12. For the measurements of the maximum flame temperature, the radiation correction reaches about 350 K. In this figure, the two datasets illustrates the effect of neglecting the radiation received by the probe from the enclosure walls. This simplification results in an overestimation of the radiation correction of 25 K relative to the assumption of a representative wall temperature of 500 K. For the results presented from this point onward, the radiation received from the walls will be included in the calculation of the radiation correction.

The radiation corrected data for the uncoated and coated probes is presented in figures 6.13(a) and 6.13(b), respectively. In these figures, the solid black line represents the temperature profile obtained from the numerical model described in section 3.3. The radiation correction resulted in the difference between the coated and uncoated probes to decrease from 188 K to 150 K. This difference can be entirely attributed to the catalytic effects on the probe surface and is sufficient for the uncoated thermocouple measurement to clearly overestimate the flame temperature.

The radiation-corrected data from the coated thermocouple measurement is compared in figure 6.14 to both the numerical results and the prediction of the simplified model presented in section 3.1.2, with the three datasets showing remarkable agreement, within 50 K. The maximum flame temperature reached in the theoretical profile was determined following the procedure described in section 3.1.3. The small difference in the experimental data on the cold advected side of the burner can simply be explained by the boundary conditions used for the theoretical and numerical models. The value of 500 K used in the models is representative of a large range of flames while the specific experimental data plotted in this figure has an injection temperature at the advected end of 460 K.

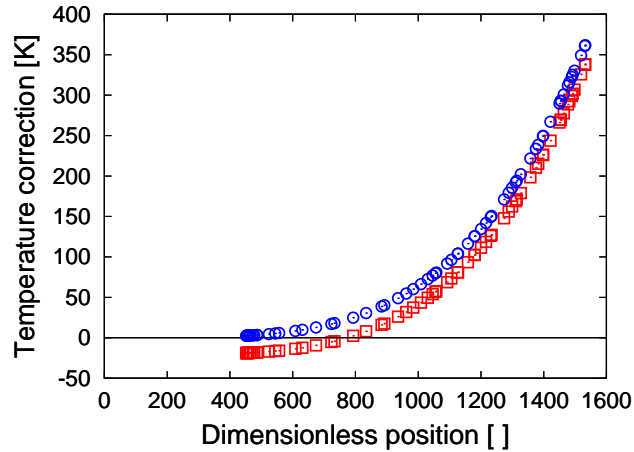


Figure 6.12: Magnitude of the radiation correction for a coated probe as a function of measured temperature, by neglecting the radiation received by the probe from the walls (\circ) and by assuming a representative wall temperature of 500 °C (\square).

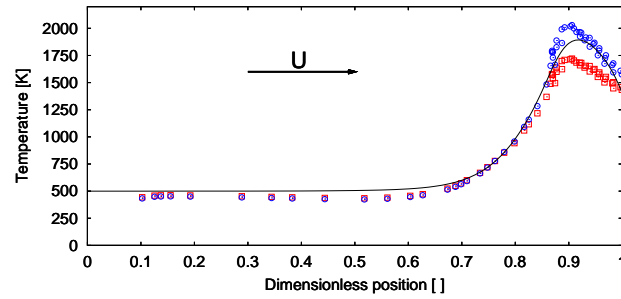
6.3.1 Temperature in the burning chamber

From the shape of the flame presented in figure 6.1, it seems obvious that the flame intensity and therefore its temperature is not uniform over the burner cross section. To measure this temperature variation, a coated thermocouple probe was successively introduced in the burning chamber through different extraction tubes. The resulting transverse temperature profile is presented in figure 6.15. The effect of the walls induces a significant reduction of the flame temperature on the periphery of the burning chamber, in excess of 350 K. In this figure, the solid and dashed lines represent the adiabatic flame temperature and the result of the numerical model, respectively.

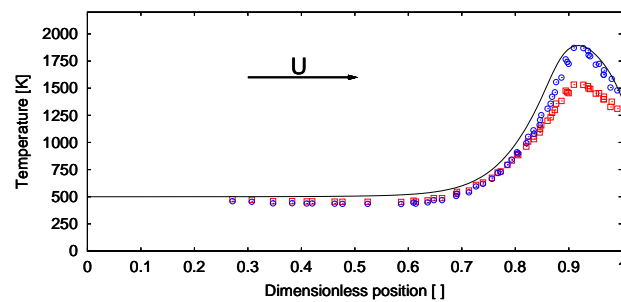
The use of the quartz cylinder described in section 4.1.2 allows the inner flame where the measurements are conducted to be much closer to isothermal. The position of the cylinder is illustrated in the figure by the vertical lines. Within this region, the flame temperature deviates no more than 125 K from either the adiabatic flame temperature or the flame temperature obtained numerically. Heat loss only account for part of the deviation since, as will be discussed in the next section, inhomogeneities in the species distribution results in a reduced mixture strength on the burner edges.

6.4 Species measurements

The measurement of mixture composition in the burning chamber was done using mass spectrometry, with the equipments and procedures described in chapter 5. This technique was employed throughout this thesis to establish the effective boundary conditions at the counter-diffusing inlet of the burner. It was also used to characterize the species distribution in the burner and the flames generated. These results are presented in this section.



(a)



(b)

Figure 6.13: Radiation corrected longitudinal temperature profiles (\circ) and untreated measured temperatures (\square). a) Using uncoated thermocouple probes; b) Using coated thermocouple probe. The solid black line is the profile obtained from the numerical model. The catalytic effects on the uncoated thermocouple surface result in an overestimation of the flame temperature.

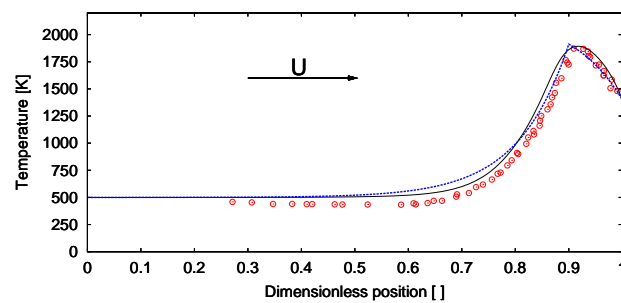


Figure 6.14: Comparison between experimental (\circ), numerical ($—$) and theoretical ($---$) longitudinal temperature profiles. The experimental values are slightly shifted to the left as a result of the small conduction losses in the probe assembly.

6.4.1 Species transverse concentration profiles

In the previous two sections it was shown that the temperature and velocity boundary layers in the burning chamber and chimney are significant issues in the burner design

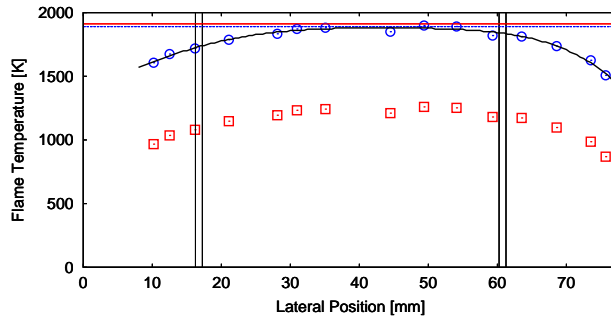


Figure 6.15: Flame temperature distribution across the burning chamber. The vertical lines represent the position of the walls of the inner quartz cylinder. The measurements were made with coated thermocouples, \square uncorrected temperatures, \circ radiation corrected temperatures. The solid and dashed lines represent the adiabatic flame temperature and the result of the numerical model, respectively.

used here. From these findings it appears obvious that the injection layer would be subjected to slightly different conditions across the injection array. By introducing the mass spectrometer capillary through successive extraction needles, it was possible to characterize the species distribution in the injection layer and define the variation of the boundary conditions at the counter-diffusing end. The results presented in figure 6.16(a) and 6.16(b), covering one half of the burner cross section, show the variation of the oxidant volume fraction and the corresponding change in mixture strength, respectively. Once again, the vertical lines represent the position of the inner quartz cylinder. Within this inner region of the flame, the mixture strength was measured to be uniform within 10% of its average values. On the edges of the burning chamber, the phenomena listed above result in the flame having a mixture strength over 50% lower. This considerably leaner periphery flame is colder and reaches instability well before the central region, often becoming extinct as the instabilities are still studied within the quartz cylinder.

This variation in the mixture strength ϕ measured in figure 6.16(b) is believed to be the main cause of the rapid cell motion observed in the cellular flames developing in the Mark I version of the burner, shown in figure 4.3. Rather than being caused by heat loss at the chamber windows, as was initially believed, the heat loss in the chimney is expected to play a central role in the phenomenon. The walls of the chimney being colder, the exit velocity of the species injected through the needles is higher in the periphery rows of the array. Additionally, the upward velocity is slower there because of the boundary layer developing in the burning chamber. The result from the combination of these effects is a higher concentration of the counter-diffusive species close to the chamber walls. This ϕ variation induces flame curvature and associated flame stretch that is responsible for the cell motion.

The introduction of the inner quartz cylinder in the burning chamber, as described in section 4.1.2 only addresses one of these problems, since velocity boundary layers are still present within the cylinder. However, the good flame flatness (see section 6.1) and absence of cell motion (see section 7.3) observed within the cylinder reveal that the influence of the velocity boundary layer is small. Solving the problem of the curvature of the flame edges and residual stretch would require the homogenization

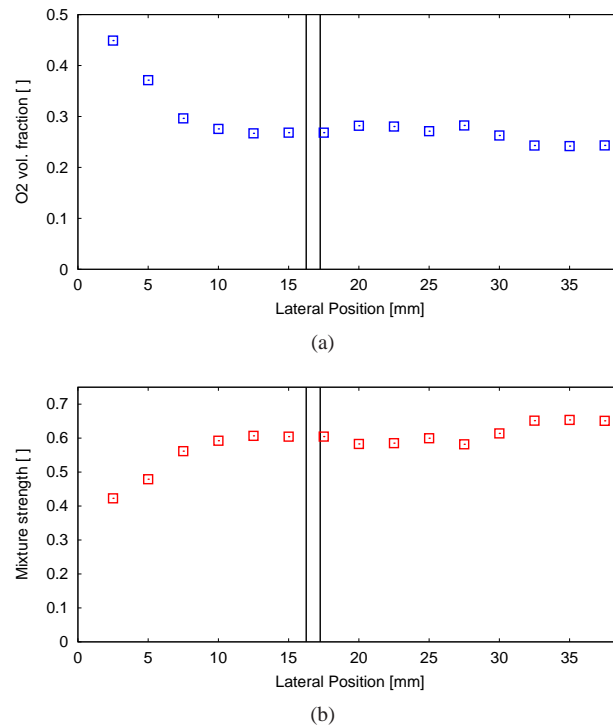


Figure 6.16: Effect of the walls on the oxidant distribution in the chamber, over one half of the burner cross section. (a) Variation of the O₂ volume fraction. (b) Corresponding change in the mixture strength. The vertical lines represent the position of the inner quartz cylinder.

of the temperature distribution in the burner chimney. Placing the whole assembly in an oven set at a temperature close to that of the exhaust would help but complicate optical access to the burning chamber. Localized heating on the chimney is another option but would require the presence of a heat conductive fluid, perhaps circulated, in the space between the injection and extraction arrays to ensure sufficient heat transfer. Some experimentations were made following this concept, with the very limited beneficial effect not outweighing the considerable increase in system complexity. In the end, since improvements provided by simply using a quartz cylinder to isolate the unstretched central region of the burner proved sufficient to allow the observation of stationary cellular flames, only this solution was implemented. This choice explains the significant increase in the area of the burner cross-section between the Mark I and the Mark II, to ensure that the inner unstretched region was large enough to conduct meaningful experiments.

6.4.2 Species longitudinal concentration profiles

Species concentration profiles covering the length of the burning chamber were also obtained by slowly moving the tip of the mass spectrometer capillary from the outside with a stable flame burning in the chamber. The procedure is described in chapter 5 and

is only able to measure stable species, with an estimated relative accuracy of about 5% for most of the mixtures measured. Close to the flame sheet, the large concentration of radical species can result in additional errors of up to 10%.

The profiles presented in figure 6.17(a) and 6.17(b) cover the cases where the fuel is advected and counter-diffusing, respectively. The concentration of the fuel (H_2), oxidant (O_2) and product (H_2O) are included. The profiles expected from the simplified theoretical model presented in section 3.1 are also plotted using solid lines. There is a surprisingly good agreement between the experiment and the simplified model, considering the drastic assumptions that were made in developing it, especially regarding the constant transport properties. These being evaluated at the flame temperature, it is without surprise that the main disagreement between the two are found in the cold region close to the advected species inlet.

The results obtained from the numerical model are also plotted in figure 6.17(a), using dashed lines. The agreement with the experimental data on the side where the fuel is advected is not very good, which is surprising considering that the model accounts for the variation of the transport properties with temperature. However, as seen previously, the model properly accounts for the flame position and the temperature profile. In the fuel counter-diffusing configuration, the numerical model failed to converge to a stable burning state. The reason for these errors is unknown, but since the numerical treatment of the problem is not the main concern of this thesis, this topic was not investigated further.

6.5 Flame position

To measure the flame location in the burner, photographs were taken from the side, following the procedure described in section 4.2.1. The images were then analyzed and the flame position determined as the point of maximum luminosity in the center of the chamber. This optically determined flame location was verified to be in excellent agreement with the location of the water concentration and temperature maxima. For the sake of simplicity, the optical method was used for all of the results presented here.

6.5.1 Virtual origin

The procedure used to determine the boundary condition at the counter-diffusing end of the burner is illustrated in figure 6.18. For each experimental condition, the mixture composition immediately next to the injection needle array supplying the counter-diffusing species was measured by mass spectrometry. These local concentration profiles (shown in the insert of figure 6.18, about 5 to 10 mm long), extending from the injection tube tips to the flame, allowed the determination of the amount of counter-diffusing reactant swept into the exhaust by the bulk flow, and hence the effective mixture strength in the burner. Based on this concentration profile, a point beyond the injection layer was chosen as the *virtual origin* of the counter-diffusing reactant.

The use of this short profile instead of a single point allowed some latitude in choosing the reference point to generate large datasets with more or less constant mixture strength. For instance, when increasing the bulk velocity the injection layer thickness decreased even if all other parameters remain constant. Accordingly, the oxygen concentration at a reference point 3.5 mm below the array decreased. This resulted in the mixture strength measured at that reference point to increase. To be able to use these two data points to measure the influence of bulk velocity on flame position, a new

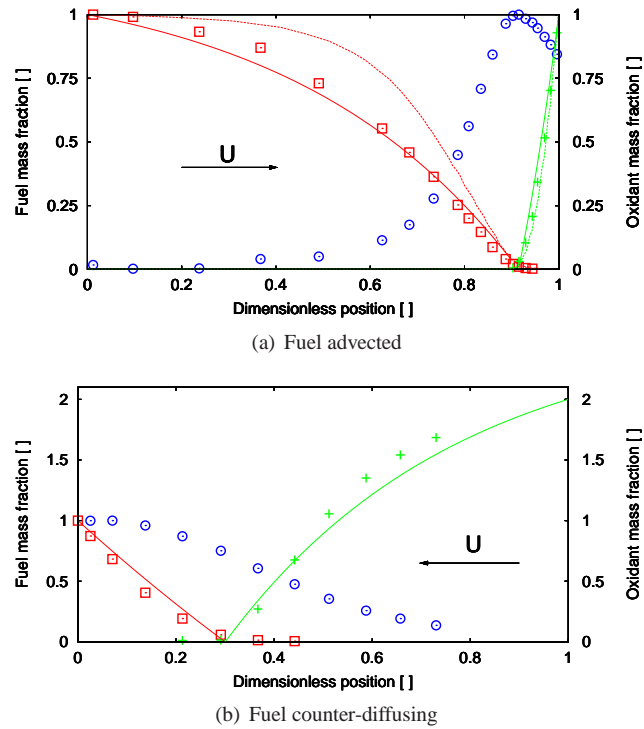


Figure 6.17: Longitudinal species concentration profiles, fuel (\square), oxidant ($+$) and water (\circ). The solid and dashed lines are the profiles obtained from the simplified theory and numerical models, respectively.

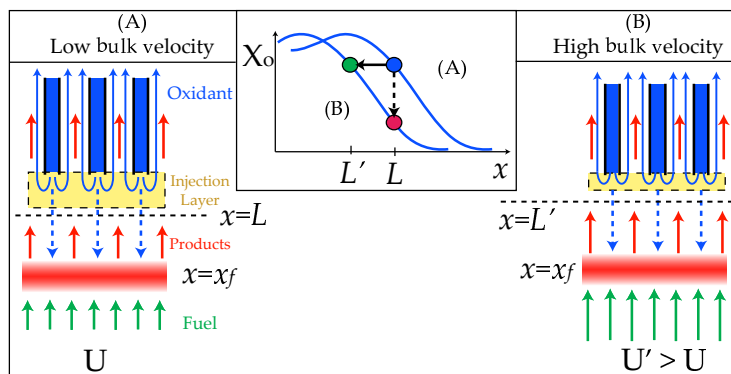


Figure 6.18: Sketch illustrating the technique used to set the virtual origin of the system. The short profile of counter-diffusing species concentration taken below the injection array (shown in the insert) allow the choice of reference points with the same mixture strength despite different injection layers.

reference point was chosen slightly downstream from the first one, where the oxidant

concentration was the same as in the first case. The result is that for the two data points the chamber length is slightly different and this was accounted for in the normalization process.

In the measurements presented here, the change in the virtual position associated with a change in bulk flow velocity was relatively small, on the order of 1 to 2 mm at the maximum. The minimum distance between the virtual origin and the needle array was always chosen to ensure that the reference point was outside of the injection layer. Following the measurements presented in section 6.2.1, this distance was set at 2.5 mm. The use of a two gas mixture (helium and CO₂) allowed the investigation of the effect of the Lewis number on flame position. Change in the inert composition and therefore in the advected mixture density, caused an effect of larger magnitude on the mixture strength than the one described previously for the bulk velocity. As can be seen in figure 6.19, when the inert gas was progressively changed from pure CO₂ to pure He at constant bulk velocity, the virtual origin had to be changed by about 3 to 7 mm to maintain a constant mixture strength.

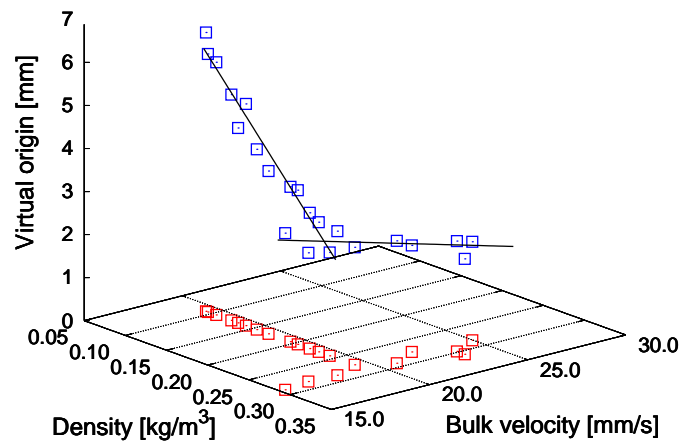


Figure 6.19: Effect of bulk velocity and mixture density on the virtual origin used to achieve a constant mixture strength of $\phi = 0.5$.

The displacement of the virtual origin proved a suitable technique to account for both of the effect of the bulk velocity and advected mixture density on the effective mixture strength. The mixture composition and temperature at the reference point were then used as boundary condition and the reduced chamber length as the new reference length for the comparison with the simplified model of section 3.1. This procedure allowed the effective mixture strength ϕ to be kept constant, despite the varying loss of counter-diffusing species into the exhaust at different bulk flow velocities and inert composition. To evaluate the theoretical flame position, the experimental Lewis numbers of the reactants were evaluated using the mixture composition and temperature measured at the flame. The dimensional bulk velocity was determined from the supplied mass flow rate.

6.5.2 Influence of bulk velocity

The position of the flame inside the burning chamber as a function of the bulk velocity magnitude and direction was investigated using CO₂ diluted H₂-O₂ flames. The results are presented in figure 6.20(a) and 6.20(b) for the fuel advected and fuel counter-diffusing configurations, respectively. Because of the limits imposed by the counter-diffusing species injection scheme, it was impossible to obtain data with the same mixture strength for both the fuel advected and fuel counter-diffusing configurations. When the fuel is counter-diffusing, most of it is carried away in the exhaust by the comparatively heavier inert. Accordingly, the flames produced in this configuration are always very lean. Typical results are presented in figure 6.20(b) for $\phi = 0.33$ and $\phi = 0.25$.

The thermal diffusivity D_{th} , used to determine the dimensionless bulk velocity was evaluated at three different temperatures for comparison purposes: at both inlet temperatures and at the flame temperature measured or as determined either numerically or using the method described in section 3.1.3. The result presented in figure 6.20 clearly show that the flame temperature is the most appropriate to evaluate D_{th} used in the dimensionless bulk velocity. When this reference point is used, the results show good agreement between the simplified theory for the flame position (equation 3.14) and the experimental results. The figures also show that the flame position is more accurately predicted by the simplified theory when the oxygen rather than the hydrogen is counter-diffusing.

Several factors can be invoked to explain the differences between the two data sets. The assumption of constant transport properties made in the theoretical development is not equally drastic in both configurations. Equation (3.14) reveals that the flame position is mainly determined by the Lewis number of the counter-diffusing species. In this dataset, Le_o varied only slightly from the injection point to the flame sheet (from 0.861 to 0.865) when the oxidant was counter diffusing. When the fuel was counter-diffusing, the Le_f variation was more significant, between 0.25 at the injection and 0.22 at the flame, on average. In addition, the thermal expansion, also neglected in the simplified theory, decreases the transport of the counter-diffusing species to the reaction zone. This effect increases the effective ϕ when the oxidant is counter-diffusing and decreases it in the reverse configuration (note that a decreasing ϕ lowers the curve $x_f(U)$ in figures 6.20(a) and 6.20(b)).

6.5.3 Influence of Lewis number

From the simplified theory described in section 3.1, when the velocity is high, only the Lewis number of the counter-diffusing species is expected to have a significant effect on flame position. However, when the velocity is small, both Lewis number need to be considered because the forward diffusion of the advected species becomes significant. To test this theory, the reactants were diluted in a mixture of two inerts (helium and CO₂) to generate a range of Lewis numbers for the two reactants. In these results the fuel-advected configuration was used and accordingly the Lewis number of the oxidant (Le_o) is expected to have a dominating influence on the flame position. Assuming a constant Le_f , the expected flame position dependence on Le_o and U is given in figure 6.21(a).

The use of helium as a dilution gas with its high thermal diffusivity means that the dimensionless velocity is relatively small, so the Lewis number of the advected species has to be taken into account. In figure 6.21(b), the flame position predicted by the theory is showed with and without considering the variation in the advected species

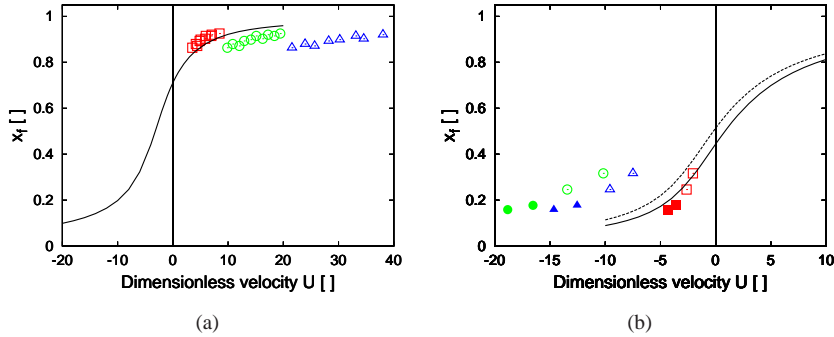


Figure 6.20: Effect of bulk flow velocity on flame position for the case of counter-diffusing oxidant (a) and counter-diffusing fuel (b). The D_{th} used to non-dimensionalize the bulk velocity is evaluated at the flame (\square), at the advecting inlet (\circ) and at the counter-diffusing inlet (\triangle). The lines represent the flame position predicted by the simplified theory, a) —, for $\phi = 1$, $Le_f = 0.35$ and $Le_o = 0.85$, b) $Le_f = 0.25$, $Le_o = 0.80$, $\phi = 0.25$ (filled symbols and solid line) and $\phi = 0.33$ (open symbols and dashed theoretical line).

Lewis number. For the low-velocity flames considered here ($0.4 > U > 2$), neglecting the advected species Lewis number results in differences of up to 12% in the predicted dimensionless flame position.

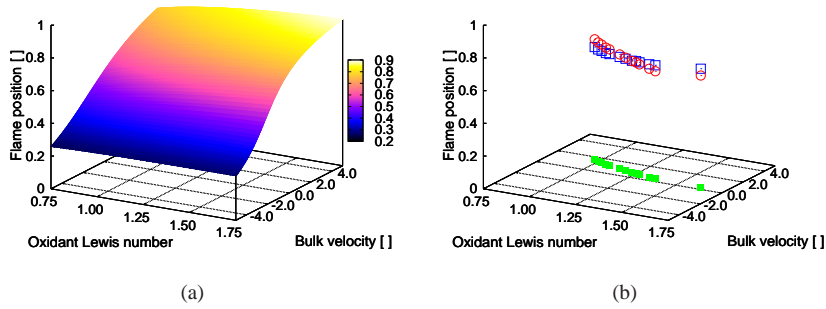


Figure 6.21: Effect of bulk velocity and counter-diffusing species Lewis number (Le_o) on flame position predicted by the simplified theory. a) The fuel Lewis number is assumed constant and the mixture strength is $\phi = 0.5$. b) Theoretical results, with (\circ) and without (\square) considering the variation of Le_f measured for the experimental data points available.

The results gathered in these conditions and presented in figure 6.22 confirm the necessity of considering both Lewis numbers. In figure 6.22(a), the measured flame position from the virtual origin is simply normalized using the reduced chamber length¹. A comparison between these results and the theoretically predicted values, even considering the variation of both Lewis numbers, yields considerable errors. For the data

¹The reduced chamber length is the total chamber length minus the position of the virtual origin used.

presented in figure 6.22(a), the error exceeds 20% for the flames with the lowest bulk flows.

This discrepancy can be explained by considering that for the low velocities used for this experiment, the conditions present at the end of the bottom injection tubes are not the same as in the prescribed gas stream. With the small chamber length² used here (20 mm), the bottom injection array is located in a region with significant concentration gradients. This results in a forward diffusion effect in the injection tube and in the effective chamber length being longer than expected. For the experiment presented here, when the inert gas is mostly helium, the fuel exits the needles only 10 mm from the flame and easily diffuses towards it, resulting in a concentration gradient within the injection needles. The consequence is that the effective chamber length is longer than the distance between the tip of the two needle arrays. This was confirmed by mass spectrometry measurements carried out throughout the burning chamber and *inside* the advected species injection tubes. Naturally, this effect will vary significantly with the burner operating condition, much like the position of the virtual origin described in section 6.5.1. From the mass spectrometric measurements, it was estimated that this effect resulted in an chamber length increase of 5 mm on average for the conditions used in this section. The results using this corrected chamber length for the normalization of the flame position are presented in figure 6.22(b), resulting in much better agreement with the theoretical predictions (differences below 5%).

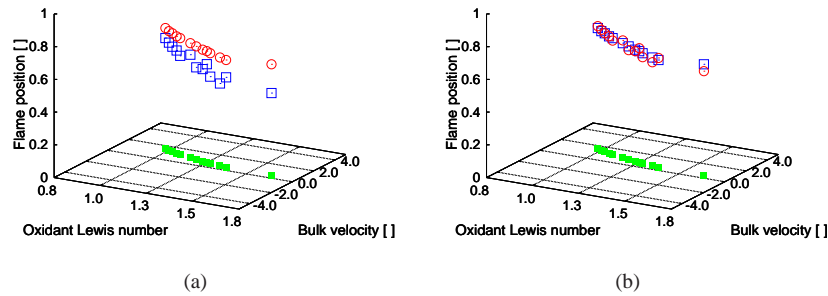


Figure 6.22: Experimental results for flame position with variable Lewis numbers. a) Comparison with simplified theory. b) Comparison with theory using an effective chamber length slightly longer than the actual chamber length, to compensate for diffusion effects in the advected supply at low velocity. With (□) experimental measurements and (○) theoretical results.

²The small chamber length of 20 mm used in this section, compared to the 40 mm used in section 6.5.2 was chosen to prevent the formation of convective cells in the burner (see section 6.1.2).

Chapter 7

Experimental observation of thermal-diffusive instabilities

In this chapter, the experimental observation of thermal-diffusive instabilities realized in the unstrained diffusion flames characterized in the previous chapter are presented and analyzed. In the first section, the limits of stability and extinction of the flame are presented as a function of the burner operating parameters. In the second section, the type of instability occurring close to the lean extinction limit is identified in the Lewis number parameter space. The subsequent sections are dedicated to the two types of thermal-diffusive instabilities observed in this experiment: cellular flames and planar intensity pulsations.

7.1 Stability and extinction limits

In section 3.2 it was shown that the limit of infinitely fast and complete combustion (the Burke-Schumann limit, corresponding to $Da \rightarrow \infty$) is unconditionally stable. The experimental results on instabilities presented in this chapter are all gathered by starting from such a stable baseline flame. This flame is described by the theoretical model of section 3.1 and has been extensively characterized in chapter 6. In order to observe thermal-diffusive instabilities, it is therefore necessary to decrease the Damköhler number Da until a marginally stable state is achieved. When Da is further decreased, the unstable flame can remain burning for a certain range of Da before reaching extinction. This sequence of events follows the top branch of the S-shaped response curve of figure 3.3.

In numerical treatments of the problem such as the one by Metzener and Matalon [45], it is convenient to control the Damköhler number simply by changing the bulk velocity U while keeping all other parameters constant. Unfortunately this is not possible experimentally using the present configuration because of the strong coupling between U and other important parameters such as the boundary condition at the side of the chamber with the counter-diffusing reactant. As a result, only a narrow range of velocities can be used while maintaining a configuration similar to the idealized model of figure 3.1. If the bulk flow is too fast, the flame will be located in the injection layer and if it is too low the flame sheet is far from the injection array as to be subjected to buoyancy induced instabilities (see section 6.1.2). Although it should be possible to generate flames with a very small bulk flow using this configuration, experimentally the

task has proved extremely difficult. As the bulk flow magnitude is decreased, the flame has a tendency to collapse entirely or partially onto one of the injection arrays. As a result of the subsequent asymmetric heating of the supply tubes causing convection within the burner, it was almost impossible to re-create a stable planar flame sheet in the center of the burner without extinguishing and re-igniting the burner. Consequently, the conveniently usable bulk velocities available in the burner ranges only from about 15 to 30 mm/s. This range is insufficient to change the Damköhler number enough to bring the flame from stability down to extinction.

For the burner design used, the only other experimentally available mean to control the Damköhler number is through the flame temperature that can be varied either through the dilution (its nature or its amount) or the mixture strength. Changing the burning temperature through dilution alone while maintaining constant mixture strength is very complicated because, similarly to the bulk flow magnitude, the nature of the inert has a strong influence on the injection layer (see figure 6.19). Therefore, the Damköhler number was reduced and the flame brought to instability simply by reducing the mixture strength through the supplied fuel volume fraction. The following procedure was used to map the burning regime sustained in the burner, under constant bulk velocity, as a function of the supplied mixture composition. Starting from a stable flame, the strength (fuel fraction) of the fuel stream was progressively reduced while keeping all other parameters constant. The flame shape and position in the burner is monitored simultaneously using two cameras, as described in section 4.2.1. Prior to the implementation of the mass spectrometric measurements, the results could only be plotted as a function of the reactant composition of each stream supplied to the burner. Such results for the fuel advected case are presented in figure 7.1.

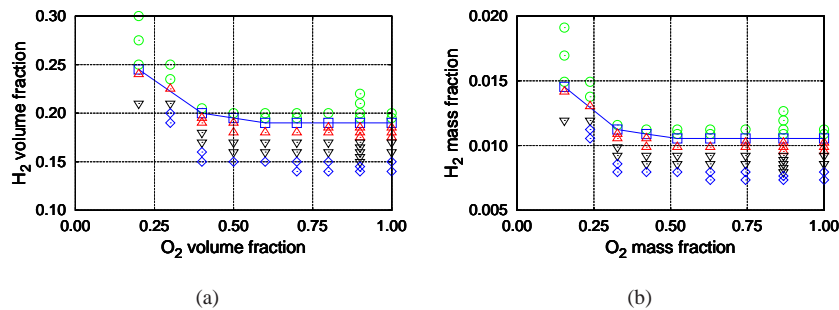


Figure 7.1: Stability limits inferred from the supplied flow rates, corresponding to flame #2 in table 6.1 ($U = 19.4$ mm/s). a) As a function of the volume fraction of the reactants. b) As a function of the mass fractions. Key: (◊) Stable planar flames; (◻) Onset of first holes in flame sheet; (◄) Partly cellular flames; (◃) Fully cellular flames; (◊) Fully cellular flame collapsed on injection array.

It was observed that the flame does not become cellular instantaneously as a whole but is rather observed to first become partly cellular and later fully cellular as the input mixture composition is changed. This was expected from the measurements of the species distribution over the burner cross section presented in figure 6.16. The 10% variation in ϕ observed in the central part of the burner results in part of the flame reaching instability before the rest. In figure 7.1, the operating parameters resulting in a partially and a fully cellular flame have been identified separately. These measurements

were made using the conditions listed under flame #2 in table 6.1 as the baseline state (varying only the fuel and oxidant content in their respective streams).

The concept of extinction is also somewhat blurred in this configuration since the flame does not stop burning completely until very low fuel volume fractions are reached, on the order of 8-10%. What happens is that, as the flame approaches extinction and fuel leakage through the reaction zone increases, the flame front moves in the direction of the flow. At some point the flame *jumps* into the highly oxygenated region of the injection layer where it can continue burning despite further reduction in mixture strength. The criteria for flame extinction used in this thesis is therefore one of flame position rather than one of flame aspect¹. The flame was considered unusable for measurements if it was located very close or downstream of the virtual origin considered for the definition of ϕ . While the flame might actually still burn, in the corresponding situation for the idealized one-dimensional burner of figure 3.1 it would have been blown out into the top stream.

Because of the nature of injection layer already abundantly discussed in this thesis, the results presented in figure 7.1 are only qualitative. The use of mass spectrometry allows the generation of more reliable stability and extinction limits as a function of the effective counter-diffusing boundary conditions of the burner. The results presented of figure 7.1 are plotted in this manner in figure 7.2. The comparison between the two figures reveals the necessity of such mixture composition measurements to define the true operating parameters of the burner. This dataset was obtained using a fixed virtual origin 2.75 mm below the injection array and demonstrate that the effective oxidant volume fraction at the virtual origin is about 1/3 of the value in the supplied gas stream.

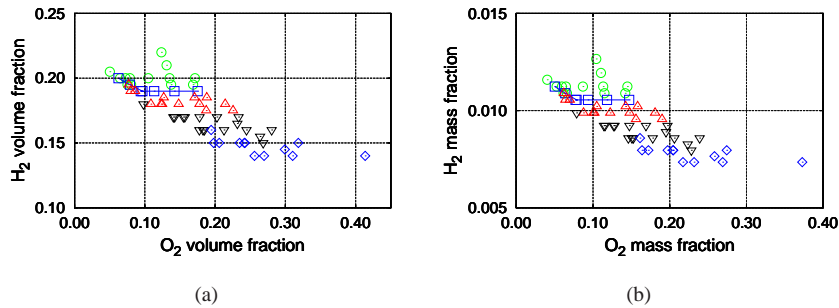


Figure 7.2: Stability limits inferred from the mass spectrometric data, as a function of the volume (a) and mass (b) fractions of the reactants at either end of the burning chamber. The burner is operated in the fuel-advecting configuration and the symbols are the same as in figure 7.1.

From the measurements used to generate the maps given in figures 7.1 and 7.2, the variation of the *effective* mixture strength can also be determined as the flame becomes unstable and leakage becomes significant. Again the mass spectrometric data are essential to identify the true flame parameters. This is especially true for rich flames when the counter-diffusing stream has a low oxygen content. In this situation, the strong effect of the bulk flow on the injection layer results in a five fold difference between the

¹Using the same burner configuration as here, Lo Jacono[55] defined in his thesis the extinction as a state when the flame occupied only 0.2% of the burner cross section. From the measurements presented here, this limit occurs long after the flame is displaced to the tip of the injection needles

mixture strengths as determined from the supplied mixtures and by mass spectrometry.

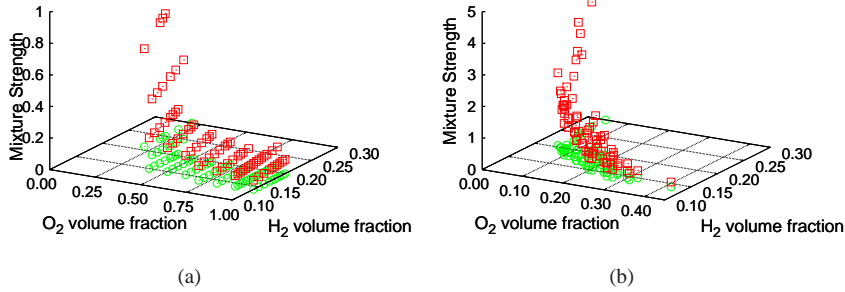


Figure 7.3: Mixture strength (\square) inferred from flow rates (a) and mass spectrometry (b). The circles (\circ) represents the projection of the data points in the mixture composition plane.

Through the variation of the mixture strength, as the fuel content of the advected stream is varied and the flame becomes unstable, it also changes position. The observed flame position corresponding to the different stable and unstable flames plotted in figure 7.2 are given in figure 7.4(a). A more detailed view is presented in figure 7.4(b) where the flame position of two flames is shown as the mixture strength is progressively lowered. As expected, when the flame is stable or partly cellular ($\phi > 0.6$), a decrease in the advected fuel mixture volume fraction results in the flame moving upstream. However, when the flame becomes fully cellular ($\phi \approx 0.5$) the trend is reversed and the flame moves towards the oxidant end of the burner as the mixture strength is further decreased. The phenomenon is most likely strongly influenced by the significant reactant leakage through the reaction zone implying some degree of pre-mixing in the resulting cellular flames. When the mixture strength is reduced significantly below the value corresponding to full cellularity, the position of the flames moves upstream of the virtual origin. This corresponds to negative values in figure 7.4(b). As mentioned above, under these conditions the flame was considered unusable because located in the injection layer and no longer strictly one-dimensional.

7.2 Mapping of the instabilities

The theoretical investigations of the thermal-diffusive instabilities of diffusion flames presented in chapter 2 predict that the type of instability that develops close to extinction, if any, will depend on the transport properties of the reactants. The Lewis numbers of both reactants play a defining role in the phenomena as they relate the rates at which the reactants can be supplied and the heat evacuated from the reaction zone. The combination of possible Lewis numbers constitutes the parameter space that should be explored to validate the theoretical predictions on the nature of the thermal-diffusive instabilities in diffusion flames.

Numerical treatment of the linear stability problem allows both Lewis number to be controlled independently and the whole parameter space to be investigated. The result are maps such as the one presented in figure 2.1 where the type of instability is predicted as a function of both Lewis number. However, experimentally the situation

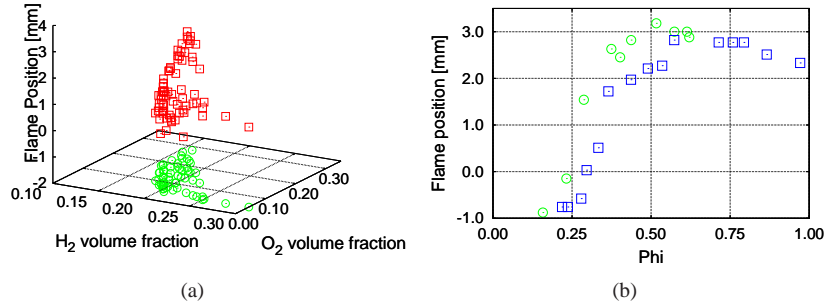


Figure 7.4: Flame position change as the mixture strength is lowered and the flame becomes unstable. For two initially stable flames, using 100% (\square) and 90% (\circ) oxygen in the counter-diffusing stream. Negative values mean that the flame is located above the virtual origin and in the injection layer.

is different since the two Lewis numbers are not independent and cannot be chosen arbitrarily. Only a limited set can be produced as a result of the reactants and inert gases available for this type of study. The hydrogen-oxygen combination was selected as the main reactive system because of its simplicity and the extensive experience of our laboratory with this type of diffusion flames. The simplicity of the reaction, yielding only water as a product, also eases the mass spectrometric analysis of the mixture composition in the burner. Since H₂-O₂ flames produce very little visible light emissions, the inert has to be chosen appropriately to solve this problem. Carbon dioxide (CO₂) fits this requirement and was used extensively in this thesis as the inert gas. Additionally it is cheap, non-toxic and relatively stable at high temperature.

Hydrogen-oxygen diffusion flames diluted in various amounts of CO₂ yield only relatively small variations of the Lewis number of both species. For instance, measurements made in the Mark I version of the burner[96] with such mixtures only allowed Le_f to vary between 0.23 and 0.27. The results collapse almost to a single point in the Lewis number parameter space and are of limited use for the validation of the theoretical models. In order to produce wide ranges of Lewis numbers, a mixture of two inerts with drastically different transport properties can be used for the dilution of the reactants. For the results presented in this thesis, the second inert selected is helium. As this lighter inert progressively replaces CO₂ in the dilution mixture, the Lewis numbers of both reactants increases significantly. This allowed the investigation of part of the parameter space where planar intensity pulsation are expected.

However, as the helium replaces the CO₂, the flame becomes less luminous, to the point of making observation from its visible light emission impossible at high Lewis numbers. For this reason, a heavier fuel (methane CH₄), was used to explore the pulsation instability region of the parameter space, corresponding roughly to both Lewis numbers being above unity. CO₂ and helium were again used as the dilution mixture for the sake of simplicity and convenience in the mass spectrometer calibration. The combustion of methane producing CO₂ in addition to water, the use of two other inerts would have required a six gas calibration for the mass spectrometer, complicating the procedure described in section 5.4.2 beyond practical feasibility. The use of still heavier fuels and different inerts would allow the investigation of a larger part of the Lewis number parameter space at the cost of some complications of the experiment.

Examples of such combinations with an estimation of the parameter space covered are given in appendix B.

The measured region of the Lewis number parameter space covered by hydrogen and methane burning with oxygen in a mixture of CO_2 and He is given in figure 7.5(a) with the corresponding type of instability observed close to extinction. With hydrogen, cellular flames are observed when the inert used is comprised only of CO_2 . When helium almost entirely replaces CO_2 , oscillations were observed in the H_2 flames but were difficult to measure because of their very dim light emission. The methane flames produced were seen to oscillate for the whole range of helium- CO_2 inert mixtures used. However, when the inert is almost exclusively CO_2 , corresponding to the lowest Lewis numbers, the oscillation are of very low amplitude, even close to extinction. This hints at a possible transition towards another instability mode close to the limit of the Lewis number range achievable using this reactant and inert combination.

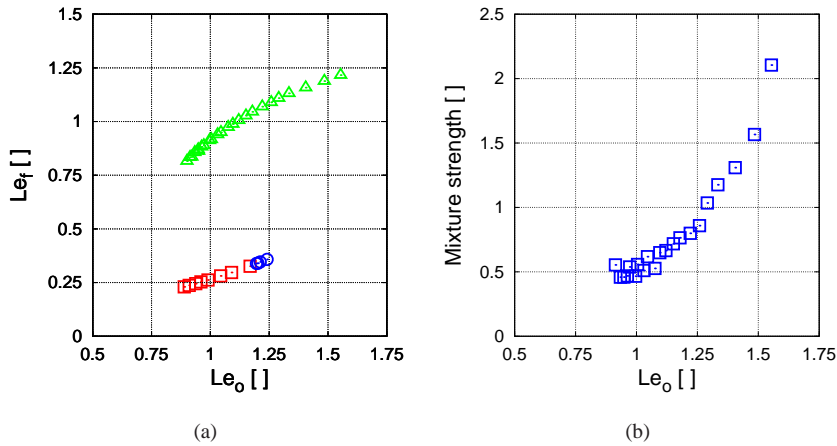


Figure 7.5: a) Experimental map of the instabilities in the Lewis number parameter space. With \square cellular hydrogen flames, \circ pulsating hydrogen flames and \triangle pulsating methane flames. The mixture strength is roughly 0.5 for cellular flames. b) Mixture strength variation associated with the change in inert composition for the pulsating methane flames.

The change in the inert composition used to achieve the wide range of Lewis numbers presented above obviously caused changes in the injection layer and therefore on the resulting mixture strength. The results presented in figure 7.5(b) quantify this change for pulsating methane flames.

7.3 Cellular flames

7.3.1 Observed instabilities

An example of the observed typical transitions starting from a stable flame sheet to a fully cellular flame as the mixture strength is progressively reduced is presented in figure 7.6. This sequence was captured inside a 48 mm inner diameter quartz cylinder place inside the burner. The outer flame in the rest of the burner has followed the

same transition, but with strong cell motion, and became extinct before the instabilities developed in the inner cylinder. The difference in the mixture strength between a stable and a fully cellular flame is quite high, about $\Delta\phi = 0.1$. This difference is mainly due to the change in the counter-diffusing boundary condition resulting from progressively reduced flame activity. This results in a reduction of the effective bulk velocity in the injection layer and an increase in the oxygen content at the top of the chamber, explaining the decrease of ϕ .

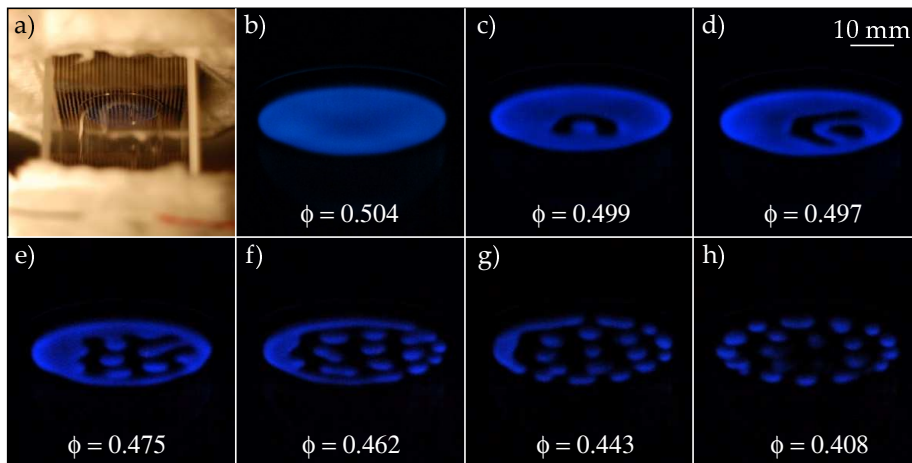


Figure 7.6: Photographs of cellular flame structures, from onset to full cellularity. For this sequence, the inert is pure CO_2 and the bulk velocity is kept constant at 19.4 mm/s. In these hydrogen flames, the Lewis numbers for the fuel and oxidant are approximately 0.23 and 0.86, respectively.

From the distribution of the oxidant across the burner cross section presented in section 6.4.1, the effective mixture strength is expected to be slightly higher in the central portion of the burner. Accordingly, the instabilities are expected to occur at the periphery of the flame first. They should then propagate inward as the mixture strength is reduced, however the opposite is observed. The residual flame stretch distribution in the burner can be invoked to understand this counter-intuitive finding. From the results presented in section 6.2.3, the residual stretch is expected to be higher on the periphery of the inner flame because of the velocity boundary layers. Since stretch is known to have a strong stabilizing influence on the thermal-diffusive instabilities, this can explain why the instabilities occur first in the richer but less stretched flame center.

One of the main problems in the Mark I version of the burner is that the residual flame stretch and species distribution inhomogeneities are high enough to induce strong cell motion in the unstable flames. This prevents the accurate measurements of the cellular flames geometrical characteristics since the cells produce streaks in the long exposure photographs required to capture their dim light emission. For example, the picture presented in figure 4.3 was taken using a 1/10 second exposure and is barely usable to determine the cell size. By comparison, the images taken in the Mark II version and used in the sequences of figure 7.7 are captured using 1/4 second exposure time. The absence of streaks behind the cells demonstrate that the true shape of the cells can be measured from these photographs.

The two sequences of figure 7.7 reveal the small cell motion that is still observed

in the Mark II burner for partially and fully cellular flames. The number and size of the cells is constant, but there is a very slow drift in the cells positions. There are also cells that divide and other cells that tend to absorb their neighbors. These phenomena can be clearly observed at top of the fully cellular flames, in frames f to j.

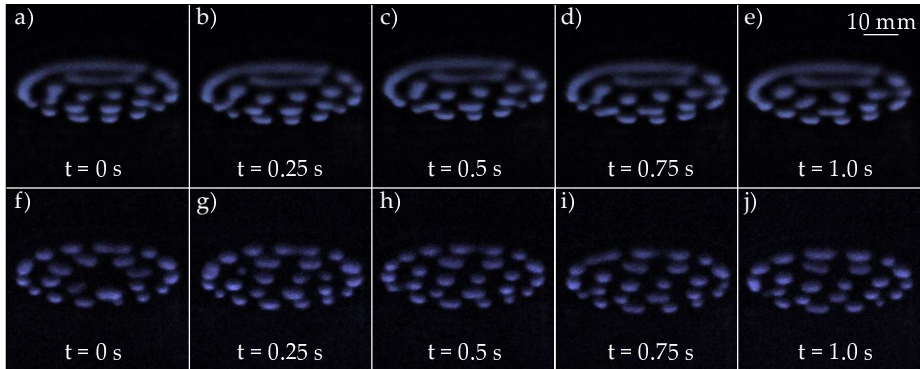


Figure 7.7: Cell motion in cellular flames for one partly cellular flame (first row, $\phi = 0.443$) and a fully cellular flame (second row, $\phi = 0.408$), corresponding to frames g and h in figure 7.6, respectively.

The concentration profiles of the reactants taken in the center of the burner, along its longitudinal axis, are presented in figure 7.8. These profiles were taken through a lean ($\phi = 0.5$) stable planar flame sheet, very close to the onset of the first cells. This figure can be compared to the profiles given in figure 6.17(a) for a similar flame but richer ($\phi = 1$) and hence further from the transition to instability. The main difference between the two sets of profiles is the reactant leakage through the reaction zone. In the flame close to the transition to instability, the leakage is significant while almost none was measured for the richer flame. This confirms the belief that through leakage the critically stable and cellular flames are at least partly premixed in nature.

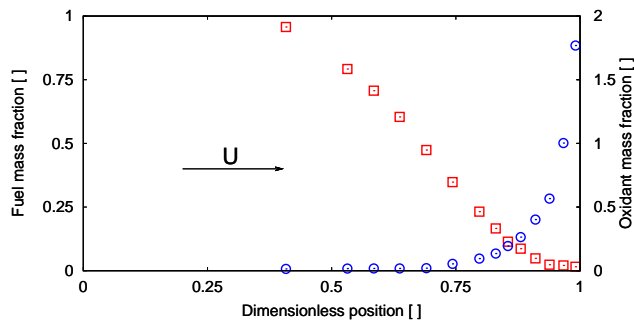


Figure 7.8: Reactant concentration profiles across a stable flame close to the transition to a cellular structure, corresponding to frame b) in figure 7.6. Significant fuel (\square) and oxidant (\odot) is seen across the still homogeneous reaction sheet.

7.3.2 Cell size scaling

From the theoretical modeling the size of the transverse cell spacing l_T in the cellular structure is expected to scale linearly with the diffusion length $l_D = D_{th}/U$ [44]. This quantity is defined as the ratio of the thermal diffusivity to the bulk flow velocity. The results of the linear stability analysis show that the wavelength with the maximum growth rate at marginal stability will be indicative of the cell size. The more general expression for the cell size is given in equation 7.1.

$$l_T \sim \frac{2\pi l_D}{\sigma^*} \quad (7.1)$$

In this equation, σ^* is the wavenumber at the onset of the instability. This parameter σ^* is obtained from the numerical treatment of the dispersion relation with its dependence on flame parameters such as Da , Le_o , Le_f , U and ϕ unknown. For stoichiometric flames with small Lewis numbers, σ^* has been shown to be roughly equal to 1 [45]. For the lean flames such as those were the cellular structure is observed in this burner ($\phi \approx 0.5$) the same reference evaluates σ^* again close to unity, but increasing slightly with Le_o . The dependence of σ^* on the other parameters is likely to be significant in the determination of the cell size, but specific numerical calculation would be required to enable direct comparison with the available experimental results. Accordingly, since it falls outside of the scope of this thesis, the dependence of l_T on σ^* will not be discussed further here.

To investigate the scaling of the cell size, the experiment was constructed to allow control over the two quantities defining the diffusion length l_D . The bulk velocity can be changed directly, and the resulting effect of the cellular flame structure can be seen in figure 7.9. These experiments were realized using hydrogen as the advected fuel and pure CO_2 as the inert. The cell size is clearly seen to increase as the bulk velocity is decreased, as expected. Under those conditions, when the bulk flow is lowered below about 18 mm/s the cellular pattern starts to rotate at about one revolution per second. From a stationary partly cellular flame, a small decrease in the mixture strength suddenly changes the flame structure to a fully cellular and rotating pattern. This change is associated with a sudden increase in the cell size and accordingly the results gathered with large cell size at low velocities are subject to greater uncertainty.

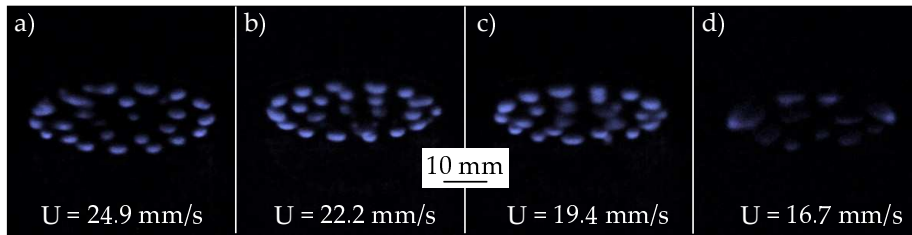


Figure 7.9: Pictures of cell size scaling with bulk velocity in the fuel-advected configuration, with pure CO_2 used for the inert. The mixture strength is $\phi = 0.45$ on average for these pictures.

The second parameter defining the diffusion length, the thermal diffusivity, was modified through the use of a two inert mixture as the dilution gas. The resulting change in the cellular pattern as the inert composition is progressively changed from

pure CO₂ to pure helium is given in figure 7.10(a). As expected, this increase in the thermal diffusivity results in an increase in the observed cell size. It should be noted here that the large size cells are observed to have small amplitude and unsteady size oscillations. In figure 7.10(b), the reactants transport properties in the cellular flames presented in figure 7.10(a) are plotted in the Lewis number parameter space. This reveals that the large size cells are produced very close to the transition where the dominant instability close to extinction is intensity pulsations rather than cells. It is expected to see competing modes of instability in this region of the parameter space [45]. In the transition region it was also possible to observe under certain conditions a rotating planar flame spiral inside the burner. This situation corresponds to a single cell in rotation with the observed angular velocity being again on the order of one revolution per second. Unfortunately the phenomenon was too weakly luminous to be further investigated using the experimental techniques available. All of the flames with varying bulk velocities realized in pure CO₂ inert presented in figure 7.9 correspond to a state very close to point a) in figure 7.10(b).

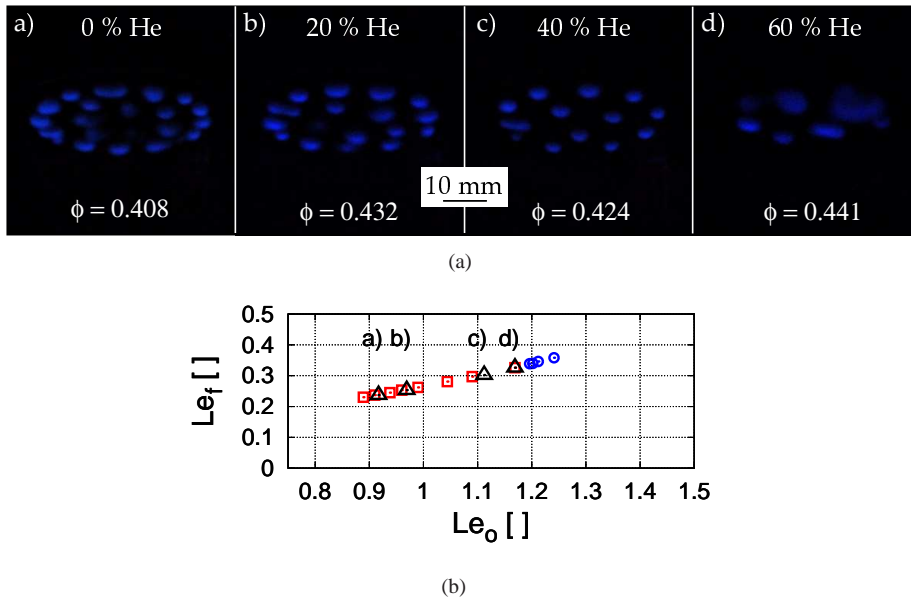


Figure 7.10: a) Images of cell size scaling in the fuel-advected configuration. b) Location in the Lewis number parameter space corresponding to the cellular flames shown in a) (Δ). The other data points represent conditions where cellular flames (□) and planar intensity pulsations (⊙) have been observed in hydrogen flames.

The cell sizes λ_c extracted from both datasets presented previously is plotted in figure 7.11 against the diffusion length calculated using the thermal diffusivity at the flame temperature. In this figure the expected linear scaling with thermal diffusivity is observed for both datasets, particularly for the one realized at constant velocity. This is consistent with the results of Metzener and Matalon [45] which suggest that the Lewis number dependence of σ^* is weak. Further knowledge regarding the velocity dependence of the parameter σ^* would be required to determine if the diffusion length alone is sufficient to account for the cell size dependence on bulk flow velocity.

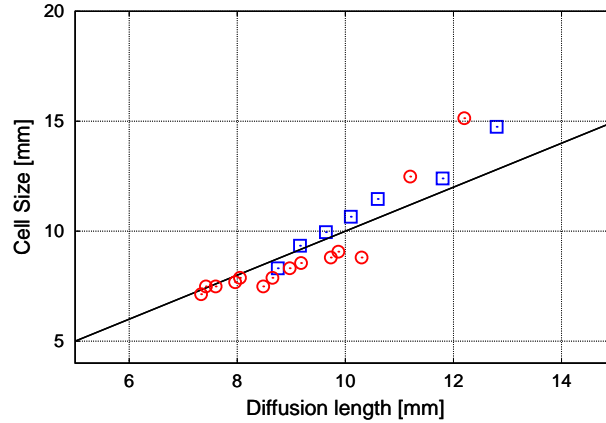


Figure 7.11: Scaling of the measured cell size λ_c as a function of the diffusion length, using the thermal diffusivity at the flame. The two datasets were realized at constant velocity, varying the inert composition (\square) or using CO_2 as the inert and changing the velocity (\circ).

Unfortunately the limited range of velocity under which stable cellular flame pattern are observable in the current burner configuration does not allow the matter to be investigated further. Attempts have been made to try to correlate λ_c/l_D with parameters that might help reduce the scatter observed in figure 7.11 such as Le_o , ϕ or U without discernible trends emerging. It was impossible to use the Damköhler in this situation since the fragmentation of the flame front in cellular flames prevents the gathering of reliable mass spectrometric data.

Changes in the mixture strength resulting from the use of different velocities and inerts can be estimated in manner similar to the one documented in section 6.5.1 for the virtual origin. Assuming a constant virtual origin position 3.0 mm below the injection array, the mixture strength variation resulting from the changes in velocity and inert composition applied in this section is presented in figure 7.12. For the range of inerts and velocities considered here, the mixture strength *before the onset of the instabilities* is $\phi = 0.5 \pm 0.2$.

7.4 Planar intensity pulsations

The results presented in the previous section reveal that as the reactant Lewis numbers are increased so does the size of the cells forming close to extinction. For very big cells, the pattern becomes less well defined and unsteady. In this section, flames with higher Lewis numbers are produced where planar intensity pulsations instead of a cellular pattern develops close to extinction. The video acquisition technique described in section 4.2.2 is used to capture the flame dynamics. It is operated between 50 (the lowest possible acquisition rate) and 250 frames per second (fps) to provide the bandwidth sufficient to properly resolve the pulsations. The analysis of the digital videos provides a 8bit signal of the intensity of the light emission of the chemical reaction. It is necessary to point out here that this signal is only an indirect measure of the chemical activity. A signal that falls to zero simply means that the flame does not emit enough

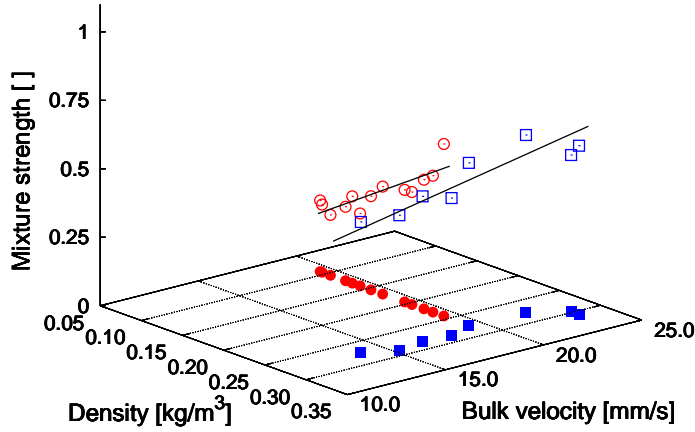


Figure 7.12: Effect of bulk velocity and mixture density on the mixture strength, considering a constant virtual origin 3.0 mm below the injection array. The open symbols have the same meaning as in figure 7.11 with the filled symbols being their projection in the density and bulk velocity plane.

light to be detected, not that it is extinct.

The technique therefore only provides a limited dynamic range for the flame intensity. The settings of the image acquisition had to be adjusted to ensure that the flame could be observed over the entire pulsation cycle and avoid pixel saturation. Therefore the exposure time and the aperture were changed between very dim and brighter flames. As a result, the absolute magnitude of the signal acquired and the pulsation amplitude cannot be directly compared between flames. However, the image sensor of the camera was used with a linear sensitivity setting ($\gamma = 1$) so the variation of the maximum flame light emission intensity relative to its average was considered the best measure of the pulsation amplitude available. This signal was acquired by considering a sampling window such as the one presented in figure 7.13. For each column of pixels in this window, the value and position of the intensity maximum is found. The width of the windows typically used includes from 10 to 20 columns, ensuring that the average values returned are not biased by optical artifacts and represent the true flame position and intensity. The procedure is repeated for each frame of a video sequence capturing several flame pulsation cycles. Typical sample lengths are between 10 and 20 seconds, comprising between 500 and 5000 frames, the longest requiring of the order of 2 minutes of processing time to extract the signals.

As was the case for the cellular flames of section 7.3, the instabilities investigated here occur close to extinction, meaning that the flames are very dim. The unsteady nature of the intensity pulsation also requires the use of short exposure times to capture the phenomena. To maximize the light gathering, the images are taken from the side, using viewing position # 1 in figure 4.9. Consequently, the signal available is a spatial integration over the width of the flame. Care has to be taken in the interpretation of the signal since the temporal oscillations of the flame also resulted in some spatial inhomogeneities. For instance, the appearance of traveling waves resulted in a large increase in the measured flame intensity when the wave passed on the camera side of

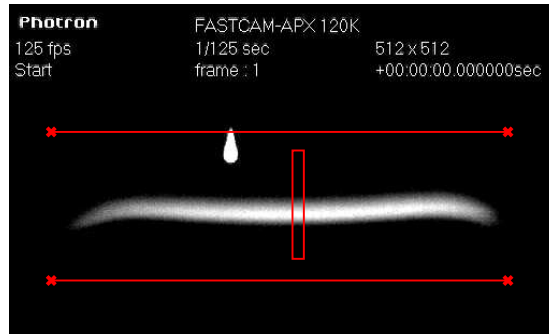


Figure 7.13: Example of sampling window used for the video analysis.

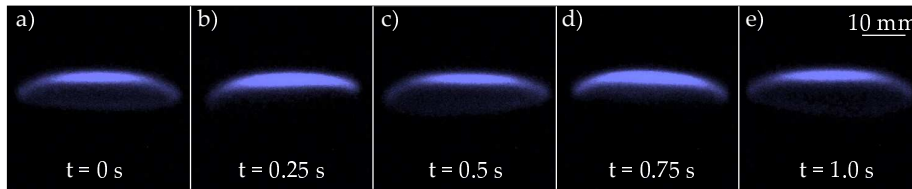


Figure 7.14: Intensity pulsation in a helium diluted hydrogen flame.

the burner. It is for this reason that the amplitude results presented in this section must be treated with caution and to have a relatively high uncertainty. The results on the pulsation frequency on the other hand were found to be unaffected by these traveling waves and are considered very reliable.

7.4.1 Observed instabilities

The first experimentations of pulsating planar flames were made using hydrogen as the fuel and mostly helium as the inert to provide sufficiently large Lewis numbers. Transition from cells to pulsations as the dominant mode of instability close to extinction was observed with flames created using the inner quartz cylinder in the burner. It was not possible to observe pulsating hydrogen flames in the absence of the inner quartz cylinder as extinction always occurred before the instability could develop. The limited light sensitivity of the high speed camera was insufficient to capture these very weakly luminous flames. The slowest acquisition rate of the device still imposes a relatively fast exposure time of 1/50 of a second. Using the Nikon D200 digital still camera, described in section 4.2.1, it was possible to take up to 24 frames in succession at approximately 4 frames per second. A sequence of a pulsating hydrogen flame acquired using this technique is presented in figure 7.14.

The observed pulsating hydrogen flames, such as the one presented in figure 7.14, are identified in the map of figure 7.5(a) and are associated with the highest achievable Lewis numbers using this fuel. Using the 4 sample per second signal extracted from these flame, the pulsation frequency was determined to be about 1.5 Hz. This is very close to the Nyquist frequency of such a signal and illustrates the difficulty of capturing the dynamics of these flames. In addition to these technical problems, hydrogen flames

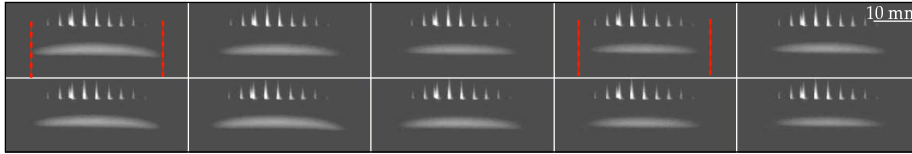


Figure 7.15: Pulsation in a methane flame with the inner quartz cylinder present. The time increment between the frames is 0.05 seconds and the frame width is equal to the quartz cylinder inner diameter. The vertical dashed line represent the maximum flame size, associated with the higher intensity part of the oscillation.

are not well suited to investigate the intensity pulsations because the transition between cellular flames and intensity pulsations occurred when about 80% of the inert was helium. This provides only a very limited range of Lewis number over which the phenomenon could be studied.

Methane (CH_4) is a much more appropriate fuel for the generation of pulsation instabilities in diffusion flames. Its higher mass results in significantly larger Lewis numbers when mixed with He-CO_2 , meaning that pulsations can be observed for a large range of inert composition. Additionally, CH_4 flames emit much more light than H_2 flames, allowing the use of higher acquisition rates. For these reasons, the results presented in the remainder of this chapter are obtained using exclusively methane flames. The list of the burner parameters of the various flames used to gather the pictures and signals presented in the following pages is given in table 7.1, at the end of the section.

In the sequence shown in figure 7.15 a methane flame analogous the the previous hydrogen flame is pulsating inside the quartz cylinder. The use of the cylinder allowed the flame to be as unstretched as possible. For all such experiments, the outer flame always went extinct very shortly after the onset of the instability. It was never possible to observe sustainable intensity pulsations in this region of the burner, probably because of the strong concentration gradients. The observed flame somewhat reduces in size during the low intensity part of the cycle and expands back toward the wall while remaining planar. In figure 7.15 this is shown by the vertical dashed lines representing the maximum extent of the flame observed during the higher intensity part of the cycle. In this figure the flame appears to cover only about half of the inner cylinder diameter. This effect is only a result of the limited sensitivity of the camera used and the fact that on the edges of the flame the light emission of the flame is integrated over a shorter length. With the naked eye, the flame was observed to extend much closer to the quartz cylinder walls. Typical variations in the flame diameter as recorded by the camera over one pulsation cycle are on the order of 2 mm.

When the quartz cylinder was present in the burner, it was very difficult to achieve sustainable pulsating flames under certain conditions. The main problem is that flames with low velocity or created using mostly CO_2 as the inert (the low frequency flames) loose their flatness as soon as the pulsations begin to grow in amplitude. In flames pulsating at a higher frequency, the very uniform species distribution means that the whole flame reaches instability at the same time. As a result, the amplitude of the instability grows very quickly often leading to flame extinction. This complicates the use of a large parameter range and motivated the comparison of the pulsating flames generated with and without the quartz cylinder in the burner.

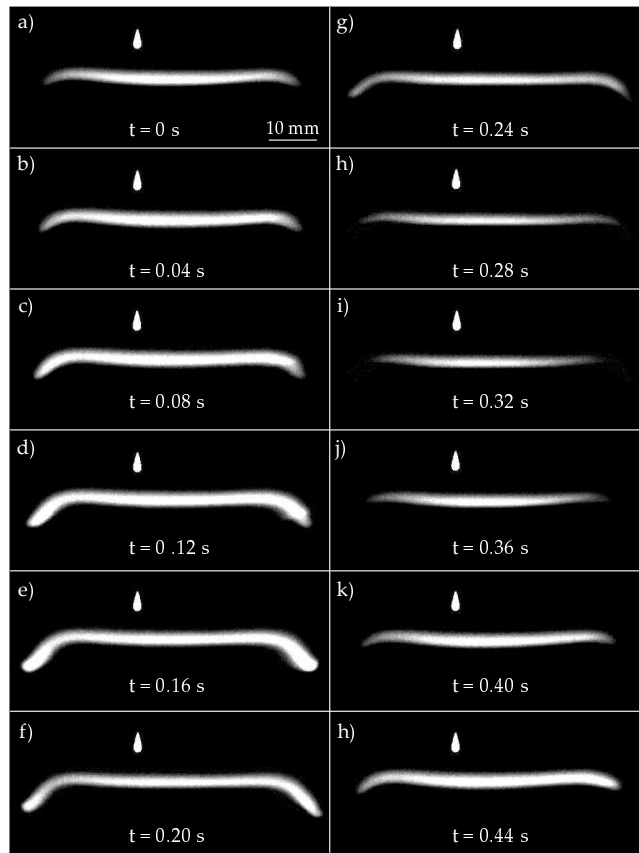


Figure 7.16: Pulsation in a methane flame without the inner quartz cylinder present. As the flame increase intensity, it expands in the leaner burner edges and dips down as a result.

When the instabilities were allowed to develop unimpeded in the chamber, the edges of the flames were seen to dip downward during the high intensity part of the cycle. This can be seen in the sequence presented in figure 7.16. In the high intensity part of the cycle, the flame expands in the periphery of the burning chamber where the lower mixture strength pushes the edges of the flame down towards the fuel side.

It is without surprise that the parameters affecting the magnitude of this phenomenon are those suspected to play a role in the extent of velocity and species boundary layers present near the walls. For instance, if the bulk velocity is increased relative to the situation presented in figure 7.16, the edges of the flame remain almost stationary throughout the cycle. This can be seen in the sequence presented in figure 7.17 where the velocity is 19.42 mm/s, compared to 13.87 mm/s for the previously mentioned flame. In general, this behavior of the flame edges was always more pronounced in flames pulsating at a lower frequency. When comparing both the pulsation amplitude and frequency, no difference were measured between the flames created with and without the quartz cylinder in the burner. Consequently, since it allows the investigation of a wider range of parameters, the results presented in this section were realized mostly

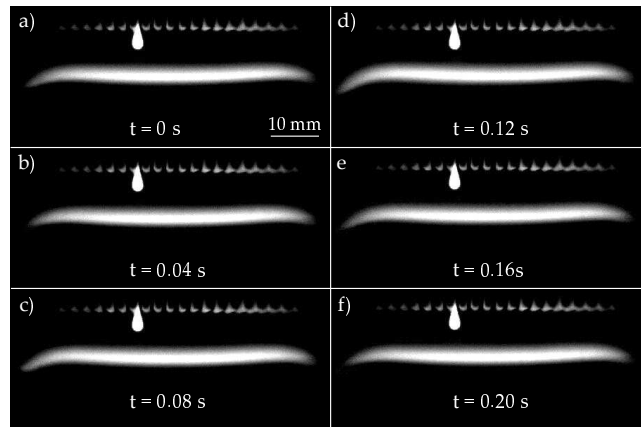


Figure 7.17: Pulsation in a methane flame without the inner quartz cylinder present. The burner parameters are chosen to reduce the wings on the flame edges.

without the inner cylinder.

Examples of the variation of the measured flame light emission are presented in figure 7.4.1. In some of the flames observed, the onset of the instability is quickly followed by a period of rapid growth of the pulsation amplitude which leads to flame extinction. This behavior was particularly observed in moderately low frequency (1-3 Hz) pulsating flames (hydrogen flames, flames with low bulk flows) and in flames generated with the inner quartz cylinder present. A typical intensity variation for these flames from the onset to flame extinction is presented in figure 7.18(a). In other flames, at the threshold of the instability, it was possible to observe pulsation spontaneously appear and dampen by themselves. The reduction in the pulsation amplitude of one such flame is presented in figure 7.18(b). Spatial inhomogeneities in the burner sometimes resulted in two regions of the flame pulsating at slightly different frequencies or at the same frequency but out of phase. An example is presented in figure 7.18(c), with a modulation in the integrated light signal gathered resulting from the interference between the two frequencies. However, for the majority of the results presented here focusing on the frequency of the oscillations, the signal used was that of saturated and steady-state oscillations. In several cases, the burner parameters were kept constant for close to one hour while different measurements were taken without measurable change in the pulsation frequency.

As the intensity of the chemical reaction oscillates in the reaction sheet, so does the heat released. This has an effect on the fluid mechanics of the burner and results in a variation of the flame position coupled with the variation of the flame intensity. The results presented in figure 7.4.1 show this effect for two flame with different operating parameters. Naturally, the magnitude of this effect depends on the relative importance of heat release when compared to bulk velocity. In high velocity flames, which tend to pulsate at relatively high frequencies, this effect results in variations of the flame position on the order of 0.5 mm and is not visible to the naked eye. When the bulk flow and the pulsation frequency is lower however, the flame position often changes by over 2 mm between the high and low intensity part of the cycle. It is also interesting to notice that the intensity and position variations are almost in phase at high frequencies but drastically out of phase at low frequencies. This suggests that at high frequency the

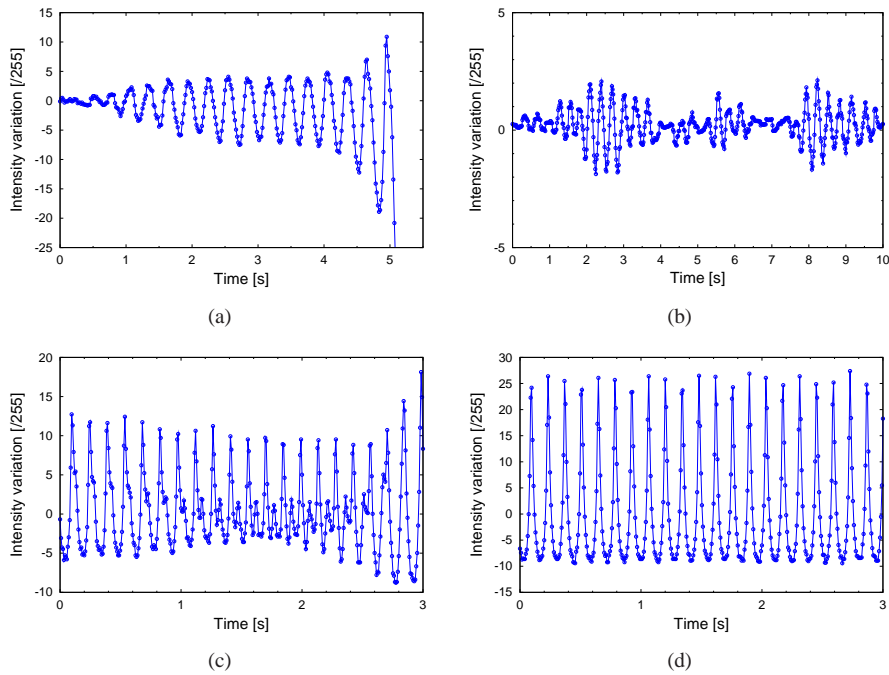


Figure 7.18: Variation of the flame intensity for different types of pulsations. a) Pulsation with rapid growth in amplitude, quickly leading to extinction. b) Damping of pulsations. c) Pulsating flame with two competing frequencies. d) Stable intensity pulsations.

decrease in heat release is too brief for a new equilibrium to be reached in the chamber before it increases again.

Contrary to cellular flames, in the case of the intensity pulsation instability, the flame front remains homogeneous spatially. This means that species concentration profiles can be taken reliably in unstable flames without concern that the particular location chosen is not representative of the whole flame sheet. Such reactant concentration profiles taken in two flame with only small to moderate amplitude pulsations are presented in figure 7.20. For these particular flames, the displacement of the flame front during the oscillation is small enough not to affect significantly the spatial resolution of the measurement. From these profiles the reactant leakage through the reaction sheet is important, as was the case for flames very close to the onset of cellular instabilities. This again indicates that at least some degree of reactant pre-mixing occurs for these pulsating flames.

7.4.2 Pulsation frequency scaling

In order to determine the pulsation frequency and amplitude as accurately as possible, the raw intensity signal is processed to ensure a reliable transfer to the frequency domain. All of the signal processing operations mentioned here are implemented using the MATLAB environment. The frequency signal is obtained through the MATLAB implementation of the fast Fourier transform (FFT), an efficient algorithm to compute

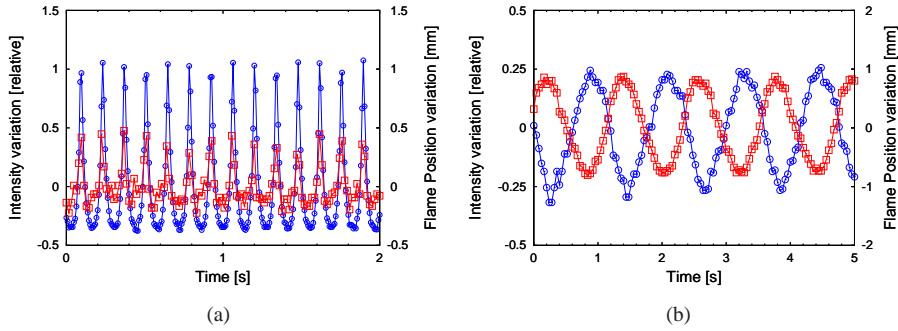


Figure 7.19: Simultaneous variation of the flame intensity and position. a) For high frequency pulsations, the variation in position is small and in phase with the high amplitude oscillation (over 100% or the average). b) For low frequency oscillations, the flame position variation is high (± 1 mm) and out of phase with the intensity variation.

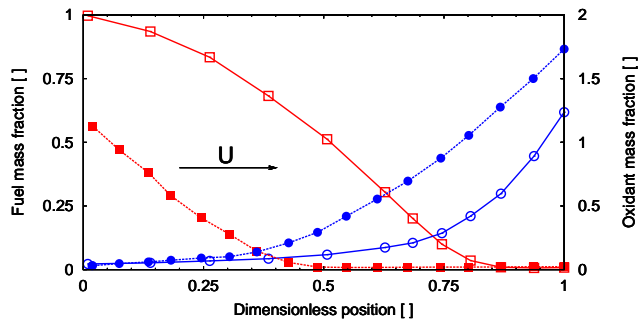


Figure 7.20: Concentration profiles showing the reactant leakage across two pulsating flames. The same virtual origin was used for the two flames produced using different inert composition, explaining their different mixture strength. The flame parameters corresponding to the open and filled symbols are listed in table 7.1 are listed under a) and b), respectively.

Figure	U [mm/s]	% CH ₄	Inert		Le_x []	Le_f []	ϕ []	f [hz]
			[%He]	[%CO ₂]				
7.16	13.87	11.5	40	60	1.05	0.95	0.62	2.62
7.17	19.42	11.0	75	25	1.23	1.08	0.95	5.81
7.18(a)	19.42	11.0	75	25	1.23	1.08	0.95	5.81
7.18(b)	13.87	11.0	15	85	0.96	0.88	-	1.04
7.18(c)	13.87	12.5	90	10	1.41	1.16	1.31	7.21
7.18(d)	13.87	12.5	85	15	1.33	1.13	1.18	6.97
7.19(a)	13.87	12.5	90	10	1.41	1.16	1.31	7.21
7.19(b)	13.87	12.0	20	80	0.95	0.86	0.89	0.86
7.20(a)	13.87	12.0	50	50	1.09	0.99	0.81	3.67
7.20(b)	13.87	12.0	0	100	0.91	0.82	0.57	0.73

Table 7.1: Burner parameters for the flames presented in section 7.4.1. All of the flames are realized using CH₄ as the fuel, U is the bulk flow velocity and f the measured pulsation frequency. The symbol [-] is used when the data is not available.

the discrete Fourier transform (DFT) of the temporal signal. The procedure used starts by removing the unwanted frequencies in the signal. Of particular concern is the very low frequency modulation² of the average measured light intensity which can cause problems in the frequency analysis. This is done through the use of a finite impulse response (FIR) bandpass filter. The filter parameters are chosen to ensure that both the main frequency and the first harmonic remain intact since the ratio of these two quantities is of interest in weakly non-linear stability theory.

It is also necessary to address the spectral leakage occurring in the discrete Fourier transform (DFT) caused by the finite length of the available signal. This effect stems from the DFT assumption that the signal is periodic. The result is that some of the signal energy end up in frequencies not present in the sample. The issue is addressed by multiplying the signal with a window function of the same length that falls to zero on both ends. This forces periodicity even if the first and last values of the signal are not equal, attenuating the secondary peaks in the frequency domain. The Hann window is used here, providing a relative side lobe attenuation of -32 db for the 1250 samples long signals typically used here. An example of signal of flame intensity before and after application of the bandpass filter and the Hann window is presented in figure 7.21(a).

In order to obtain the pulsation amplitude from the frequency signal, a dummy cosines signal was used. This reference was constructed using a known amplitude and a frequency close to the actual frequency of the signal. The same filters were then applied to the reference dummy and the flame pulsation signal, as can be seen in figure 7.21(b). The ratio of the filtered and unfiltered amplitudes of the fundamental frequency peak in the dummy was then used to calculate the true amplitude of the flame intensity pulsation from its filtered spectral representation. This is illustrated by the sample Fourier transforms presented in figures 7.21(c) and 7.21(d). The flame used

²This modulation is on the order 0.1 Hz and is observed in many signals. It was often found to be the results of variations in the aspect of the flames edges downwards motion during the high intensity part of the cycle, mentioned in section 7.4.1. The cause is therefore related to low frequency unsteadiness in the burning chamber boundary layers and is not expected to influence the fundamental pulsation frequency.

for the example of figure 7.4.2 pulsates at 6.48 Hz with an amplitude in the maximum measured pixel value of 2.71. Relative to the average maximum light emission measured, this corresponds to a variation of 10.2%. The flame used had a bulk flow of 16.65 mm/s containing 10.5% CH₄ by volume. The inert composition was 75% He with the remainder of CO₂, yielding Lewis numbers of $Le_o = 1.25$ and $Le_f = 1.09$.

Results from linear stability analysis

Results from the linear stability analysis of the thermal-diffusive instabilities in the idealized one dimensional configuration reveal that the pulsation frequency should scale following equation 7.2 [71]. Here the parameter ω_I is the imaginary part of the growth rate of the most unstable disturbance at the marginally stable state.

$$f \sim 2\pi \frac{U^2}{D_{th}} \omega_I \quad (7.2)$$

The term U^2/D_{th} represents a *diffusion frequency* with which the observed pulsation frequency should scale if it is assumed as a first approximation that the parameter ω_I is constant³. The experimental results gathered to clarify the scaling of the pulsation frequency can be grouped in two categories. In the first the bulk velocity is constant and the inert composition is varied, while the opposite being true for the second. In figure 7.22, both datasets are plotted against the diffusion frequency evaluated with the mixture transport properties measured at the flame. If the variation of the parameter ω_I could be neglected, the experimentally measured frequency should increase linearly with the diffusion frequency but the opposite is observed.

The results of figure 7.22 indicate that contrary to what was the case for the cellular flames (section 7.3), for pulsation instabilities the parameter dependence of the growth rate (ω_I in this case) needs to be considered in the scaling of the instability. ω_I can only be obtained numerically from the dispersion relationship and depends on the dimensionless parameters used in the analysis ($Da, \phi, Le_f, Le_o, \theta$). Here θ is the activation energy parameter or Zeldovich number. Unfortunately, the nature of the dependence of ω_I on these characteristic flame parameters is unknown, with the numerical results found in the literature being valid only for specific situations [71, 45].

Dimensional analysis

When facing such a problem involving a large number of physical parameters, it is often useful to use the principle of dimensional analysis to identify the dimensionless groups governing the phenomenon. From the theoretical investigations mentioned previously and from physical reasoning, the pulsation frequency can be expected to depend upon the parameters listed in table 7.2. Generally speaking, these parameters account for the amount of heat supplied and the ability of the system to evacuate it away from the reaction zone. Other parameters might be involved and could be added to refine the model in further iterations.

Using the parameters of table 7.2, two dimensionless groups can be formed using the Buckingham-Pi theorem. The first one is $f * D_{th}/U^2$, which is the pulsation frequency divided by the diffusion frequency mentioned above. The second is $C_p * T_f/U^2$ and expresses the amount of chemical energy released in the reaction zone. The relationship between the two is plotted in figure 7.23, showing that these two parameters

³A similar approximation was quite successful for the scaling of the cell size in the cellular flames treated in section 7.3

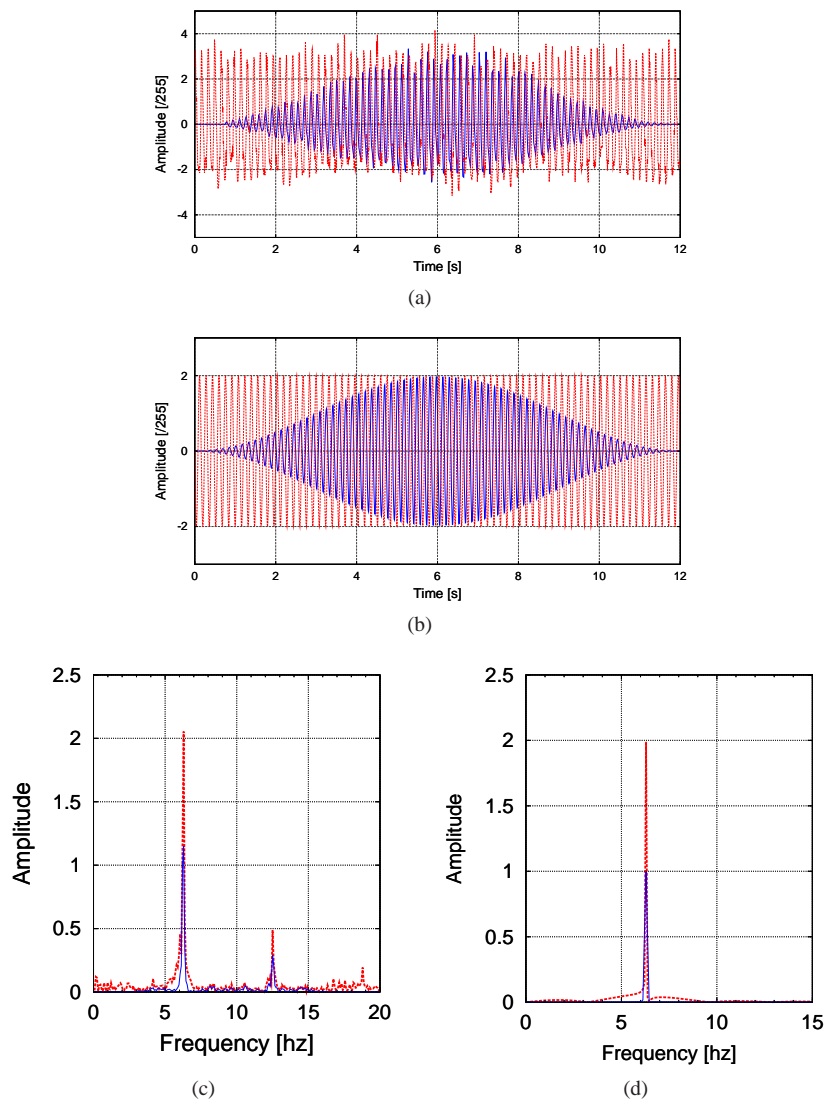


Figure 7.21: Treatments and Fourier transform of intensity signal. a) Raw input signal (---) and filtered signal (—). b) Dummy reference signal before (---) and after filtering (—). (c), (d) Frequency domain representation of the signal and the reference dummy, respectively.

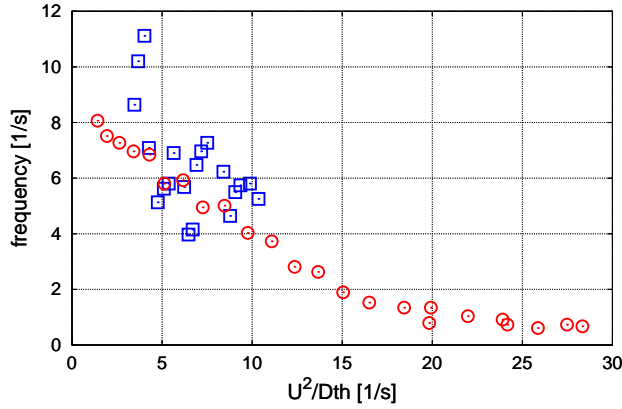


Figure 7.22: Pulsation frequency scaling with the diffusion frequency. The data does not scale as expected from the linear stability theory when the parameter ω_I is assumed constant.

Name	Symbol	Units
Pulsation frequency	f	s^{-1}
Thermal diffusivity	D_{th}	$m^2 s^{-1}$
Bulk velocity	U	$m s^{-1}$
Specific heat	C_p	$J kg^{-1} K^{-1} = m^2 s^{-2} K^{-1}$
Flame Temperature	T_a	K

Table 7.2: List of parameters considered for the dimensional analysis of the pulsation frequency scaling.

are not related by a simple power law, except at the larger values of the heat release parameter. Other quantities involved in the phenomenon and not included in the analysis can be responsible for the scatter observed. For instance, when only data points having similar values for both ϕ , Le_o and Le_f , the linear relationship becomes clearer, as can be seen from the third dataset plotted in figure 7.23. Accordingly, assuming constant Lewis numbers and mixture strength, the influence of the bulk velocity vanishes and the pulsation frequency can be expressed as:

$$f = \frac{C_p T_f}{D_{th}} \quad (7.3)$$

These results offer only limited insight on the phenomenon, hinting that some other relevant parameter was overlooked in the dimensional analysis. The group $f * D_{th}/U^2$ appears the proper dimensionless form for the frequency because its value varies around unity but $C_p * T_f/U^2$ is suspicious because of its extremely large magnitude. As an alternative dimensionless expression of the chemical heat release, the Damköhler number given in equation 3.20 is promising as it contains the Arrhenius factor which can possibly account for the non-power law relation of figure 7.23.

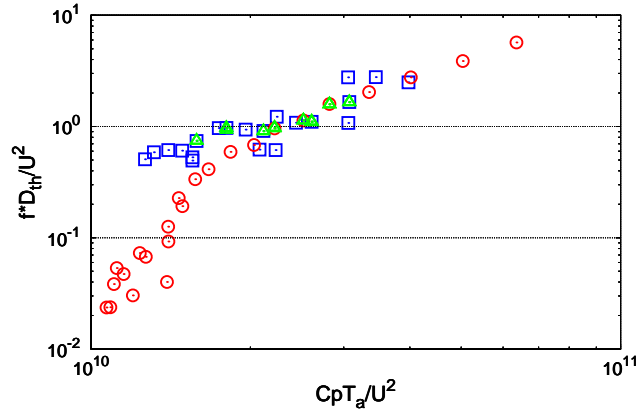


Figure 7.23: Pulsation frequency scaling obtained from dimensional analysis, with both the dataset gathered at constant inert composition (\square) and constant velocity (\odot) shown. The agreement between the two datasets is best when the flame mixture strength is similar (\triangle).

Scaling with Damköhler number

The experimental determination of the Damköhler number is not trivial, as can be seen by the large number of parameters involved in its definition, reproduced in equation 7.4. The main difficulty resides in finding suitable values for the activation energy E and the Arrhenius pre-exponential factor \mathcal{B} . The activation energy is especially troublesome since it must be determined experimentally from measured reaction rate constants. The data available in the literature for methane is limited [164] and valid only for specific reaction temperature and value of \mathcal{B} . This pre-exponential factor \mathcal{B} can be estimated analytically but often differs significantly from experimental values. Fortunately, it exhibits only a limited dependence on temperature and is not a important term in the Damköhler number expression.

$$\mathcal{D}_a = \frac{\lambda}{\rho_a c_p U^2} \left(\frac{R^0 T_a}{E} \right)^3 \frac{\nu_x c_p \bar{W}}{q R^0 W_f} P \mathcal{B} X_{f,-\infty} \exp(-E/R T_a) \quad (7.4)$$

In equation 7.4, the terms expected to have a dominating influence in the change of the Damköhler number between the flames studied here are D_{th}/U^2 , $(R^0 T_a/E)^3$ and especially $\exp(-E/R^0 T_a)$. Accordingly and because of the restrictions on the available data, all of the other parameters and E are assumed constant. The Damköhler number used in this section is a relative one, calculated with respect to a flame arbitrarily selected in the available dataset and assumed to have $Da = 1$. The measured dimensionless frequency $f * D_{th}/U^2$ as a function of this Damköhler number is shown in figure 7.24(a). In this figure, the correlation is much closer to a power law than in the previous cases. However it appears that, as in section 7.4.2, the two datasets gathered using constant mixture properties and constant velocity have approximately the same power law exponent but different pre-factors.

The first clues explaining this difference were found after systematic visual inspection of the videos. The spread observed in the data of figure 7.24(a) was found to be correlated to the difference in amplitude between the various pulsating flames

measured. As a initial approach, the video were simply categorized as almost stable (weakly pulsating), pulsating and almost extinct (high amplitude pulsations). The results plotted in figure 7.24(a) show a clear correlation for all three types of flames, with a slope in the log-log graph roughly equal to 0.5. Most of the data available was comprised of steady-state pulsation of medium amplitude because flames with similar aspect were desired to avoid saturation and under exposition in the videos. Using only this dataset of flames with similar pulsation amplitudes, the following correlation was found (plotted with the solid line in figure 7.24(a)):

$$\frac{f D_{th}}{U^2} = 0.909 * Da^{0.45} \quad (7.5)$$

The dimensionless frequency therefore scales roughly with the square root of the Damköhler number, at constant amplitude. The coefficient of determination R^2 of this correlation is excellent at 0.97. For simplicity, the square root of Da will be used as an approximation when further refining this correlation. Unfortunately, it was impossible to gather enough data points to verify if this relation still hold true for very high or very low pulsation amplitudes. The high amplitude flames are difficult to capture since they often quickly lead to extinction. On the other hand, low amplitude flames are hard to identify without complex video analysis. They are usually discarded as stable from visual inspection during the experiment, except during systematic experiments on the instability onset. The few data points available with flame close to the marginal state seem to indicate that a similar relationship can be found in those conditions.

The amplitude was measured quantitatively following the technique described at the beginning of section 7.4.2 with the resulting data plotted in figure 7.24(b). The trend observed with the naked eye in the videos is visible in this figure, with the flames close to the marginally stable state having an amplitude lower than the average. The flame identified as close to extinction have an amplitude significantly greater than the flames used to define the correlation of equation 7.5. The highest amplitudes measured represent a variation in the measured light emission equal to over 125% the average value. In figure 7.24(c), the variation of the amplitude is shown as a function of the constant in equation 7.5, using an approximate value of 0.5 for the power of the Damköhler number.

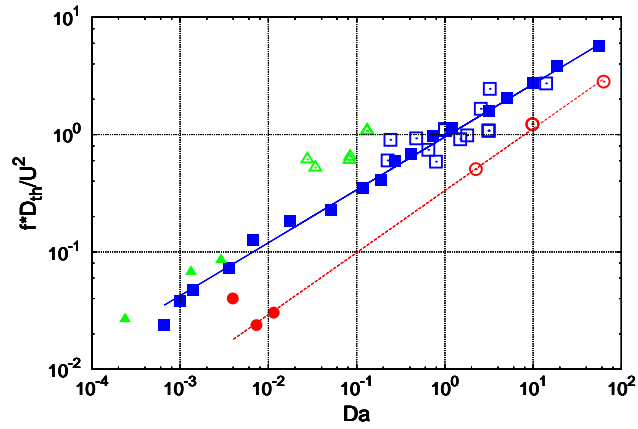
The limit-cycle oscillations observed are believed to be the result of supercritical Hopf bifurcation, like in the premixed configuration [165]. This belief is confirmed by the substantial reactant leakage measured and reported in figure 7.20 and 7.8, indicating some degree of premixing associated with the instabilities. If it is the case, the Stuart-Landau weakly non-linear stability theory [166] applies close to the bifurcation and predicts that the square of the oscillation amplitude should scale with the bifurcation parameter. Using the correlation defined in equation 7.5, yields the following relationship:

$$\frac{f D_{th}}{U^2 \sqrt{Da}} = C_0 + a \epsilon^2 \quad (7.6)$$

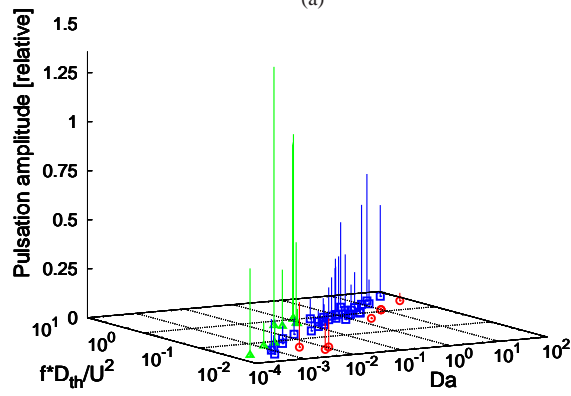
Where ϵ is the pulsation amplitude. This theoretical prediction is plotted as the solid line in figure 7.24(c). The constants C_0 is the dimensionless frequency divided by \sqrt{Da} when the amplitude is zero, corresponding to the marginally stable state. This value could be estimated directly from the available experimental data at very low amplitude. The value of the parameter a was then determined through the correlation found with the whole experimental dataset. By adjusting the value of C_0 slightly to

maximize the correlation coefficient, it was possible to achieve a correlation in qualitative agreement with the theoretical prediction, with the amplitude raised to the power 1.67. However, the R^2 for the correlation remained low at about 0.6. It should be emphasized here that the confidence in the amplitude data gathered in this experiment is limited because mainly of the spatial integration imposed by the acquisition technique used (see section 7.4.2).

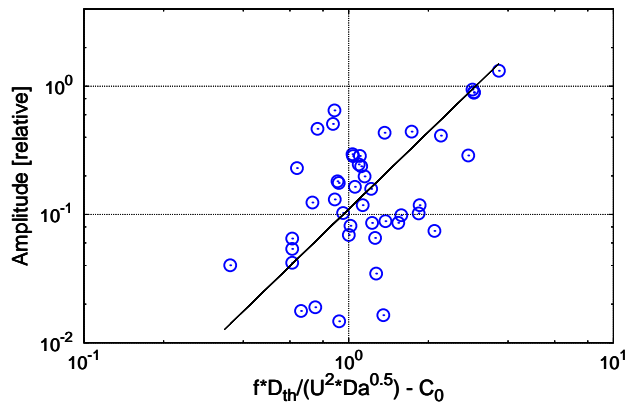
The ratio of the fundamental to the first harmonic of measured intensity signal was also calculated. According to weakly non-linear stability theory, the amplitude of the first harmonic should be proportional to the square of the amplitude of the fundamental. Attempts were made to verify this relationship, but the available amplitude data proved too unreliable to yield conclusive results. The spatial integration of the flame light emission inherent to the acquisition method used that causes an amplitude modulation when two regions of the burner pulsate at slightly different frequencies or out of phase. An example of such a modulated signal is given in figure 7.18(c). Refinements in the experiment should be implemented to investigate more deeply the role of the pulsation amplitude in the frequency scaling. Such refinements should include techniques allowing spatially resolved measurements of the intensity variation with a wide dynamic range. Recent development in sensitive temperature measurements based on optical techniques offering the required bandwidth is a promising prospective solution towards this goal.



(a)



(b)



(c)

Figure 7.24: a) Scaling of the pulsation frequency with the Damköhler number, with the different flame types observed: almost stable (\odot , \bullet), medium amplitude pulsations (\square , \blacksquare) and almost extinct (\triangle , \blacktriangle). The open and filled symbols are from datasets gathered at constant inert composition and constant velocity, respectively. b) Measured pulsation amplitude for the data in (a). c) Scaling taking into account the pulsation amplitude, with $C_0 = 0.05$ used.

Chapter 8

Conclusions and outlook

The burner presented in this thesis has evolved from the first experimental realization of a one-dimensional chambered diffusion flame [55, 96]. The novel symmetric design of the reactant supply to the combustion chamber allows the investigation of the effect of bulk flow magnitude and direction on a diffusion flame in the absence of significant strain. The improvements introduced in the present version of the burner allow a reduction of the parasitic flame curvature and residual strain observed in the initial implementation of the design. One important innovation is the use of a quartz cylinder placed inside the burning chamber to separate the more homogeneous central portion from the edges where velocity, species and temperature gradients exist. The result is the creation of a very flat flame inside the cylinder, where all the measurements are carried out.

The practical difficulty with this design which is due to the unknown proportion of fuel and/or oxidant lost into the exhausts has been overcome by the systematic use of mass spectroscopy in the combustion chamber. The key to the successful use of the mass spectrometer in this situation with large concentration variations is an innovative calibration procedure which yields continuous concentration profiles of the four or five species present in the burner and permits the determination of the effective mixture strength of the flame. The relative error in the measurement of this important flame parameter is estimated to be on the order of 5%, a precision that could not be approached without the novel calibration developed in this study.

In addition to the mass spectrometric measurements, a detailed characterization of the burner and flame produced has been achieved by using advanced experimental techniques. The fluid flow in the burner has been measured using LDA and has allowed a precise quantification of the residual strain experienced by the flame front, which was determined to be below 0.15 s^{-1} . The flame temperature was determined using thermocouple probes, constructed to avoid conduction losses and catalytic effects. The radiation corrected maximum measured temperature agree within 50 K with the flame temperature as determined from numerical adiabatic calculations. The measurements regarding the homogeneity of the species and temperature distribution in the central part of the burner have revealed deviations below 125 K in the flame temperature and 10 % in the counter-diffusing species volume fraction at the boundary. The good agreement between the present experiments and the simple theory for the flame position, the temperature and the species concentration profiles demonstrates that our new symmetric burner is a good approximation of a chambered one-dimensional diffusion flame, with one species transported against the bulk flow by diffusion only.

The central contribution of this study has been the quantitative documentation and analysis of thermal-diffusive instabilities close to extinction. The use of a two inert mixture (helium and CO₂) as dilution for the reactants has allowed a wide range of Lewis numbers to be investigated. The type of instabilities observed close to extinction has been mapped in the Lewis number parameter space for both hydrogen and methane flames burning with oxygen. In hydrogen flames, a cellular structure was observed for the low Lewis numbers associated with a dilution gas comprised mostly of CO₂. The characteristic size of the cellular pattern was observed to grow as the Lewis number increased when CO₂ was replaced by helium in the inert. It ranged from about 7 mm for flames diluted in pure CO₂ to 15 when mostly helium was used. The cell size scaled rather close to linearly with the diffusion length l_D , in good agreement with theoretical predictions.

The transition from cellular to intensity pulsations as the dominant mode of instability close to extinction occurred for hydrogen flames when 80% of the dilution mixture was helium. The weak light emission of these H₂ pulsating flames prevented their detailed investigation and methane flames were used to study the phenomenon for the first time in an essentially unstrained setting. Pulsation frequencies in the range of 0.6 to 11 Hz were observed in these flames using the same two inerts for dilution. A correlation was found for the scaling of the pulsation frequency as a function of the flame parameters: the pulsation frequency multiplied by the thermal diffusion time was found to scale approximately with the square root of the Damköhler number.

For the first time, theoreticians now have experimental data in unstrained diffusion flames available to validate their models. Direct comparison between observations and the theoretical predictions is however not trivial beyond what has been done in this thesis because of the limited parameter range which it is possible to explore experimentally. In the experiment, one also observes saturated modes while the theory is presently limited to infinitesimal perturbations. Nevertheless, with this in mind future theoretical and numerical investigations can be designed specifically to allow quantitative comparisons.

On the definition of the mixture strength ϕ

The experimental results gathered in this thesis have revealed the limitations of the currently used definition of the mixture strength ϕ . The virtual origin technique implemented in section 6.5 to compensate for the velocity or density induced variation of the boundary conditions while keeping a constant ϕ illustrates the arbitrary nature of this definition. The ϕ stays constant because the concentration of the oxidant at the boundary has not changed, but the distance between the flame and the boundary has changed. Surely from the *flame point of view* the situation must be different.

Let's consider an example in the configuration most frequently used in this thesis, with the oxidant counter-diffusing against the bulk flow. For a given flame a certain amount of oxidant is present at the boundary, of which only a fraction will manage to reach the reaction zone. Now, to compensate for the increase in the oxidant volume fraction at the boundary following a decrease in bulk velocity a new virtual origin is taken upstream of the initial boundary position. At this new location, the amount of oxidant is the same as in the previous case; What has changed is the value of the exponential in the concentration profile of equation 3.15. The definition of the mixture strength should therefore include not only how much of the counter-diffusing reactant is supplied but also how it is supplied. As new quantity, for instance the maximum

slope of the mass fraction of the counter-diffusing species at the flame, might be a useful and physically more meaningful measure of the ratio of the supplied fuel to the available oxidant, weighted by the stoichiometric ratio.

Future work

The numerous improvements implemented and the detailed characterization carried out in the new version of the burner have yielded a clear picture of the configuration presented in this thesis. Refinements are still possible and have been identified to bring this experimental realization still closer to the idealized one-dimensional construct. One of the main issues is the management of heat losses, particularly in the chimney since they are believed to be at the origin of the most detrimental wall effects observed in the burner, that is the variation in the counter-diffusing species boundary condition. Resulting in flame front curvature and residual stretch. One option to improve this situation would be to use a fluid or paste with a high thermal conductivity in the chimney to improve the heat transfer between the injection and extraction tubes. The use of electrical heating in this region of the burner is also a possible solution, but in both cases temperature inhomogeneities will probably remain, albeit with a lower magnitude than is currently observed. A more definitive solution to this issue would be to place if not the whole burner, at least the chimney in an oven heated to the temperature of the exhaust gas. This would however require a considerable increase in the complexity of the experiment to maintain optical and physical probing access to the combustion chamber.

The use of more advanced experimental techniques could also help to resolve remaining issues. In particular, laser based temperature and species measurements could provide a drastic improvement in dynamic range of the measurement of planar intensity pulsations. This is of course provided that sufficient bandwidth could be achieved to temporally resolve the phenomenon. The technique would also allow the spatial resolution of the pulsation, avoiding the problems encountered with spatially integrating techniques such as the one used in this thesis when parts of the flame pulsate out of phase with each other. The results gathered in this way would more importantly provide a reliable measurement of the pulsation amplitude, allowing more in-depth analysis on the nature of the instabilities present and its scaling. Using such techniques might also permit to further investigate very weakly luminous phenomena that could only be observed with the naked eye in this study, such as pulsations or rotating spirals in hydrogen flames.

The effect of heat loss to the injection array on the thermal diffusive instability is also difficult to evaluate in this experiment, but is likely to have a significant effect. Attempts to quantify this process, either experimentally or analytically, would be useful since heat loss is known to play a role in thermal-diffusive instabilities. For instance, Cheatham and Matalon [167] have demonstrated that intensity oscillation can be triggered both by high Lewis number without heat loss and by high heat loss, even for relatively small Lewis numbers.

The symmetric burner design introduced here is in particular aimed at the first investigation of a purely diffusive unstrained flame in the zero bulk flow limit. Experiments have been conducted to generate such a flame but have not met with success. These attempts involved starting with a stable flame and a small bulk flow, then open the extraction plenum of the advected species to remove the bulk flow by allowing the products to escape symmetrically. However, as this happened, the flame always collapsed on one of the injection arrays, either partially or totally. Once this condition

developed, it was very difficult or impossible to stabilize the flame front in the middle of the burner, even after one of the exhaust plenums was again closed. More experiments need to be made before the realization of such a purely diffusive flame without bulk flow can be ruled out. Perhaps some kind of active control is required in the pressure drop between the exhaust plenums. It might also be useful to try placing different devices inside the burning chamber to keep the flow one dimensional and prevent the formation of convection cells believed to be at the origin of the partial flame front collapse. A honeycomb structure might be useful for this task. Alternatively, the burner could be lit with both exhausts already open. This last option was not tried during the intense measurement sessions leading to this thesis for fear that the stronger explosions resulting from ignition in a quiescent chamber with a larger volume of explosive mixture would damage the equipment.

Research opportunities

The novel burner configuration presented in this thesis has only been used so far to investigate thermal-diffusive instabilities in the absence of strain. However, the possibility to generate such unstrained diffusion flames also offers new and unique opportunities in other fields of research. For example, to generate planar intensity pulsations, rich methane flames were produced and the formation of a highly luminous soot layer on the fuel side of the flame was noticed. A snapshot is shown in figure 8.1 where a bright yellow band is visible below the flame. The conditions under which this chance observation was made could be optimized specifically to improve the one-dimensional character of the soot layer. The burner design used in this thesis could therefore be used as a new tool to investigate the effect of strain and in particular the absence of strain on the formation of soot in hydrocarbon flames. Research on the subject has so far been limited to flame configurations where strain is always present [48, 168].

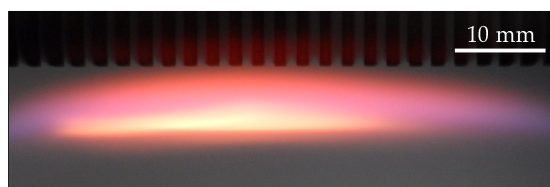


Figure 8.1: Chance observation of a soot layer forming on the fuel side of a rich methane flame.

Diffusion flames of methane and oxygen can also be used for the production of carbon nanotubes [169]. This discovery was made while investigating the effect of the strain rate on the microstructure of the soot formed in an opposed jet flame. The technique is novel because it provides a means to continuously produce this promising material, in contrast to the batch processes typically used today. The strain has been observed to have an effect on the structure of the carbon clusters formed. An unstrained flame would therefore be a useful research tool to investigate the parameters relevant to carbon nanotube formation in diffusion flames without aerodynamic perturbations.

Appendix A

Mass spectrometer system analysis

The initial trials of the instrument *in situ* revealed that its complex and sometimes unpredictable response to the numerous complicating aspects of this experiment (wide concentration range, presence of reactive species, etc.) would require a detailed analysis of the system to understand its intricacies. In this section, the pressures and flow rates through the different components of the mass spectrometer are determined. This will allow in the next two sections the identification of the sources of non-linearity and the implementation of an appropriate calibration procedure.

This mass spectrometer is designed to be able to sample gas mixtures directly at atmospheric pressure. Before analysis, the pressure of the sample must be lowered drastically to bring it to a state where the molecules are far enough apart to stop interacting with each other. Such a rarefied gas is said to be in molecular flow, its motion no longer governed by pressure differentials but only by the random kinetic velocity of the atoms and molecules it contains. This velocity of the molecules will play a critical role in the dynamics of the sample transmission between the different parts of the system. The velocity distribution of the molecules in a gas follows the Maxwell-Boltzmann distribution and quantities such as the mean speed of the molecules v_a will characterize the gas ability to move in free molecular flow.

$$v_a = \sqrt{\frac{8\kappa T}{\pi m}} = \sqrt{\frac{8RT}{\pi M}} \quad (\text{A.1})$$

Here $\kappa = R/N_A = 1.38e-23$ is the Boltzmann constant, $R = 8.3144$ the perfect gas constant, $N_A = 6.022e23$ Avogadro's number, T the temperature, m the mass of the particle and M the molecular weight. From this equation, it is obvious that the mean speed and hence many features of the system, is gas specific. For the numerical applications presented in this section, the mean molecular speed of CO_2 at 300 K, which is 379.9 m/s, will be used since this species usually makes up most of the mixtures analyzed.

A.1 Working pressures

To verify that the molecular flow assumption is reasonable for the different parts of the system, it is necessary to compare the mean free path (L) of the molecules with a

characteristic length scale (a). The resulting ratio is called the Knudsen number (Kn) and for $Kn > 1$ a gas can be considered in free molecular flow. For $Kn < 0.01$ the flow is considered viscous and the usual equations of fluid mechanics can be used. Between those two extreme values correction factors can be applied to either the viscous or molecular equations to properly capture the transitory nature of the flow.

$$Kn = \frac{L}{a} \quad (\text{A.2})$$

$$L = \frac{RT}{\sqrt{2\pi d^2 N_A P}} \quad (\text{A.3})$$

In this system the temperature is regulated to avoid condensation so the mean free path will be mostly a function of the pressure maintained in the different components of the instrument. A schematic representation of the sampling and analysis system of the MKS Cirrus is presented in figure A.1. In vacuum systems, the ability of a channel to allow the flow of gas is usually represented by the conductance C [170]. This quantity corresponds to the rate of flow (throughput) Q per unit of pressure difference between the two ends of the channel. The units of the conductance is m^3/s so the throughput Q is not a volumetric flow rate, it is a quantity that illustrates the mass flow, a pressure multiplied by a volume.

$$C = \frac{Q}{P_2 - P_1} \quad (\text{A.4})$$

The components used to create three successive pressure drops in the sample as it is transported towards the mass filter are presented with their conductances in table A.1. The resulting pressure variation experienced by the sample and the associated change in the mean free path are summarized in table A.2. The values of the pressures at point B was communicated by the manufacturer and a total pressure gauge gives the pressure in the vacuum chamber D. The rest of the values had to be determined analytically.

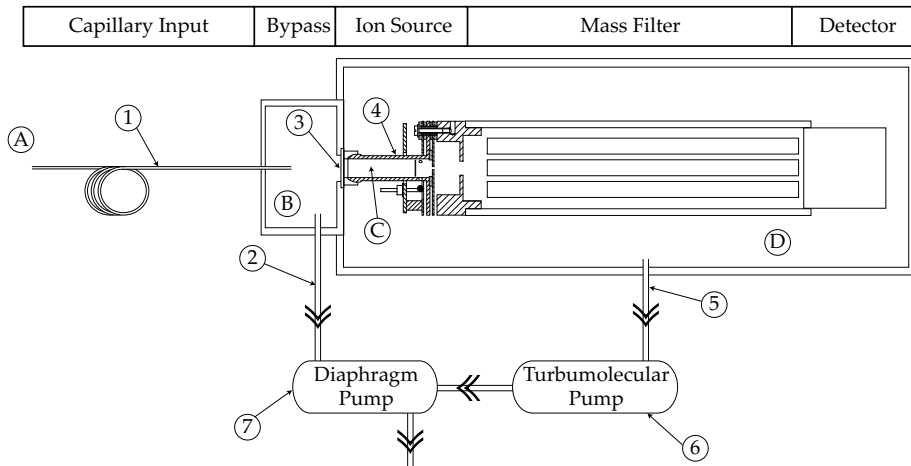


Figure A.1: Schematic representation of the vacuum system of the mass spectrometer. 1. The capillary input, 2. Bypass line, 3. Orifice, 4. Ionization chamber, 5. Exhaust line. The conductances and pressures of the various components are presented in tables A.1 and A.2.

Component	Label in figure A.1	Conductance [m ³ /s]
Capillary line	1	3.41e-9
Orifice plate	3	6.71e-8
Ion source	4	2.23e-4

Table A.1: Conductance values (for CO₂) for the different components of the vacuum system

Region	Label fig. A.1	Pressure		Mean Free Path [m]	Kn []
		Nominal [mbar]	Measured [mbar]		
Sampling	A	970	970	6.02e-8	6.02e-4
Bypass	B	5	5	11.66e-6	0.78
Ion. Chamber	C	1.51e-3	1.50e-3	38.33e-3	38.33
Vacuum chamber	D	1e-5	4e-6	9.60	192

Table A.2: Values of pressures and mean free paths throughout the vacuum system.

As can be seen in table A.2 the flow at the sampling end of the capillary is obviously viscous. The expression given in equation A.6 for the volumetric flow rate and the conductance of the capillary can therefore be estimated using the Hagen-Poiseuille equation A.6[171]. This requires the flow to be laminar as will be verified once the flow rate is known. Here \dot{V} is the volumetric flow rate, $r = 0.05\text{mm}$ is the radius of the tube, l its length and μ the dynamic viscosity. Here the term P_a , the average pressure, is added to yield a mass flow rate Q consistent with the rest of our development. This relation is only an approximation since thermal and compressibility effects can significantly change the result [172, 173, 174], but will be sufficient for a first approach.

$$\dot{V} = \frac{\pi r^4}{8\mu l} \Delta P \quad (\text{A.5})$$

$$C_{Capil} = \frac{\pi r^4}{8\mu l} P_a \quad (\text{A.6})$$

Using this conductance, adding the conductance from the bypass line 2 in fig. A.1, and using the specifications of the bypass pump, it is possible to determine the pressure in the bypass chamber, labeled B in figure A.1. This pressure is important because it controls the flow rate inserted in the ionization chamber and hence its operating pressure. Using various models to evaluate the conductance of the bypass line in the transition regime ($Kn \approx 0.05$)[175], the pressure in the bypass chamber was estimated to be between 1 and 2 mbar. These values are considerably lower than the nominal value of 5 mbar supplied by MKS. For the remainder of the calculations, the bypass chamber pressure was assumed to be 5 mbar, considering it to be a safe upper bound for this parameter. However, the implications of considering a lower value for this pressure will be briefly discussed.

The sample present in the bypass chamber is supplied to the ionization chamber through a disk, labeled 3 in figure A.1, with an array of 4 holes of 15 μm diameter to further reduce the pressure. The ion source enclosure, label 4 in fig. A.1, is pumped through 3 holes of 1 mm diameter exiting in the main vacuum chamber pumped by the turbomolecular pump. The pressure in this chamber is available through a total pressure penning gauge. To determine the pressure inside the ionization chamber, a critical parameter to determine the nature of the ionization process, it is then necessary to calculate the conductances of the orifice disk and the ion source enclosure.

The conductance of a circular orifice, in the molecular flow regime, is given by equation A.7, where A is the area of the orifice and v_a is the mean molecular speed. The total conductance of the orifice plate (C_{Or}) and ion source enclosure is then simply found by summing the conductances of the individual holes allowing gas exchange in each component. The resulting numerical values for the conductances for CO_2 at 300 K are given in table A.1.

$$C_{Orifice} = \frac{1}{4} v_a A \quad (\text{A.7})$$

From the values of the mean free path and Knudsen numbers presented in table A.1, one might argue that the flow in the orifice plate holes is not molecular but actually transitory. The value of $Kn = 0.78$ (based on the orifice diameter) for CO_2 is in fact a conservative estimate because all the other species having a smaller diameter, their mean free path is longer. For example in the same situation the Knudsen number for hydrogen is 1.41 and 1.05 for both oxygen and argon. Moreover, a slight increase in temperature also has the effect of increasing the mean free path and Knudsen number. For instance if heating is used to avoid condensation, as it often is, the temperature in the bypass region becomes 80°C and the Knudsen number for CO_2 is 0.91. The values for the hard sphere collision diameters of the various molecules and atoms were found in the literature[163].

Nevertheless, if we consider the viscous nature of the flow in the orifice, the conductance of this element can be determined using equation A.8[176] assuming a negligible plate thickness and isentropic gas expansion. In this equation γ is the isentropic expansion factor, which is equal to 1.30 for CO_2 at room temperature[171]. The resulting viscous conductance of the 4 orifice of the plate is $181.98e - 9 \text{ m}^3/\text{s}$, so about 2.7 times more than in the molecular regime.

$$C_{Or,Viscous} = \sqrt{\frac{\pi\gamma}{8} \left(\frac{2}{\gamma+1}\right)^{\frac{\gamma+1}{\gamma-1}}} v_a A \quad (\text{A.8})$$

The pressure inside the ionization chamber is found by solving successively the equation of the conductance A.4 between points B and C then between points C and D, assuming a constant mass flow rate. Assuming that the flow is molecular in the orifice plate 3, the pressure in the ionization chamber is $1.50e - 3 \text{ mbar}$. In the unlikely event that the viscous regime dominates in the holes of this component, the upper bound for the pressure inside the ion source enclosure is $4.07e - 3 \text{ mbar}$. These values are obtained assuming a 5 mbar bypass chamber pressure. If the pressure is 1 mbar, the flow rate to the ionization chamber is reduced and its pressure falls to $3.00e - 4 \text{ mbar}$

A.2 Sampling rate and ionization efficiency

The flow rate sucked from the flame can be found using the capillary conductance determined in the previous section and equation A.4. The resulting molar flow rate is $131.92E-9$ mol/s. This corresponds to $1.77e-4$ SLPM, a negligible proportion ($< 1/50'000$) of the approximately 10 SLPM bulk flow in the burner.

The resulting velocity is 0.432 m/s at the entrance and 83.83 m/s at the exit. This implies a maximum Reynolds number based on the tube diameter of $Re_D = Vd/\nu = 4.91$, confirming that the flow is laminar since the very narrow cross-section of the tube.

The actual flow rate entering the ion source through the orifice plate (label 3 in figure A.1) is determined by considering the conductances of the orifice plate and the ion source enclosure connected in series. The total impedance $Z_{Tot} = 1/C_{Tot}$ of this part of the circuit can be found by adding the impedance of the orifice and ion source.

$$\frac{1}{C_{Tot}} = \frac{1}{C_{Or}} + \frac{1}{C_{IS}} \quad (\text{A.9})$$

Assuming molecular flow in the orifice, the resulting molecular flow rate is $13.45e-9$ mol/s, or $8.10e15$ molecules per seconds (the bypass ratio is then about 10), implying a 9.81 bypass ratio. Considering that the total ionic current detected by the instrument supplied with pure CO_2 is approximately $3.85e-9$ A, or $24.02e9$ charges per second, this corresponds to a combined ionization and detection efficiency of $2.96e-4\%$. In other words, for CO_2 one out of every 337'000 molecules inserted in the vacuum chamber is detected. These values rely on the assumption that the pressure in the bypass chamber is 5 mbar. If instead we use the 1 mbar estimation from the hardware specifications, we find a flow rate into the ionization chamber of $2.26e-9$ mol/s. In this case, the bypass ratio is 58.4 and the ionization efficiency $1.77e-3\%$ or one out of every 56'600 molecules ionized and detected.

For these flow rate calculations, the conductances of the bypass line and the turbomolecular pump inlet (labels 2 and 5 in figure A.1) were evaluated conservatively using standard formulas [170, 175] and the available geometrical information. They are found to offer significantly less resistance to the gas flow than the capillary and the orifice plate and hence play only a minor role in the final values of the pressures and flow rates.

Appendix B

Possible reactant and inert combinations

The choice of the reactants (hydrogen and methane) and inerts (helium and CO₂) used in the experiments presented in this thesis is the result of a thorough selection process. Two inerts are required to generate the range of transport properties sought to cover as much as possible of the Lewis number parameter space. Other gases combinations were considered to generate the largest possible range of Lewis numbers. The use of noble gases for the inerts seemed very attractive at first because of their inherent stability and reliable detection by mass spectrometry. However, the use of two noble gases as inerts plus the two reactants and the two products (H₂O and CO₂) resulting from carbon-based fuel combustion would require a 6 gas mass spectrometer calibration. The complexity of this task forces the use of CO₂ as one of the inerts for all carbon-based fuels. For hydrogen, CO₂ must also be used to ensure that the flame emits enough light to be visible. Other species with similar properties could be used, but CO₂ was used in hydrogen flames as well to avoid complications. Nitrogen for instance, which is less stable than CO₂ at high temperature, resulting in the formation of nitrogen oxides that should be accounted for in the calibration procedure.

To produce the high Lewis numbers necessary to observe the planar intensity pulsations described in section 7.4 required the use of either heavy fuels or light inerts. Both of these choices had drawbacks that had to be weighted in order to find the optimal gas combination. The light inert chosen was naturally helium because of its extremely low molecular mass, very good high temperature stability and affordable prices. The Lewis numbers covered using these inerts and some other on three different fuels burning in hydrogen is given in figure B.1.

The use of heavier carbon-based fuels would necessitate extensive re-calibration of the mass spectrometry system or the implementation of another technique to measure the effective mixture composition in the burning chamber. These heavier fuels are also associated with increased source and mass filter fouling in quadrupole mass spectrometers. The formation of soot in the chamber would also be an issue, preventing optical access to the chamber and necessitating frequent cleanup.

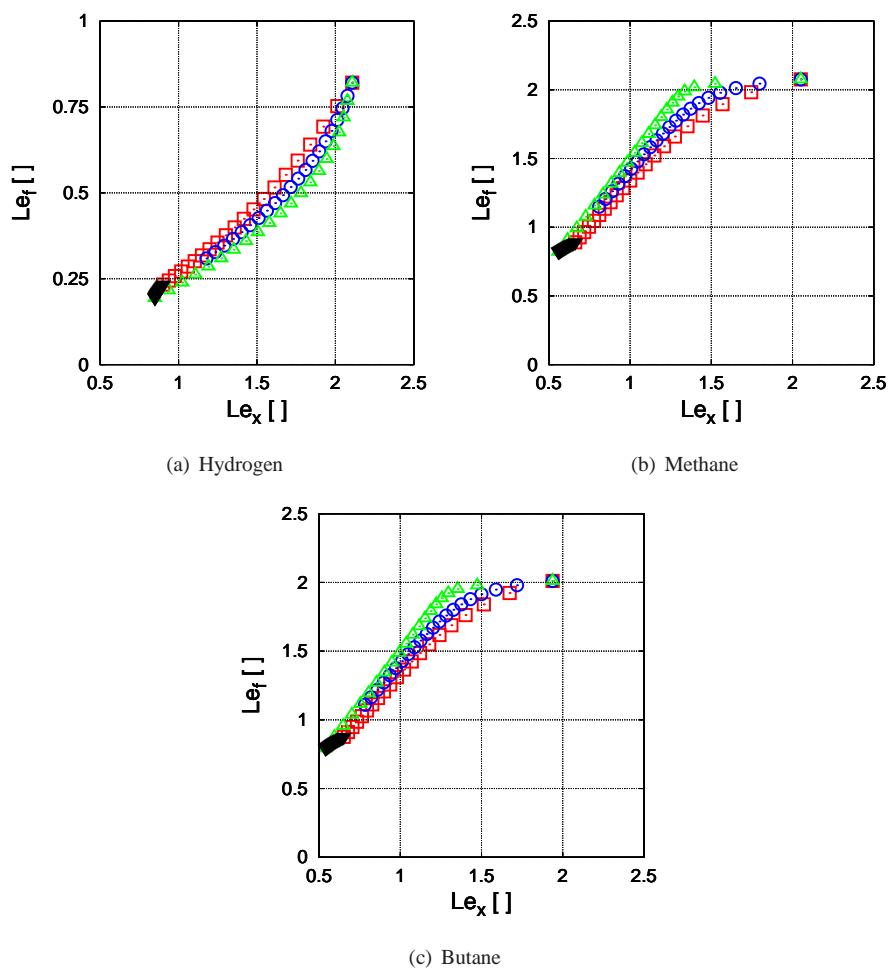


Figure B.1: Lewis number parameter spaces covered using hydrogen, methane and butane as the fuel. The inert mixtures considered are He and CO_2 (\square), He and Ar (\odot), He and Xe (\triangle) and CO_2 and Xe (∇).

Appendix C

Nomenclature

Notation

Latin alphabet

β	[m ³ /mol*s]	Specific heat at constant pressure
C_p	[J/kg*K]	Specific heat at constant pressure
D_a	[]	Damköhler number
D_i	[m ² /s]	Diffusivity of species i
$D_{th} = \lambda/(\rho C_p)$	[m ² /s]	Thermal diffusivity
E	[J/mol]	Activation energy
f	[1/s]	Pulsation frequency
K	[1/s]	Total stretch rate
K_c	[1/s]	Contribution of flame curvature to stretch rate
K_s	[1/s]	Strain rate
$Le_f = \kappa/D_f$	[]	Lewis number of fuel
$Le_o = \kappa/D_o$	[]	Lewis number of oxidant
Le	[]	Unique Lewis number or Lewis number of the most consumed reactant
P	[Pa]	Pressure
q	[J/kg]	Heat released per unit mass of fuel
Q	[J/mol]	Total heat released
R	[J/kg*mol]	Ideal gas constant
T_a	[K]	Adiabatic flame temperature
U	[m/s]	Bulk flow velocity
\bar{W}	[kg/mol]	Mean molecular weight
W_i	[kg/mol]	Molecular weight of specie i
X_f	[]	Fuel mass fraction
X_o	[]	Oxidizer mass fraction
x	[m]	Coordinate along burner length

Greek alphabet

ϵ	[variable]	Pulsation amplitude
------------	------------	---------------------

λ	[W/m ² *K]	Thermal conductivity
ν_i	[-]	Stoichiometric coefficient of species i
ϕ	[-]	Equivalence ratio (mixture strength)
ρ	[kg/m ³]	Density
σ^*	[-]	Real part critical growth rate in the marginal state
ω	[mol/s]	Chemical reaction rate
ω_I	[-]	Imaginary part of critical growth rate in the marginal state

Shorthand

CCA	:	Constant current anemometry
EI	:	Electron impact ionization
EPFL	:	Swiss federal institute of technology, Lausanne
FWHM	:	Full width half maximum
ID	:	Inner diameter
LDA	:	Laser Doppler anemometry
LIF	:	Laser induced fluorescence
LMF	:	Laboratory of fluid mechanics
MBMS	:	Molecular beam mass spectrometry
OD	:	Outer diameter
PPA	:	Partial pressure analyzer
QMS	:	Quadrupole mass spectrometer
RD	:	Reaction-diffusion
RGA	:	Residual gas analyzer
SEM	:	Secondary electron multiplier
SLPM	:	Standard liters per minute
SLR	:	Single lens reflex
TD	:	Thermal-diffusive

Bibliography

- [1] S. R. James, R. W. Dennell, A. S. Gilbert, H. T. Lewis, J. A. J. Gowlett, T. F. Lynch, W. C. McGrew, C. R. Peters, G. G. Pope, A. B. Stahl, and S. R. James. Hominid use of fire in the lower and middle pleistocene: A review of the evidence. *Current Anthropology*, 30(1):1–26, 1989.
- [2] Dick Stapert and Lykke Johansen. Making fire in the stone age: flint and pyrite. *Geologie en Mijnbouw*, 78:147–164, 1999.
- [3] N. Künzli, R. Kaiser, S. Medina, M. Studnicka, O. Chanel, P. Filliger, M. Herry, V. Puybonnieux-Textier F. Horak Jr, P. Qunel, J. Schneider, R. Seethaler, J.-C. Vergnaud, and H. Sommer. Public-health impact of outdoor and traffic-related air pollution: a european assessment. *The Lancet*, 356:795–801, 2000.
- [4] J. T. Houghton, G. J. Jenkins, and J. J. Ephraums, editors. *Climate change: The IPCC scientific assessment*. Cambridge University Press, 1990.
- [5] J. T. Houghton, Y. Ding, D. J. Griggs, M. Noguer, P. J. van der Linden, X. Dai, K. Maskell, and C. A. Johnson, editors. *Climate Change 2001: The Scientific Basis*. Cambridge University Press, 2001.
- [6] N. P. Tait. Soot formation in cracked flames. *Combustion and Flame*, 117(1-2):435–437, 1999.
- [7] D. Bradley, C. G. W. Sheppard, R. Woolley, D. A. Greenhalgh, and R. D. Lockett. The development and structure of flame instabilities and cellularity at low markstein numbers in explosions. *Combustion and Flame*, 122(1-2):195–209, 2000.
- [8] A. M. Turing. The chemical basis of morphogenesis. *Phil. Trans. of the Royal Soc. of London B*, 237(641):37–72, 1952.
- [9] A. Cho. Lifes patterns: No need to spell it out? *Science*, 303:782–783, 2004.
- [10] Philip K. Maini, Ruth E. Baker, and Cheng-Ming Chuong. The turing model comes of molecular age. *Science*, 2006.
- [11] Stefanie Sick, Stefan Reinker, Jens Timmer, and Thomas Schlake. Wnt and dkk determine hair follicle spacing through a reaction-diffusion mechanism. *Science*, 314:1447, 2006.
- [12] Han-Sung Jung, Philippa H. Francis-West, Randall B. Widelitz, Ting-Xin Jiang, Sheree Ting-Berreth, Cheryll Tickle, Lewis Wolpert, and Cheng-Ming

- Chuong. Local inhibitory action of bmps and their relationships with activators in feather formation: Implications for periodic patterning. *Developmental Biology*, 196:11–23, 1998.
- [13] Isaac Salazar-Ciudad and Jukka Jernvall. A gene network model accounting for development and evolution of mammalian teeth. *Proc. Nat. Acad. Sci. USA*, 99(12):8116–8120, 2002.
- [14] V. Castets, E. Dulos, J. Boissonade, and P. De Kepper. Experimental evidence of a sustained standing turing-type nonequilibrium pattern. *Physical Review Letters*, 64(24):2953–2957, 1990.
- [15] I. Lengyel and I. R. Epstein. A chemical approach to designing turing patterns in reaction-diffusion systems. *Proc. Natl. Acad. Sci. USA*, 89:3977–3979, 1992.
- [16] Julyan H. E. Cartwright. Labyrinthine turing pattern formation in the cerebral cortex. *J. theor. Biol.*, 217:97–103, 2002.
- [17] John E. Pearson. Complex patterns in a simple system. *Science*, 261(5118):189–192, 1993.
- [18] C. B. Muratov and V. V. Osipov. Scenarios of domain pattern formation in a reaction-diffusion system. *Phys. Rev. E*, 54(5):4860–4879, 1996.
- [19] W. Y. Tam, W. Horsthemke, Z. Noszticzius, and H. L. Swinney. Sustained spiral waves in a continuously fed unstirred chemical reactor. *J. Chem. Phys.*, 88(5):3395–3396, 1988.
- [20] K. J. Lee and H. L. Swinney. Lamellar structures and self-replicating spots in a reaction-diffusion system. *Phys. Rev. E*, 1995.
- [21] P. S. Hagan. Spiral waves in reaction-diffusion equations. *SIAM J. App. Math.*, 42(4):762–786, 1982.
- [22] William N. Reynolds, Silvina Ponce-Dawson, and John E. Pearson. Self-replicating spots in reaction-diffusion systems. *Phys. Rev. E*, 56(1):185–198, 1997.
- [23] S. Arrhenius. Uber die reaktionsgeschwindigkeit bei der inversion von rohrzucker durch sauren. *Z. Phys. Chem*, 4:226, 1889.
- [24] C. W. Wardlaw. A commentary on turing’s diffusion-reaction theory of morphogenesis. *New Phytologist*, 52(1):40–47, 1953.
- [25] J.E. Pearson and W. Horsthemke. Turing instabilities with near equal diffusion coefficients. *J. Chem. Phys.*, 90(3):1588–1599, 1989.
- [26] G. I. Sivashinsky. Instabilities, pattern formation and turbulence in flames. *Ann. Rev. Fluid Mech.*, 15:179–199, 1983.
- [27] J. Buckmaster. The structure and stability of laminar diffusion flames. *Ann. Rev. Fluid Mech.*, 25:21–53, 1993.
- [28] P. Clavin. Premixed combustion and gasdynamics. *Ann. Rev. Fluid Mech.*, 26:321–352, 1994.

- [29] Moshe Matalon. Intrinsic flame instabilities in premixed and nonpremixed combustion. *Annu. Rev. Fluid Mech.*, 39:169–191, 2007.
- [30] E. Mallard and E. Le Chatelier. Combustion des mélanges gazeux explosifs. *Ann. Mines*, 8(3):274–378, 1883.
- [31] A. K. Oppenheim and R. I. Soloukhin. Experiments in gas dynamics of explosions. *Annu. Rev. Fluid Mech.*, 5:31–58, 1973.
- [32] G. Darrieus. Propagation d’un front de flamme. Presented at La Technique Moderne (Paris) and in 1945 at Congrès de Mécanique Appliquée (Paris), 1938.
- [33] L. D. Landau. On the theory of slow combustion. *Acta Physicochim. USSR*, 19:77–85, 1944.
- [34] C. Clanet and G. Searby. First experimental study of the darrieus-landau instability. *Phys. Rev. Lett.*, 80(17):3867–3970, 1998.
- [35] G. Searby, F. Sabathier, P. Clavin, and L. Boyer. Hydrodynamical coupling between the motion of a flame front and the upstream gas flow. *Physical Review Letters*, 51(16):1450–1453, 1983.
- [36] J. P. Botha and D. B. Spalding. The laminar flame speed of propane/air mixtures with heat extraction from the flame. *Proc. Royal Soc. London A*, 225(1160):71–96, 1954.
- [37] E. Korusoy and J.H. Whitelaw. Extinction and relight in opposed flames. *Experiments in Fluids*, 33:75–89, 2002.
- [38] J. A. Eng, C. K. Law, and D. L. Zhu. On burner-stabilized cylindrical premixed flames in microgravity. *Proc. of the Combustion Inst.*, 25:1711–1718, 1994.
- [39] Geoffrey Taylor. The instability of liquid surfaces when accelerated in a direction perpendicular to their planes. i. *Proc. Royal Soc. London A*, 201(1065):192–196, 1950.
- [40] N. Peters. Laminar flamelet concepts in turbulent combustion. *Twenty-first symposium (int.) on Combustion*, 21:1231–1259, 1988.
- [41] L. L. Kirkby and R. A. Schmitz. An analytical study of the stability of a laminar diffusion flame. *Combustion and Flame*, 10(3):205–220, 1966.
- [42] J. S. Kim, F. A. Williams, and P. D. Ronney. Diffusion-thermal instability of diffusion flames. *J. Fluid Mech.*, 327:273–301, 1996.
- [43] J. S. Kim and F. A. Williams. Extinction of diffusion flames with nonunity lewis numbers. *J. Engineering Mathematics*, 31:101–118, 1997.
- [44] S. Cheatham and M. Matalon. A general asymptotic theory of diffusion flames with application to cellular instability. *J. Fluid Mech.*, 414:105–144, 2000.
- [45] P. Metzener and M. Matalon. Diffusive-thermal instabilities of diffusion flames: onset of cells and oscillations. *Combust. Theory Modelling*, 10(4):701–725, 2006.
- [46] C. K. Law. *Combustion physics*. Cambridge university press, 2006.

- [47] I. Glassman. *Combustion*. Academic Press, 3 edition, 1996.
- [48] J. Du and R. L. Axelbaum. The effect of flame structure on soot-particle inception in diffusion flames. *Combustion and Flame*, 100(3):367–375, 1995.
- [49] T.M. Brown, R.W. Pitz, and C.J. Sung. Oscillatory stretch effects on the structure and extinction of counterflow diffusion flames. *Proc. of the Combustion Inst.*, 27(1):703–710, 1998.
- [50] G.L. Pellett, K.M. Isaac, W.M. Humphreys, Jr., L.R. Gartrell, W.L. Roberts, C.L. Dancey, and G.B. Northam. Velocity and thermal structure, and strain-induced extinction of 14 to 100 % hydrogen-air counterflow diffusion flames. *Combustion and Flame*, 112(4):575–592, 1998.
- [51] V.R. Katta and W.M. Roquemore. Response of hydrogen-air opposing-jet diffusion flame to different types of perturbations. *Symposium (International) on Combustion*, 28(2):2055–2062, 2000.
- [52] B. Han, A. F. Ibarreta, C. J. Sung, and J. S. T'ien. Experimental low-stretch gaseous diffusion flames in buoyancy-induced flowfields. *Proc. of the Combustion Inst.*, 30:527–535, 2005.
- [53] H. Tsuji. Counterflow diffusion flames. *Progress in Energy and Combustion Science*, 8(2):93–119, 1982.
- [54] J. R. Nanduri, C. J. Sung, and J. S. T'ien. Structure and dynamic response of radiative diffusion flames. *Combust. Theory Modelling*, 9(3):515–548, 2005.
- [55] D. Lo Jacono, P. Papas, M. Matalon, and P. A. Monkewitz. An experimental realization of an unstrained, planar diffusion flame. *Proc. of the Combustion Inst.*, 30:501 – 509, 2005.
- [56] D. Lo Jacono. *Experimental study of cellular instabilities in non-premixed flames*. PhD thesis, Swiss Federal Institute of Technology Lausanne, EPFL, 2005.
- [57] C. K. Law, C. J. Sung, G. Yu, and R. L. Axelbaum. On the structural sensitivity of purely strained planar premixed flames to strain rate variations. *Combustion and Flame*, 98:139–154, 1994.
- [58] A. Smithells and H. Ingle. The structure and chemistry of flames. *J. Chem. Soc., Trans.*, 61:204–216, 1892.
- [59] F. A. Smith and S. F. Pickering. Bunsen flames of unusual structure. *Industrial and Engineering Chemistry*, 20(10):1012–1013, 1928.
- [60] Y. B. Zeldovich. Theory of combustion and detonation of gases (in russian: Teoriya goreniiya i detonatsii gazov). *Akademiia Nauk SSSR, Moscow*, 1944.
- [61] G. H. Markstein. Cell structure of propane flames burning in tubes. *J. Chem. Phys.*, 1949.
- [62] B. Jackson J. E. Garside. Polyhedral diffusion flames. *Nature*, 168:1085, 1951.
- [63] S. P. Burke and T. E. W. Schumann. Diffusion flames. *Industrial and Engineering Chemistry*, 20(10):998, 1928.

- [64] Y. B. Zeldovich. On the theory of combustion of initially unmixed gases. *J. Tech. Phys, Moscow*, 1949. Translated as Nat. Adv. Comm. Aero., Wash., Tech. Memo. 1296 (1951).
- [65] D. B. Spalding. A theory of the extinction of diffusion flames. *Fuel*, 1954.
- [66] D. B. Spalding and V. K. Jain. A theoretical study of the effects of chemical kinetics on a one-dimensional diffusion flame. *Combustion and Flame*, 6:265–273, 1962.
- [67] A. Liñán. The asymptotic structure of counterflow diffusion flames for large activation energies. *Acta Astronautica*, 1:1007–1039, 1974.
- [68] A. Liñán and A. Crespo. An asymptotic analysis of unsteady diffusion flames for large activation energies. *Combust. Sci. Technol.*, 14:95–117, 1976.
- [69] M. Matalon, G. S. S. Ludford, and J. Buckmaster. Diffusion flames in a chamber. *Acta Astronautica*, 6:943–959, 1979.
- [70] N. Peters. Laminar diffusion flamelet models in non-premixed turbulent combustion. *Prog. Energy Combust. Sci.*, 10:319–339, 1984.
- [71] S. Kukuck and M. Matalon. The onset of oscillations in diffusion flames. *Combust. Theory Modelling*, 5:217–240, 2001.
- [72] J. S. Kim. Linear analysis of diffusional-thermal instability in diffusion flames with lewis numbers close to unity. *Combust. Theory Modelling*, 1:13–40, 1997.
- [73] R. Vance, M. Miklavcic, and I. S. Wichman. On the stability of one-dimensional diffusion flames established between plane, parallel, porous walls. *Combust. Theory Modelling*, 5:147–161, 2001.
- [74] M. Miklavcic, A. B. Moore, and I. S. Wichman. Oscillations and island evolution in radiating diffusion flames. *Combust. Theory Modelling*, 9(3):403–416, 2005.
- [75] H.Y. Wang, J.K. Bechtold, and C.K. Law. Nonlinear oscillations in diffusion flames. *Combustion and Flame*, 145(1-2):376–389, 2006.
- [76] M. R. Dongworth and A. Melvin. The transition to instability in a steady hydrogen-oxygen diffusion flame. *Combust. Sci. Technol.*, 14:177–182, 1976.
- [77] S. Ishizuka and H. Tsuji. An experimental study of effect of inert gas on extinction of laminar diffusion flames. *Symposium (International) on Combustion*, 18:695–703, 1981.
- [78] R.-H. Chen, G. B. Mitchell, and P. D. Ronney. Diffusion-thermal instability and flame extinction in nonpremixed combustion. *Symposium (International) on Combustion*, 24:213–221, 1992.
- [79] Marc Furi, Paul Papas, and Peter A. Monkewitz. Non-premixed jet flame pulsation near extinction. *Proc. of the Combustion Inst.*, 28:831–838, 2000.
- [80] D. Lo Jacono, P. Papas, and P. A. Monkewitz. Cell formation in non-premixed, axisymmetric jet flames near extinction. *Combust. Theory Modelling*, 7:635–644, 2003.

- [81] D. Lo Jacono and P.A. Monkewitz. Scaling of cell size in cellular instabilities of nonpremixed jet flames. *Combustion and Flame*, 151:321–332, 2007.
- [82] P. Metzener and M. Matalon. The effect of thermal expansion on the stability of a planar diffusion flame.
- [83] C.H. Sohn, S.H. Chung, and J.S. Kim. Instability-induced extinction of diffusion flames established in the stagnant mixing layer. *Combustion and Flame*, 117(1-2):404–412, 1999.
- [84] E. W. Christiansen, S. D. Tse, and C. K. Law. A computational study of oscillatory extinction of spherical diffusion flames. *Combustion and Flame*, 134(4):327–337, 2003.
- [85] S. R. Lee and J. S. Kim. On the sublimit solution branches of the stripe patterns formed in counterflow diffusion flames by diffusionalthermal instability. *Combust. Theory Modelling*, 6:263–278, 2002.
- [86] A. L. Valär, C. E. Frouzakis, A. G. Tomboulides, and K. Boulouchos. Numerical simulation of cellular instabilities in jet diffusion flames. In *Third European combustion meeting*, 2007.
- [87] J. S. Kim and S. R. Lee. Diffusionalthermal instability in strained diffusion flames with unequal lewis numbers. *Combust. Theory Modelling*, 3:123–146, 1999.
- [88] F. E. Fendell. Ignition and extinction in combustion of initially unmixed reactants. *J. Fluid Mech.*, 21(2):281–303, 1965.
- [89] J. Buckmaster, A. Nachman, and S. Taliaferro. The fast-time instability of diffusion flames. *Physica*, 9(3):408–424, 1983.
- [90] D. G. Goodwin. Cantera: Object-oriented software for reacting flows. Available at <http://www.cantera.org>.
- [91] D. G. Goodwin. An open-source, extensible software suite for cvd process simulation, chemical vapor deposition. volume 2003-08, page 155162. The Electrochemical Society.
- [92] S. Gordon and B.J. McBride. Computer program for calculation of complex chemical equilibrium composition, rocket performance, incident and reflected shocks and chapman-jouguet detonations. Technical Report SP-273, NASA, 1971.
- [93] B.J. McBride, S. Gordon, and M.A. Reno. Coefficients for calculating thermodynamic and transport properties of individual species. Technical Report TM-4513, NASA, 1993.
- [94] Robert M. Fristrom. Flame sampling for mass spectrometry. *International Journal of Mass Spectrometry and Ion Physics*, 16:15–32, 1975.
- [95] G. P. Smith, D. M. Golden, M. Frenklach, N. W. Moriarty, B. Eiteneer, M. Goldenberg, C. T. Bowman, R. K. Hanson, S. Song, W. C. Gardiner, V. V. Lissianski, and Z. Qin. http://www.me.berkeley.edu/gri_mech/.

- [96] E. Robert and P. A. Monkewitz. Thermo-diffusive instabilities in a low-strain planar diffusion flame. In *5th US Combustion Meeting*. San Diego CA, 2007.
- [97] C. Willert and M. Jarius. Planar flow field measurements in atmospheric and pressurized combustion chambers. *Experiments in Fluids*, 33:931–939, 2002.
- [98] B. Mauconduit and M. Trinite. Nouvel anémomètre basse vitesse utilisant une thermistance maintenue a température constante. *J. Physics E*, 9:1091–1096, 1976.
- [99] H. Fujita, T. Ohhashi, M. Asakura, M. Yamada, and K. Watanabe. A thermistor anemometer for low flow-rate measurements. *IEEE Trans. Inst. Meas.*, 44(3):779–782, 1995.
- [100] J.-A. Hertig, J.-C. Keller, and P. Liska. Sonde thermoanemometrique directionnelle. Technical report, EPFL-INER, 1980.
- [101] Thomas Dreier and David J. Rakestraw. Measurement of oh rotational temperatures in a flame using degenerate four-wave mixing. *Optics Letters*, 15(1):72–74, 1990.
- [102] R. Cattolica. Oh rotational temperature from two-line laser-excited fluorescence. *Applied Optics*, 20(7):1156–1166, 1981.
- [103] A. C. Eckbreth. *Laser Diagnostics for Combustion Temperature and Species*. Gordon and Breach, 1996.
- [104] C. S. McEnally, Ümit Ö. KÖYLÜ, Lisa D. Pfefferle, and Daniel E. Rosner. Soot volume fraction and temperature measurements in laminar nonpremixed flames using thermocouples. *Combustion and Flame*, 109:701–720, 1997.
- [105] Daniel D. Pollock. *Thermocouples: Theory and Properties*. CRC, 1991.
- [106] Thomas W. Kerlin. *Practical Thermocouple Thermometry*. Instrumental Society of America, 1999.
- [107] Robert M. Fristrom. *Flame Structure and Processes*. Oxford University Press, 1995.
- [108] J. D. Bittner. *A molecular beam mass spectrometer study of fuel-rich and sooting benzene-oxygen flames*. PhD thesis, Massachusetts Institute of Technology. Dept. of Chemical Engineering, 1981.
- [109] J. H. Miller, S. Elreedy, B. Ahvazi, F. Woldu, and P. Hassanzadeh. Tunable diode-laser measurement of carbon monoxide concentration and temperature in a laminar methane-air diffusion flame. *Applied Optics*, 32(30):6082–6089, 1993.
- [110] W. E. Kaskan. The dependence of flame temperature on mass burning velocity. *Symposium (International) on Combustion*, 6(1):134–143, 1957.
- [111] E. A. Theby J. M. Madson. SiO₂ coated thermocouples. *Combust. Sci. Technol.*, 36:205–209, 1984.
- [112] K. A. Burton, H. D. Ladouceur, and J. W. Fleming. An improved noncatalytic coating for thermocouples. *Combust. Sci. Technol.*, 81:141/145, 1992.

- [113] J. H. Kent. A noncatalytic coating for platinum-rhodium thermocouples. *Combustion and Flame*, 14:278–282, 1970.
- [114] R. A. Shandross, J. P. Longwell, and J. B. Howard. Noncatalytic thermocouple coating for low-pressure flames. *Combustion and Flame*, 85:282–284, 1991.
- [115] M. E. Kolanz. Introduction to beryllium: uses, regulatory history, and disease. *Applied Occupational and Environmental Hygiene*, 16(5):559–567, 2001.
- [116] J. S. Kim and M. A. Cappelli. Temperature measurements in low-pressure, diamond-forming, premixed flames. *J. Applied Physics*, 84(8):4595–4602, 1998.
- [117] J.P. Holman. *Heat transfer, 9th edition*. McGraw-Hill Book Co., 2002.
- [118] W.H. McAdams. *Heat transmission, 3rd edition*. McGraw-Hill Book Co., 1954.
- [119] D. Bradley and A. C. Entwistle. Determination of the emissivity, for total radiation, of small diameter platinum-10%, rhodium wires in the temperature range 600–1450°C. *British j. of Applied Physics*, 12:708–711, 1961.
- [120] R. E. Stephens. The spectral emissivity and the relation of true temperatures and brightness temperatures of platinum. *J. Opt. Soc. America*, 29:158–161, 1938.
- [121] C. M. Cade. The thermal emissivity of some materials used in thermionic valve manufacture. *IEEE trans. on electron devices*, 8(1):56–69, 1961.
- [122] N. Iwamoto, N. Umesaki, S. Endo, and T. Morimura. Characterization of plasma-sprayed and whisker-reinforced alumina coatings. *J. Mat. Sciences*, 22:1113–1119, 1987.
- [123] M.E. Jr. Whitson. Handbook of the infrared optical properties of Al_2O_3 , carbon, mgo, and ZrO_2 . volume i. Technical report, Aerospace Corp., El Segundo, CA (USA). Chemistry and Physics Lab., 1975.
- [124] J. Peeters and G. Mahnen. Reaction mechanisms and rate constants of elementary steps in methane-oxygen flames. *Symposium (International) on Combustion*, 14(1):133–146, 1973.
- [125] R. V. Serauskas, G. R. Brown, and R. Pertel. A supersonic molecular beam atmospheric pressure flame sampling system. *Int. J. Mass Spectr. and Ion Phys.*, 17:69–87, 1975.
- [126] J. Vandooren, M. C. Branch, and VanTiggelen P. J. Comparisons of the structure of stoichiometric $\text{CH}_4\text{-N}_2\text{O-AR}$ and $\text{CH}_4\text{-O}_2\text{-AR}$ flames by molecular beam sampling and mass spectrometric analysis. *Combustion and Flame*, 90:247–258, 1992.
- [127] A. Bhargava and P. R. Westmoreland. Mbms analysis of a fuel-lean ethylene flame. *Combustion and Flame*, 115:456–467, 1998.
- [128] Joan C. Biordi, Charles P. Lazzara, and John F. Papp. Molecular beam mass spectrometry applied to determining the kinetics of reactions in flames. i. empirical characterization of flame perturbation by molecular beam sampling probes. *Combustion and Flame*, 23:73–82, 1974.

- [129] D. Stepowski, D. Puecherty, and M. J. Cottreau. Use of laser induced fluorescence of oh to study the perturbation of a flame by a probe. *Symposium (International) on Combustion*, 18(1):1567–1573, 1981.
- [130] R. J. Cattolica, S. Yoon, and E. L. Knuth. Oh concentration in an atmospheric-pressure methane-air flame from molecular-beam mass spectrometry and laser-absorption spectroscopy. *Combust. Sci. Technol.*, 28:225, 1982.
- [131] P. Ladd, A. Antipenkov, G. Janeschitz, and R. Marrs. Iter vacuum pumping and leak detection systems. *Fusion Eng. and Design*, 58-59:377–381, 2001.
- [132] M. E. Buckley. Process control in the semiconductor manufacturing environment using a high pressure quadrupole mass spectrometer. *Vacuum*, 44(5-7):665–668, 1993.
- [133] R. K. Waits. Semiconductor and thin film applications of a quadrupole mass spectrometer. *J. Vac. Sci. Technol. A*, 17(4):1469–1478, 1999.
- [134] Charles R. Tilford. Process monitoring with residual gas analyzers : limiting factors. *Surface and Coatings Technology*, 69/69:708–712, 1994.
- [135] Krithi Shetty, S. Zhao, W. Cao, U. Siriwardane and N. V. Seetala, and D. Kuila. Synthesis and characterization of non-noble nanocatalysts for hydrogen production in microreactors. *J. Power Sources*, 163(2):630–636, 2007.
- [136] James E. Blessing, Robert E. Ellefson, Bruce A. Raby, Gerardo A. Brucker, and Robert K. Waits. Recommended practice for process sampling for partial pressure analysis. *J. Vac. Sci. Technol. A*, 25(1):167–186, 2007.
- [137] L. R. Koller. Electron emission from oxide coated filaments. *Physical Review*, 25(5):671–676, 1925.
- [138] E H Hirsch. Thermionic emission change through ambient gas diffusion. *Journal of Physics D: Applied Physics*, 38:2353–2359, 2005.
- [139] Fu Ming Mao and J. H. Leek. The quadrupole mass spectrometer in practical operation. *Vacuum*, 37(8/9):669–675, 1987.
- [140] M. C. Cowen, W. Allison, and J. H. Batey. Nonlinearities in sensitivity of quadrupole partial pressure analyzers operating at higher gas pressures. *J. Vac. Sci. Technol. A*, 12(1):228–234, 1994.
- [141] P. Turner, S. Taylor, E. Clarke, C. Harwood, K. Cooke, and H. Frampton. Calibration effects during natural gas analysis using a quadrupole mass spectrometer. *Trends in Analytical Chemistry*, 23(4):281–287, 2004.
- [142] L. Lieszkovsky, A. R. Filippelli, and C. R. Tilford. Metrological characteristics of a group of quadrupole partial pressure analyzers. *J. Vac. Sci. Technol. A*, 8(5):3838–3854, 1990.
- [143] W. E. Austin and J. H. Leek. Optimization of the operation of the small quadrupole mass spectrometer to give minimum long-term instability. *Vacuum*, 41(7-9):2001–2003, 1990.

- [144] P. O. Schissel and O. C. Trulson. Mass-spectrometric study of the oxidation of tungsten. *Journal of Chemical Physics*, 43(2):737–743, 1965.
- [145] G. D. Earle, R. Medikonduri, N. Rajagopal, V. Narayanan, and P. A. Roddy. Tungsten-rhenium filament lifetime variability in low pressure oxygen environments. *IEEE Transactions on Plasma Science*, 33(5):1736, 2005.
- [146] M. D. Coleman, P. J. Brewer, I. M. Smith, P. M. Harris, M. G. Clift, and M. J. T. Milton. Calibration transfer strategy to compensate for instrumental drift in portable quadrupole mass spectrometers. *Analytica Chimica Acta*, 601:189–195, 2007.
- [147] José Luis Pérez Pavón, Miguel del Nogal Sánchez, Carmelo García Pinto, M. Esther Fernández Laespada, Bernardo Moreno Cordero, and Armando Guerrero Peña. Strategies for qualitative and quantitative analyses with mass spectrometry-based electronic noses. *Trends in Analytical Chemistry*, 25(3):257–266, 2006.
- [148] John-Erik Haugen, Oliver Tomic, and Knut Kvaal. A calibration method for handling the temporal drift of solid state gas-sensors. *Analytica Chimica Acta*, 407:2339, 2000.
- [149] A. G. Gaydon. The emission spectra of flames. *Q. Rev. Chem. Soc.*, 4:1–19, 1950.
- [150] W.G. Bessler, C. Schulz, T. Lee, J.B. Jeffries, and R.K. Hanson. Carbon dioxide uv laser-induced fluorescence in high-pressure flames. *Chem. Phys. Letters*, 375:344–349, 2003.
- [151] S. Chandrasekhar. *Hydrodynamic and hydromagnetic stability*. Oxford University press, 1961.
- [152] E. Bodenschatz, W. Pesch, and G. Ahlers. Recent developments in rayleigh-bénard convection. *Ann. Rev. Fluid Mech.*, 32:709–778, 2000.
- [153] E. Grandjean. *Investigation into localized instabilities in mixed Rayleigh-Bénard-Poiseuille convection*. PhD thesis, EPFL, 2008.
- [154] A. A. Hill, S. Rionero, and B. Straughan. Global stability for penetrative convection with throughflow in a porous material. *IMA J. App. Math.*, 72(5):635–643, 2007.
- [155] N. A. Nield. Throughflow effects in the rayleigh-bénard convective instability problem. *J. Fluid Mech.*, 185:353–360, 1987.
- [156] R. Krishnamurti. On cellular cloud pattern. part 1 : Mathematical model. *J. Atmospheric Sc.*, 32:1353–1363, 1975.
- [157] R. Krishnamurti. On cellular cloud pattern. part 2 : Laboratory model. *J. Atmospheric Sc.*, 32:1364–1372, 1975.
- [158] R. Krishnamurti. On cellular cloud pattern. part 3 : Applicability of the mathematical and laboratory models. *J. Atmospheric Sc.*, 32:1373–1383, 1975.
- [159] F. A. Williams. *Combustion Theory 2nd Edn*. Benjamin Cummings, 1985.

- [160] B. Karlovitz, D. W. Denniston, D. H. Knapschaeffer, and F. E. Wells. Studies on turbulent flames. *Symposium (International) on Combustion*, 4:613–620, 1953.
- [161] M. Matalon. On flame stretch. *Combust. Sci. Technol.*, 31:169–181, 1983.
- [162] M. Matalon, C. Cui, and J. K. Bechtold. Hydrodynamic theory of premixed flames: effects of stoichiometry, variable transport coefficients and arbitrary reaction orders. *J. Fluid Mech.*, 487:179–210, 2003.
- [163] J. O. Hirschfelder, C. F. Curtiss, and R. B. Bird. *Molecular Theory of Gases and Liquids*. John Wiley and Sons, 1966.
- [164] I. K. Puri and K. Seshadri. Extinction of diffusion flames burning diluted methane and diluted propane in diluted air. *Combustion and Flame*, 65:137–150, 1986.
- [165] A. D. Benedetto, F. S. Marra, and G. Russo. Spontaneous oscillations in lean premixed combustion. *Combust. Sci. Technol.*, 174(10):1–18, 2002.
- [166] J. T. Stuart. Nonlinear stability theory. *Ann. Rev. Fluid Mech.*, 3:347–370, 1971.
- [167] S. Cheatham and M. Matalon. Heat loss and lewis number effects on the onset of oscillations in diffusion flames. *Proc. of the Combustion Inst.*, 26:1063–1070, 1996.
- [168] J. Du, R. L. Axelbaum, and C. K. Law. Soot formation in strained diffusion flames with gaseous additives. *Combustion and Flame*, 102:11–20, 1995.
- [169] Wilson Merchan-Merchan, Alexei Saveliev, Lawrence A. Kennedy, and Alexander Fridman. Formation of carbon nanotubes in counter-flow, oxy-methane diffusion flames without catalysts. *Chem. Phys. Letters*, 354:20–24, 2002.
- [170] Saul Dushman. *Scientific Foundations of Vacuum Technique*. John Wiley and Sons, 1962.
- [171] Frank M. White. *Fluid Mechanics*. WCB/McGraw Hill, 1999.
- [172] G. M. Fryer. A theory of gas flow through capillary tubes. *Proc. of the Royal Soc. of London. Series A*, 293(1434):329–341, 1966.
- [173] R. K. Prud’Homme, T. W. Chapman, and J. R. Bowen. Laminar compressible flow in a tube. *App. Sci. Research*, 43:67–74, 1986.
- [174] Y Zohar, S. Y. K. Lee, W. Y. Lee, L. Jiang, and P. Tong. Subsonic gas flow in a straight and uniform microchannel. *J. Fluid Mech.*, 472:125–151, 2002.
- [175] S A Tison. Experimental data and theoretical modeling of gas flows through metal capillary leaks. *Vacuum*, 44(11-12):1171–1175, 1993.
- [176] W. Jitschin, U. Weber, and H. K. Hartmann. Convenient primary gas flow meter. *Vacuum*, 46(8-10):821–824, 1995.

Curriculum Vitae

Etienne ROBERT

Avenue de Senalèche 27
1009 Pully, Switzerland
E-mail: etienne.robort@gmail.com

Born on January 1, 1979
Nationality: Canadian
Languages: French, English, Swedish (basic)

RESEARCH ASSISTANT (2004 - 2008)

Research assistant and PhD candidate at the Swiss Federal Institute of Technology, Lausanne (EPFL):

2004 to 2005 in the Laboratory of Hydraulic Machinery directed by Prof. François Avellan and from 2005 in the Laboratory of Fluid Mechanics directed by Prof. Peter A. Monkewitz.

RESEARCH PROJECTS

▷ **Thesis topic: Experimental investigation of unstrained planar diffusion flames**
Development construction and exploitation of a novel research burner configuration. Use of mass spectrometry and development of custom calibration procedure for in situ species measurement with large dynamic range. LDA employed for velocity measurements in the gas phase.

Supervisor: Prof. Peter A. Monkewitz

Doctoral program in solid and fluid mechanics, project sponsored by the Swiss National Science Foundation (May 2005 to April 2008)

▷ **Investigation of cavitation bubble behavior inside a liquid jet**
Development of a laser-induced cavitation setup. Investigation of bubble behavior close to free surfaces, inside a liquid jet. Experience with high-power lasers, PIV systems, short exposition time photography and ultra-fast cinematography.

A collaboration between the laboratory of hydraulic machines (EPFL) and the European center for nuclear research (CERN). Awarded the Ryhming prize for best research work in fluid mechanics.

TEACHING

▷ **TA for mechanical engineering and physics students**

REVIEWER

Journal of optics and laser technology

EDUCATION

- 2004 Completion of double diploma between École Polytechnique de Montréal and the Swiss Federal Institute of Technology Lausanne:
Bachelor in mechanical engineering (Montréal)
– Specialization in energy
Master of sciences in mechanical engineering (Lausanne)
– Specialization in fluid mechanics
Master's thesis: **Cavitation bubble behavior inside a liquid jet**
- 1999 – 2003 **Master's Program in Mechanical Engineering**, Swiss Federal Institute of Technology, Lausanne, Switzerland
Supervisors: Mohamed Farhat, LMH-EPFL and Jacques Lettry, CERN
- 1998 – 2002 **Bachelor's Program in Mechanical Engineering**, École Polytechnique de Montréal, Québec, Canada

INTERNSHIPS

- ▷ **Research Internship at the Laboratory of Hydraulic Machines (2002)**
Study of cavitation bubble interaction with a free surface. Generation of vapor cavities using a spark gap.
- ▷ **Internship at Alstom Power Canada (2001)**
Engineering internship in a industrial environment. Troubleshooting of a novel sheet metal coating line. Operator formation and technical documentation redaction.
- ▷ **Non-academic Temporary Positions**
Bike Messenger (2002-2003), Vélocité, Lausanne, Switzerland
Tree planter in northern Canada (1999), Netchako Reforestation, Prince-Georges, British-Columbia, Canada
Various tasks on the family orchard (1990-2002), Guided visits, detail and bulk sales, field work, cider and product development

COMPUTER SKILLS

Languages	C++, VB, VBA, Matlab, HTML, \LaTeX
Software	MS Office, Catia, Ideas, Labview, Adobe Illustrator
Operating systems	Windows, Linux, Unix

LIST OF PUBLICATIONS

▷ **Papers in International Journals**

E. Robert and P.A. Monkewitz (2008). Experiments in a novel quasi-1D diffusion flame with variable bulk flow, accepted for publication in Proceedings of the Combustion Institute, Vol. 32, 2009.

E. Robert, J. Lettry, M. Farhat, P. A. Monkewitz, and F. Avellan, (2007). Cavitation bubble behavior inside a liquid jet, Physics of Fluids 19:067106

J. Lettry, A. Fabich, S. Gilardoni, M. Benedikt, M. Farhat, and E. Robert (2003). Thermal shocks and magnetohydrodynamics in high power mercury jet targets, *J. Phys. G* 29:1621.

▷ **Conference Proceedings**

E. Robert and P.A. Monkewitz (2007). Thermo-diffusive instabilities in a low-strain planar diffusion flame, Proceedings of the 5th US Combustion Meeting, San Diego, California, USA.

E. Robert and P.A. Monkewitz (2008). Experiments in a novel quasi-1D diffusion flame with variable bulk flow, in 32nd International Symposium on Combustion Montréal, Québec, Canada.